The Dissertation Committee for Catherine Carter Kitts Certifies that this is the approved version of the following dissertation:

Spectroscopic and Calorimetric Studies of Aggregated Macromolecules

Committee:

David A. Vanden Bout, Supervisor

Paul F. Barbara

Peter J. Rossky

David W. Hoffman

Brian A. Korgel

Spectroscopic and Calorimetric Studies of Aggregated Macromolecules

by

Catherine Carter Kitts, B. S.

Dissertation

Presented to the Faculty of the Graduate School of

The University of Texas at Austin

in Partial Fulfillment

of the Requirements

for the Degree of

Doctor of Philosophy

The University of Texas at Austin

August 2007

Dedication

To my parents: R. Dale Kitts and Theresa A. Kitts.

Whose unconditional love and support has always guided me throughout my life.

Acknowledgements

I first would like to acknowledge my research advisor, Dr. David A Vanden Bout, for all his support and guidance over the course of my graduate career. To my parents, Dale and Theresa Kitts, I would like to thank them for all their support, emotionally and financially, without whom I would not be where I am today. I would also like to thank all the members of the Vanden Bout group, especially Dr. Lynn Rozanski, who's years of friendship helped keep me sane during those frustrating times in graduate school. I would also like to thank all my friends in graduate school, who understood all the pressures we were under and empathize with my struggles. Specifically, I would like to acknowledge Dr. Ron Houk and Natalie Barkey, two of my best friends at UT, who were also encouraging and there for me when I needed a friend. I would also like to acknowledge the UT Taekwon Do Club (ITF) and Mr. Travis Young for their friendship and guidance in marital arts, without which I would never have had a constructive outlet to vent my frustrations during life's trials. I offer many thanks to my girlfriends from high school back in Midlothian, VA for supporting me in my dreams even though those dreams took me to Texas. Finally, I would like to acknowledge my furry friends, Loki the cat, and the late Viggo the hedgehog, who always gave me something happy to come home to.

Spectroscopic and Calorimetric Studies of Aggregated Macromolecules

Publication No._____

Catherine Carter Kitts, Ph.D.

The University of Texas at Austin, 2007

Supervisor: David A. Vanden Bout

Different optical and calorimetric techniques were utilized to gain a better understanding of aggregated macromolecules. This research looked at two different macromolecules: poly(9,9'-dioctylfluorene), a conjugated polymer that forms aggregates in organic solvents; and bovine insulin, which forms amyloid fibrils. Conjugated polymers are of increasing interest due to their thermal stability and ease of solution processing for use in devices. A member of the polyfluorene family, poly(9,9'-dioctylfluorene) (PFO), has been studied due to its blue-emitting spectral properties. However, PFO has been found to form aggregates in solution, which is detected by the presence of a red-shifted absorption peak. This peak is caused when a section of the backbone planarizes forming the β-phase. The β-phase can be removed from the solution upon heating and will not return until the solution is cooled, making it a non-equilibrium process. The dissolution and reformation of the β-phase were monitored using absorption spectroscopy and differential scanning calorimetry. Atomic force microscopy (AFM) and near-field scanning optical microscopy (NSOM) were able to probe the aggregates in

films. It is important to understand polymer properties in solution in order to understand film morphology.

Amyloid fibrils contribute to over 20 different neurodegenerative diseases, in which cures have yet to be found. The fibrils form when a soluble protein misfolds and self-assembles to form insoluble protein aggregates, and the cause of the fibril formation *in vivo* has still yet to be determined. Spectroscopy studies have been made possible with the use of fluorescent dyes: thioflavin T (ThT), BTA-2, and Congo red (CR). These dyes bind to amyloid fibrils and exhibit changes in their spectral properties. However, the exact mechanism for the binding of these dyes has only recently been studied. Through the use of calorimetry, the forces involved with binding of ThT and CR to amyloid fibrils can be determined. Absorption and fluorescence spectroscopy techniques were employed to study the spectral properties of these dyes. Polarized NSOM was used to determine the ThT or BTA-2's orientation with an individual fibril. Understanding how these dyes bind to fibrils will enable researchers to use spectroscopy to study the early stages of fibril formation.

Table of Contents

List of Tables

List of Figures

xiv

xv

xvi

CONJUGATED POLYMERS

Chapter 1: The effect of solvent quality on the chain morphology in solutions of poly(9,9'-dioctylfluorene)

INTRODUCTION

Conjugated polymers have become an area of increasing interest because of their optical and electrical properties,[1-8] making them promising materials for inexpensive, flexible light emitting devices,[2, 9-13] transistors,[14] and photovoltaics.[15, 16] One of the advantages offered by polymer electronics is the ease of solution processing. While this offers potential for rapid production, spin casting yields films whose morphology is not governed by equilibrium. Different morphologies lead to films with different properties.[9, 17-23] Morphology can vary for films cast at different speeds or from different solvents. Moreover, the treatment of the solution prior to casting can affect the properties of the films, such that the chain conformation of the polymer in solution can be partially retained when cast into a film. Studies of light emitting devices of MEH-PPV cast from differing solutions have shown how solvent quality can affect polymer conformation and subsequent properties of both films and devices.[9, 18] Given these issues it is important to understand polymer conformations in both dilute and concentrated solutions to better control subsequent properties of films.

Polyfluorenes present an excellent model system for such studies as the polymer has two conformations with distinct absorption spectra. Polyfluorenes have shown promise because of their high quantum yield and thermal stability;[24-26] specifically, poly(9,9-dioctyl fluorene) (PFO) which has been studied for its blue-emitting spectral properties. PFO's thin film morphology has been shown to affect both the

1

photoluminescence and electroluminescence of PFO films[8, 17, 27, 28] because changes in the structure of the polymer backbone will lead to changes in the conjugation of the electron system.[29] In both films and solutions, PFO has exhibited two distinct conformations denoted simply as the - and -phases. The -phase has been characterized as amorphous and is the only phase present in dilute polymer solutions and in a good solvent.[30-32] The -phase is thought to have a more planar structure with extended conjugation that results in a distinct red-shifted absorption band at 437 nm.[28, 29, 31, 33] It is this unique absorption that makes the PFO system an excellent candidate for studying how solvent processing affects the polymer conformation, as it can be easily monitored by absorption spectroscopy. There have been numerous studies of PFO β-phase formation in thin films. It was first noted that the 437 nm absorption could be increased in thin films by low temperature processing.[34] The increase in β-phase was observed to remain even when the films were reheated to room temperature. Subsequent studies demonstrated that the β-phase could be removed by heating to much higher temperature, although these changes were always gradual rather than exhibiting a distinct transition temperature.[32-34] β-phase formation could also be induced by solvent swelling of films, leading to the conclusion that stressing the film either by low temperature cycling or swelling with incompatible solvents would lead to an increase in β-phase.[33]
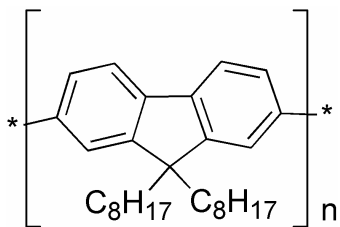
PFO

Beta-phase formation has been associated with aggregation in concentrated solutions. Previously, researchers have speculated that in poor solvents, the polymer chains tend to aggregate to avoid contact with the solvent and form small "crystals" that were dominated by the -phase conformation.[34, 35] In films and in concentrated solutions, intermolecular forces, either between polymer chains or the polymer and a matrix, have been postulated to be the driving force for the -phase formation. A recent study by Monkman *et al.* examined β-phase formation in dilute solutions.[30] In dilute solutions, aggregation and intermolecular forces could be minimized. Monkman *et al.* concluded that the formation of the -phase at low temperatures was the result of the polymer adopting a more stable but lower entropy conformation. They showed that -phase formation was a reversible equilibrium process in dilute solutions, and that aggregation proceeded after the formation of the -phase. In other words, the aggregation was the result of -phase formation rather than aggregation being the cause of -phase formation.[30]

In this paper we will examine how solvent quality affects dissolution of polymer aggregates and the hysteresis of the -phase formation in both dilute and concentrated solutions. The -phase is present when PFO is initially dissolved into many organic solvents and will not dissipate over time even with vigorous stirring. The -phase can be converted completely to the -phase by heating the solution above room temperature. The polymer will remain in the -conformation even after the solution has returned to room temperature. The -phase can be subsequently converted back to the -phase by cooling the solution well below room temperature, and will remain until heated again. Concentrated solutions behave similar to dilute solutions upon heating; however, when cooled below room temperature, gelation occurs. The gelation is concurrent with the appearance of the -phase. This now suggests that the -phase regions of the polymer serve as cross-linking points in the network causing a gel to form. The aggregate

dissolution and the gel formation thermodynamics are explored using UV-Vis spectroscopy and differential scanning calorimetry (DSC) in a variety of different solvents. Other spectroscopic and scanning probe techniques were utilized to characterize the -phase. The transition temperatures for the dissolution and reformation of the -phase vary with solvent quality. Furthermore, the trend with solvent quality implies a collapse of the polymer chain leads to the formation of the -phase and subsequent gelation or aggregation, and that a conformational change in the polymer chain is responsible for the conformational change of the polymer backbone.

EXPERIMENTAL

Poly(9,9'-dioctylfluorene) Sample Preparation

The polymer, poly(9,9'-dioctylfluorene) (PFO), was used as purchased from American Dye Source, Inc (M_n •34,800 with a polydispersity of 2.9). All polymer solutions were made by diluting a 1 wt% PFO stock solution in toluene, tetrahydrofuran (THF), chloroform ($CHCl_3$), or cyclohexane. Heated solutions were prepared in a similar fashion by diluting a portion of the stock solution and applying mild heat until the solution changed from yellow to clear. Cooling was accomplished by either placing the solution in a temperature controlled refrigerator or by immersing the solution in a solvent ice bath (e.g. an acetone/dry ice bath, -78°C). PFO films were made by spin casting an aliquot of the 1 wt% solution onto a glass coverslip at 3000 rpm for 30 s. Coverslips were cleaned by sonicating in KOH for 15 min, then sonicating in DI water for 15 min and finally dried in an oven.

Absorption spectroscopy

Absorption spectra were obtained using a Beckman DU 7400 UV-Visible Diode-array spectrophotometer. Absorption spectra of the 1 wt% PFO stock solution were

collected using a Hellma quartz cuvette with a path length of 10 μm; while absorption spectra of diluted polymer solutions were taken using standard quartz cuvettes with a path length of 1 cm. Diluted solutions were prepared to yield an optical density (OD) between 0.4 and 1 at 390 nm. Kinetics experiments were performed using the same UV-Vis spectrophotometer as for steady state absorption spectra. The kinetics of dissolution were monitored by measuring the absorbance at a fixed wavelength, 437 nm, every 0.1 s for 90 s. The spectrometer contained a cuvette holder with a heating mantle. A blank of toluene was placed in a cuvette (3 mL volume) and allowed to equilibrate to the desired temperature. Once the solvent had reached thermal equilibrium, the kinetics trace was started to ensure no data was loss due to slow reaction time, and then a 25 μL aliquot of the 1 wt% PFO stock solution was added. The large volume of the solvent compared to the added stock solution, ensured a rapid temperature equilibration. An external digital thermometer was utilized to ensure the calibration of the temperatures as well as monitor the temperature stability.

Fluorescence Spectroscopy

Fluorescence and anisotropy measurements were acquired using a Photon Technologies International Quanta Master Model C Cuvette based scanning fluorometer. Samples were excited at 400 nm (polymer peak) and 440 nm (aggregate peak). Bandpass filters of appropriate wavelength were used to ensure a monochromatic excitation beam. Long pass filters were used in the emission path to help eliminate scattered excitation light. For anisotropy measurements two polarizers mounted onto rotation stage were placed in the excitation and emission paths. Emission spectra were then obtained using the following polarizations: HH, HV, VH, VV (H=horizontal polarization, V=vertical polarization), where the first letter denotes the polarization of the excitation and the second letter is the polarization of the emission. The G-factor of the instrument was

determined by dividing the intensity of the HV polarizations by the intensity of the HH polarizations for each wavelength. The anisotropy was calculated using the following equation:

$$r = \frac{I_{VV} - (G * I_{VH})}{I_{VV} + (2 * G * I_{VH})}$$

Scanning Probe Microscopy

Atomic Force Microscopy (AFM) images were taken on a Nanoscope II (Digital Instruments/Veeco) multimode scanning probe microscope in tapping mode. Near-Field Optical Microscopy (NSOM) images were collected using an Aurora system (Thermomicroscopes/Veeco). A frequency doubled Ti-Sapphire laser was utilized to excite the sample at either 400 or 440 nm. Near-field probes were manufactured in-house and mounted on piezo-electric tuning forks for shear-force feedback. The fluorescence was collected through a 455 nm longpass filter on an Avalanche Photo-diode (APD).

Differential Scanning Calorimetry

Differential Scanning Calorimeter (DSC) measurements were acquired using a Perkin Elmer DSC 7 and/or a TA Instruments Q100 DSC. Two empty large volume stainless steal pans (max volume 60 μL) were used for baseline subtraction. A 45 μL aliquot of the 1 wt% PFO solution in toluene or THF was used as the sample and for the PFO gel samples, a portion of the gel was placed in the pan. The pans were then hermatically sealed using the Perkin Elmer Quick Press (0990-8467) and spacer insert (0319-1047). Care was taken in massing the pans prior to insertion of the sample and after the pans were sealed in order to determine the mass of the sample, which is inputted into the computer program prior to heating. DSC data were collected from 20 to 90 °C and/or 20 to -90 °C at a rate of 5°C/min for both the baseline and the sample. After

sample runs the pans were re-massed to verify that no solvent was lost through evaporation.

Differential Scanning Calorimetry Technique

Differential scanning calorimetry (DSC) is a common technique used for studying the different phase transitions of polymers. The DSC is a thermal analysis technique that monitors the change in heat flow between a reference and a sample as a function of temperature.[36] In the DSC instrument, there are two independent furnaces, where one heats the sample and the other heats the reference. Samples are typically placed in an aluminum pan with a lid, while the reference pan is an empty aluminum pan. A heating program is inputted into the computer with the interested temperature range and the heating rate. When the heating program is started, the sample and reference pans are kept at the same temperature throughout the experiment. The DSC then measures the change in energy input in either the sample or reference to maintain both at a constant temperature.[37] If there is any difference in the reference power between the sample and reference, it is plotted as a function of sample temperature. In polymers, researchers are interested in determining the glass transition temperature, the melt transition temperature and the crystallization transition temperature.

RESULTS

Steady state absorption spectra were used to quantify the β-phase in the PFO solutions. Figure 1.1 shows the absorption spectrum of a dilute PFO solution in toluene before heating, after heating above 60 °C, and after cooling to -78 °C. All three spectra were taken after the samples had re-equilibrated to room temperature. The spectrum of the unheated solution exhibits two distinct absorption peaks, one at 390 nm and one at 437 nm. The absorption peak at 390 nm is assigned to the standard morphology or α-

phase, while the red shifted peak at 437 nm is assigned to the β-phase. When the solution is heated, the absorption spectrum shows an increase in the 390 nm peak and no peak at 437 nm, indicating an absence of polymer in the β-phase. The heated solutions remain free of any absorbance at 437 nm even after many months at room temperature. When the sample was cooled to -78 °C for 40 min and then allowed to re-equilibrate to room temperature, the β-phase peak was observed; however, in toluene the size of the peak had greatly diminished when compared to the original solution spectrum.
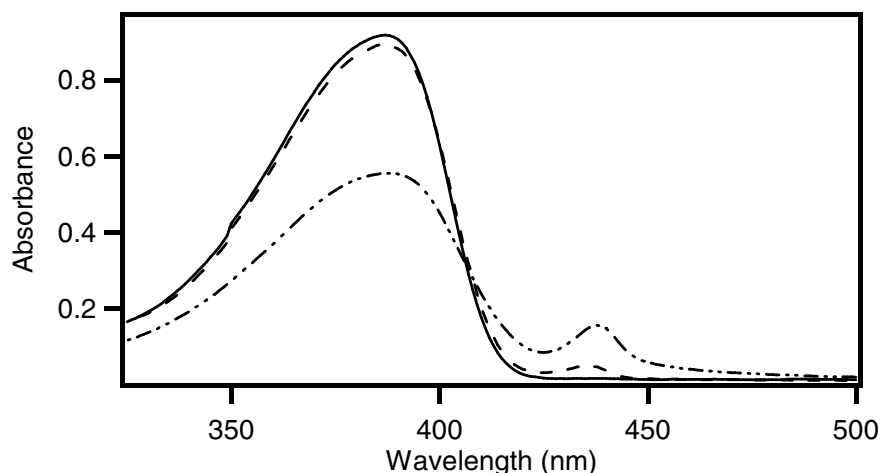
Figure 1.1   Absorption spectra of PFO in toluene. The dotted and dashed line is the absorption spectrum of the aggregated PFO solution, the solid line is the absorption spectrum of the PFO solution after heated, and the dashed line is the absorption spectrum of the PFO solution after it had been cooled for 40 minutes at -78 °C. All absorption spectra were taken using the same PFO solution.

Comparable results were observed in PFO solutions made with different solvents. Heating the solutions above 50 °C resulted in the dissolution of the β-phase which did not return upon subsequent cooling to room temperature. The only notable difference between the solutions in different solvents was that the β-phase returned at different temperatures. The transition temperatures from the UV-Vis are shown in Table 1.1.

8

These are rough estimates of the temperature obtained by systematically increasing the solution temperature and taking an absorption spectrum at each temperature until the β-phase was gone. The temperature at which the β-phase disappeared was the approximate transition temperature.

Solvent	% β-phase present	Heat Transition Temp (°C)	% β-phase reformed	Cool Transition Temp (°C)	Gel (y or n)
CHCl$_3$	11.52	45	N/A	-42	n
Toluene	24.71	53	3.61	-55	y
THF	20.59	50	37.43	-25	y
Cyclohexane	46.18	73	18.21	10	y

Table 1.1   Summary of the transition temperatures of PFO in different solvents. Also the percent β-phase present before heating and after cooling past the transition temperature.

Another characteristic of the PFO solutions is that the initial solution is noticeably cloudy, indicating aggregated polymer present in the solution, but after heating the solution becomes clear and remains so indefinitely. In addition to heating, the solution can be either filtered or centrifuged to remove some of the larger aggregates. After filtration or centrifugation, there is a reduction in the β-phase absorption peak (data not shown). The total amount of β-phase also varies with solvent quality. The interconversion between the α- and β-phases can be more clearly seen in Figure 1.2, where several absorption spectra where taken at 47 °C at different time intervals as the β-phase slowly disappeared. The spectra reveal a clear isosbestic point at 405 nm, which is characteristic of two inter-converting species. The increase in the α-peak was found to be directly proportional to the disappearance of the β-phase peak. For all spectra, the total integrated area of both peaks remained constant.
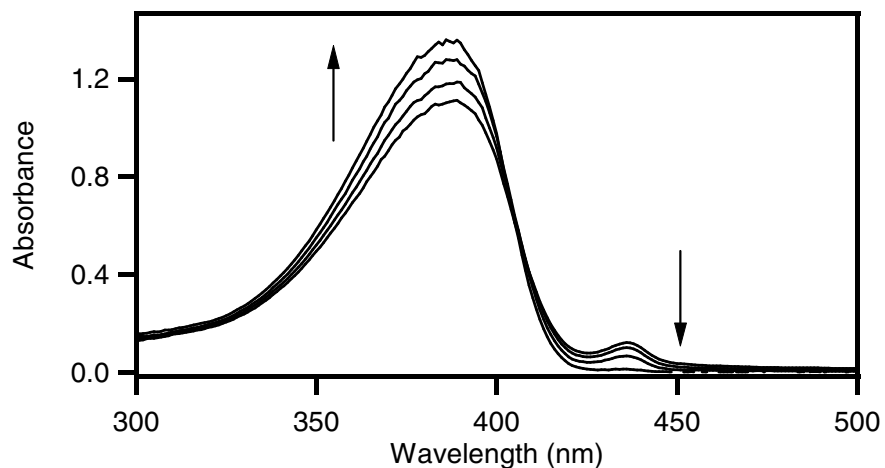
Figure 1.2   Absorption spectra of PFO in toluene at 47 °C at different time intervals showing the decay of the aggregate peak with time.

Concentrated solutions exhibited a slightly different behavior.   The absorption spectrum for a 1 wt% PFO solution in toluene has a similar absorption spectrum as the dilute PFO solution. When the concentrated solution is heated the 437 nm peak converts into a larger absorption at the α peak in the same way the dilute solution does. However, when the 1 wt% PFO solution is cooled to -78 °C the solution completely gels. An absorption spectrum of the PFO gel reveals a reformation of the β-phase as indicated by a return of the 437 nm absorption. When the gel returns to room temperature it remains in the gel state and does not melt into an aggregated solution. It will not return to solution until heated again. Similarly concentrated PFO solutions in other solvents have slightly different heating and cooling transitions (see Table 1.1 for summary) and all formed gels except for CHCl₃.

In the best solvent, the fraction of β-phase was found to be independent of concentration. Figure 1.3 shows the absorption spectrum of two toluene solutions with very different concentrations. The solid line is the absorption of the 1 wt% stock solution in a cuvette with a path length of 10 μm, while the dotted line shows the spectrum of a

10

solution that has been diluted by a factor of 1000 in a 1 cm cuvette. The product of the

concentration and path length for both samples was constant. The ratio of the α to the β

peak (6:1) is identical in both cases despite a three order of magnitude difference in the

total concentration of the solutions. Slight differences in the total absorbance of the two

samples were likely the result of variation in the thickness of the small path length

cuvette and/or slight dilution errors.
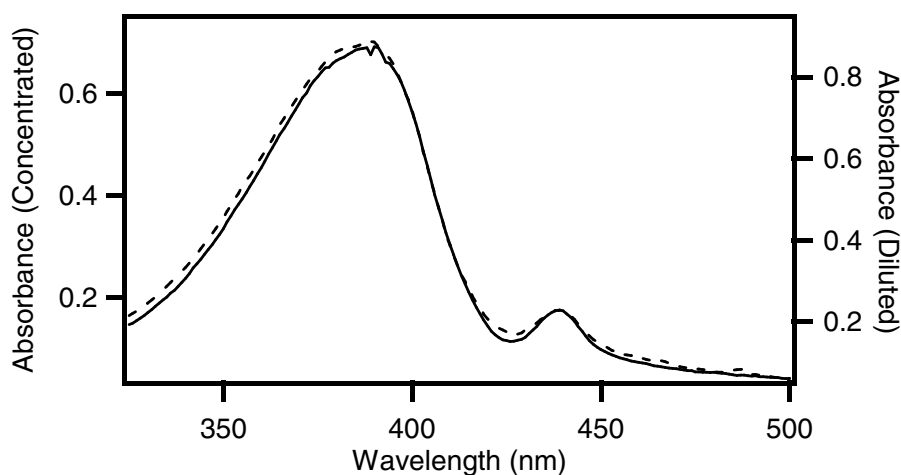
Figure 1.3   Absorption spectra of aggregated PFO solutions; a comparison of a
              concentrated solution versus a diluted solution. The solid line is the
              absorption spectrum of the concentrated PFO solution (1 wt%) collected
              using a 10 μm path length cell. The dashed line represents the diluted PFO
              solution that was collected using a standard 1 cm path length cuvette.

The kinetics of the disappearance of the β-phase can be monitored by measuring

the absorption at 437 nm as function of time after a temperature jump.   Kinetic

measurements showed the peak at 437 nm is apparently infinitely slow at room

temperature with the rate becoming finite as the temperature increases.   Then the rate

increases rapidly when the temperature approaches 50 °C. A typical kinetics transient is

shown in the Figure 1.4. The decay can be well characterized by an exponential fit;

however, the final absorbance at 437 nm is not zero indicating a residual amount of

11

polymer still in the β-form, or that the kinetics are extremely slow for the conversion of the remaining polymer.
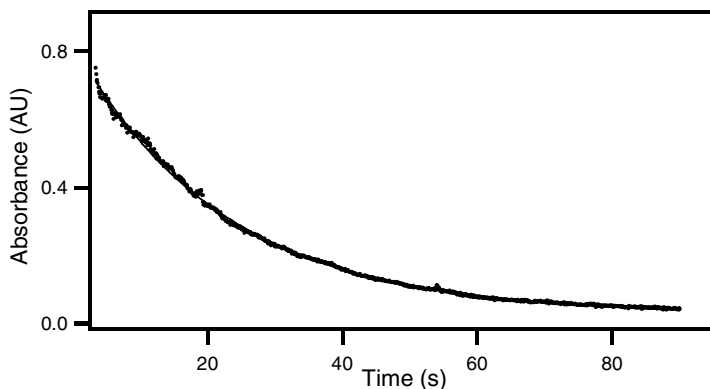
Figure 1.4   An absorption decay of the 437 nm peak at 52 °C. Exponential fit overlaid by the data yielded a rate constant of 0.045 s^{-1} (τ = 22 s).

Similar effects to those observed in absorbance could be seen in the emission spectra of PFO solutions in toluene. When an aggregated PFO solution was excited at 400 nm, the emission spectrum demonstrated three vibrational peaks, with the most predominant peak at 438 nm. After heating the PFO solution, the emission spectrum still had three vibrational peaks, except the first peak had increased dramatically in intensity while the second peak showed little change in intensity. Then upon cooling the solution, there was a decrease in the 438 nm peak and an increase in the second peak, compared to the heated solution's spectrum. This demonstrated that upon cooling some α-phase was converted into the β-phase, which caused then predominate α-phase emission peak (438 nm) to decrease. Figure 1.5a shows the fluorescence spectra for the aggregated, heated, and cool solutions. Since the original aggregated solution was excited near the isosbestic point (405 nm), the emission spectrum was a sum of both - and β-phase species. However, when the aggregated solution was excited near the β-phase peak (440 nm) only

12

the β-phase emission was excited. In order to confirm this, the heated emission spectrum was subtracted from the original aggregated emission spectrum, yielding a spectrum of only the aggregate emission.   The subtracted spectrum was then compared to the aggregate emission spectrum excited at 440 nm and when plotted together, the subtracted spectrum and aggregated spectrum overlaid one another exactly (Figure 1.5b).
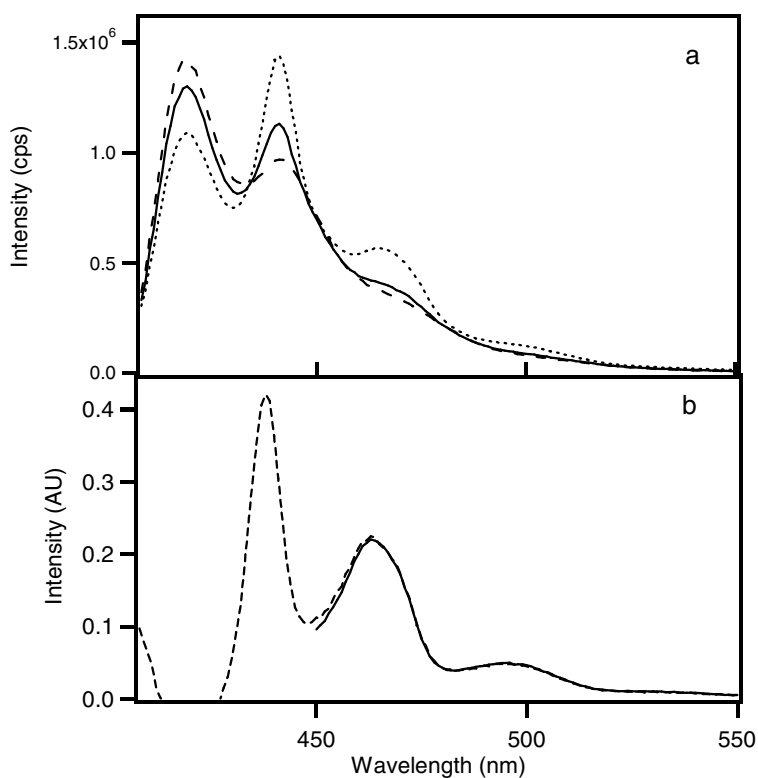
Figure 1.5   a) Fluorescence spectra of PFO solution in toluene excited at 400 nm. The dotted line is the fluorescence spectrum of the aggregated solution, the dashed line is the fluorescence spectrum after the solution had been heated, and the solid line is the fluorescence spectrum of the cooled solution. b) The solid line is the fluorescence spectrum of the aggregated PFO solution excited at 440 nm and the dashed line is the resultant spectrum when the heated spectrum was subtracted from the aggregate spectrum.

Fluorescence anisotropy measurements were taken of the aggregated PFO solution, heated PFO solution and cooled PFO solution in toluene as discussed above. The aggregated and cooled solutions were excited at both 400 nm and 440 nm, and the anisotropy was calculated for both excitations (Figure 1.6). The heated PFO solution, which is all -phase, had a calculated anisotropy of ~0.13 (Figure 1.6C). This anisotropy corresponds with the long solvated polymer chains rotating in solution. The aggregated and cooled spectra that were excited at 400 nm also had similar anisotropies to that of the heated solution. The aggregated solution's anisotropy was ~0.15 and the cooled solution's anisotropy was ~0.14. This is to be expected, even though the aggregated and cooled solutions contain both the β-phase and -phase, they are primarily comprised of the -phase. However, when the aggregated and cooled solutions were excited at 440 nm, the anisotropy of the β-phase was calculated to be ~0.3 (Figure 1.6B & D). An anisotropy of 0.3 reveals that indeed the β-phase consists of large, slow rotating aggregates.
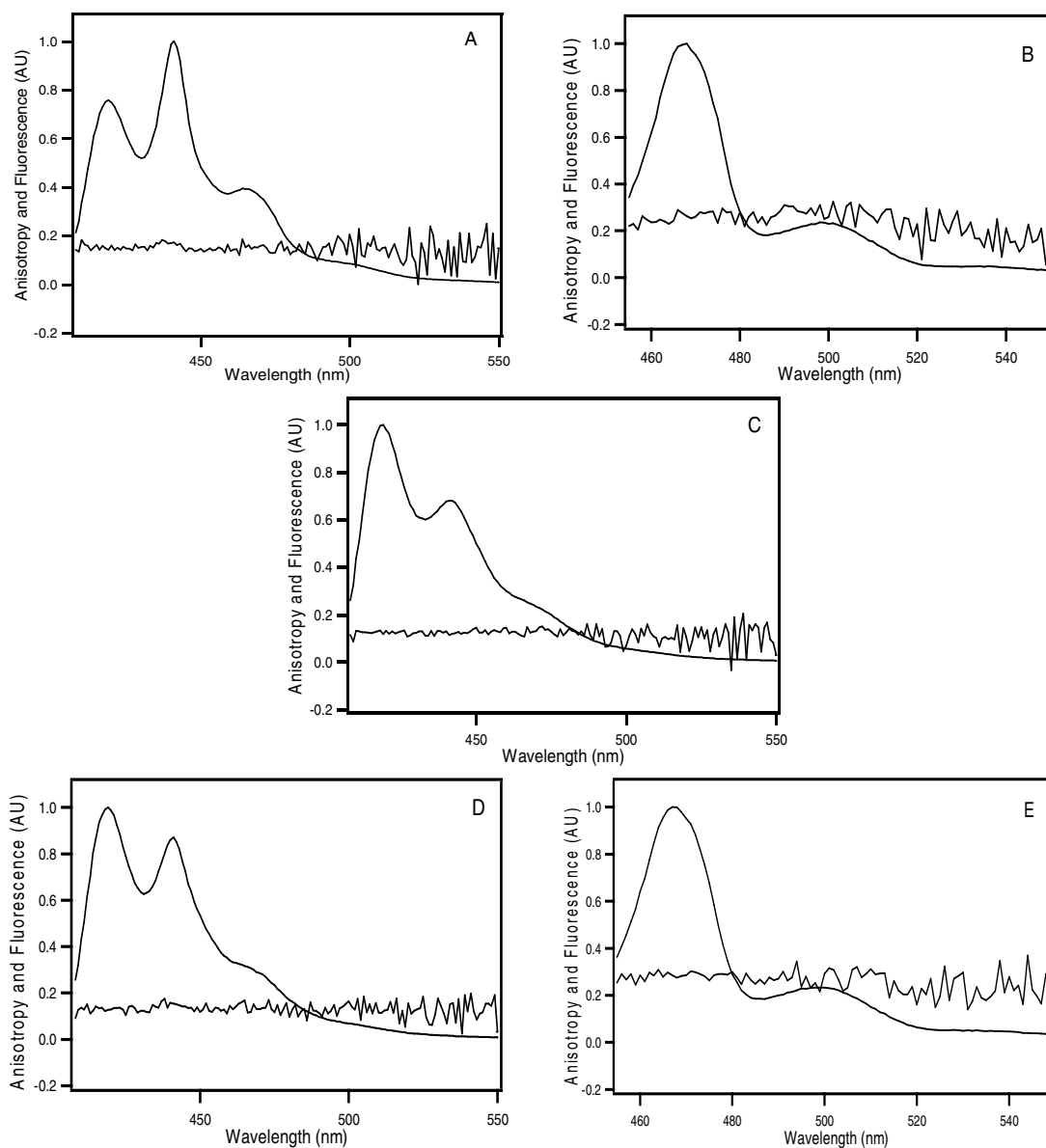
Figure 1.6 A) The fluorescence spectrum of an aggregated PFO solution excited at 400 nm with the anisotropy, B) the same solution in A excited at 440 nm and the anisotropy of the aggregates, C) the fluorescence spectrum of the PFO solution heated with the anisotropy of the α-phase excited at 400 nm, D) the fluorescence spectrum of the PFO solution cooled to -78 ºC and the anisotropy excited at 400 nm, and E) the fluorescence spectrum of the cooled solution excited at 440 nm with the anisotropy

Scanning probe microscopy was utilized to directly probe the polymer aggregates. AFM images were acquired of films cast from PFO aggregated, aggregated and filtered, and heated solutions in toluene, shown in Figure 1.7. The AFM image of the film cast from the aggregated solution clearly showed small polymer clumps, roughly 20 nm in height. The film cast from a filtered aggregated solution showed a reduced number of aggregates present on the film, while the film cast from a heated solution had no visible aggregates present.
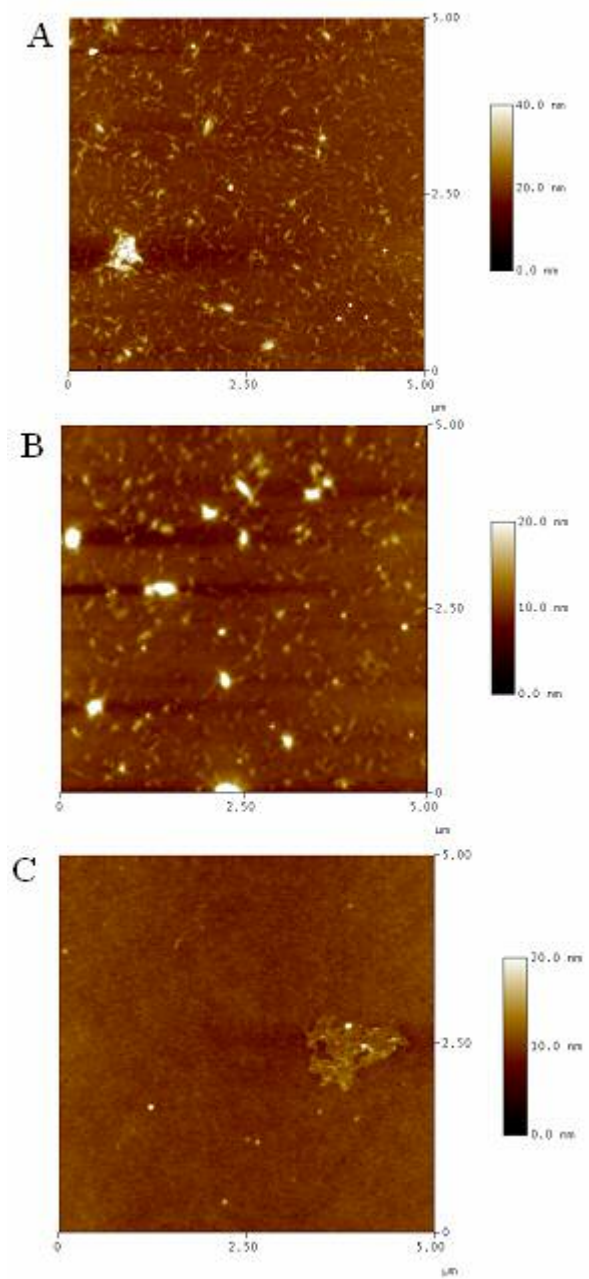
Figure 1.7   All images are 5 X 5 μm AFM images taking in tapping mode. A) PFO film
made from an aggregated solution, B) PFO film made from a filtered
solution, and C) PFO film made from a heated solution.

NSOM[38, 39] was used to probe the aggregates in order to see if they can be directly excited at the 437nm absorption peak. A film cast from a filtered aggregated solution was imaged with an excitation wavelength of 440 nm. The aggregates are clearly present in the topography image as 20 nm clusters (Figure 1.8A). The fluorescence image shows that the aggregates are fluorescent at this excitation wavelength (Figure 1.8B). Moreover, the rest of the film exhibits almost no fluorescence indicating that nearly all the polymer with the β-phase morphology is in the aggregates. Previous studies of conjugated polymer aggregates have shown they can have a lower fluorescence quantum yield due to a variety of interchain electronic interactions.[17, 19] Previous NSOM images of PFO films with small aggregates had a decrease in emission were observed for the aggregates seen in the topography,[40] but these studies did not look at direct excitation of the β-phase. When the β-phase is excited directly it is clear that the polymer aggregates are more fluorescent than the film. Although, this is likely due to the concentration of the β-phase rather than the relative quantum yields of the aggregates versus the film.
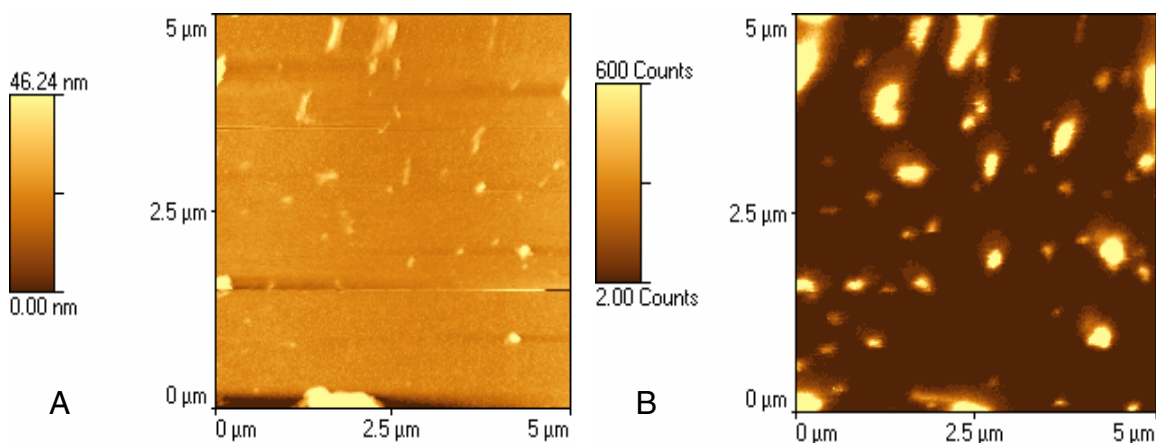
Figure 1.8   Both NSOM images are 5 X 5 μm with 200 resolution. A) Topography
              image of a PFO film filtered and B) the corresponding fluorescence image
              excited at 440 nm.

DSC measurements were taken to probe the thermodynamics of the aggregate dissolution and the gelation phenomena. Figure 1.9A shows the DSC scan of an initially unheated solution from 20 to 90 °C. A clear endothermic peak is observed at ~53 °C, which is the same temperature where the kinetics become too rapid to record. However, upon cooling from 90 °C to 20 °C, no exothermic peak at 53 °C was seen. Then after the initial heating run, the same sample was allowed to equilibrate to 20 °C and rescanned to 90 °C, and no transition peak was observed. As was the case with the absorption spectra, the changes that were observed were not reversible. The enthalpy for the endothermic transition observed in the initial DSC scan was measured to be 0.1353 J g^{-1} of solution. Subsequently, when an aggregated PFO solution in toluene was heated and then cooled down to -90 °C, an exothermic peak was observed at -56 °C (Figure 1.9B). The enthalpy for the transition was calculated to be -0.1518 J g^{-1} of solution (-5.90 kJ/mol of monomer). The sample was then re-heated past the transition temperature and another endothermic peak was observed at approximately the same temperature as before. This suggests that the aggregates are indeed reforming when the sample is cooled off.
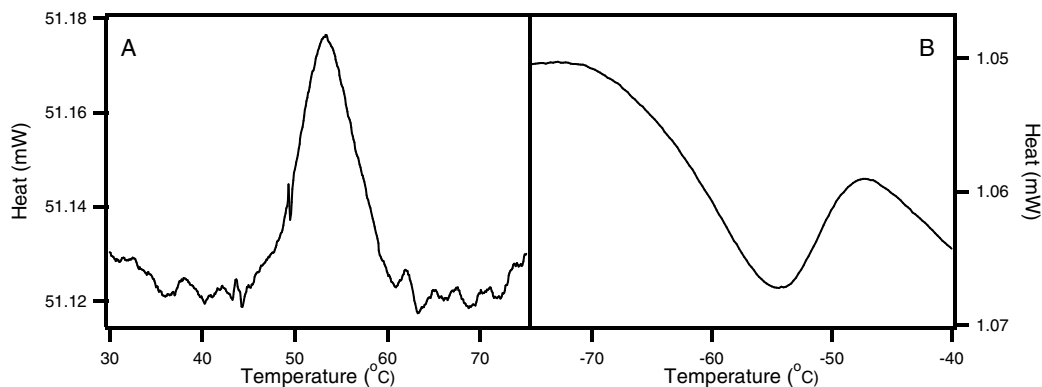
Figure 1.9   The DSC data: A) PFO solution in toluene heated from 20 °C to 90 °C. The transition temperature was measured to be 53.3 °C and •H was calculated to be 24.37 kJ mol^{-1} of monomer. B) The same solution as in a) cooled to -90 °C. The exothermic transition was at -56 °C and the •H was calculated to be -5.90 kJ mol^{-1} of monomer.

DSC measurements were also taken of a PFO solution in THF. The DSC scan of an aggregated 1 wt% PFO solution in THF heated from 20 °C to 60 °C showed a clear endothermic peak at ~48 °C (Figure 1.10A). The enthalpy of the aggregate dissolution was 0.1631 J g^{-1} of solution. As in toluene, when the solution was cooled past the transition temperature, no exothermic peak was observed. However, upon cooling down to -90 °C, an exothermic peak occurred at -25 °C (Figure 1.10B). The enthalpy of the reverse transition was -0.3182 J g^{-1} of solution. The reverse transition enthalpy was calculated using the total polymer in the solution, since the fraction of -phase that reforms is unknown. Upon heating the solution again, an endothermic peak at 47 °C was observed, indicating that in fact the -phase did reform.
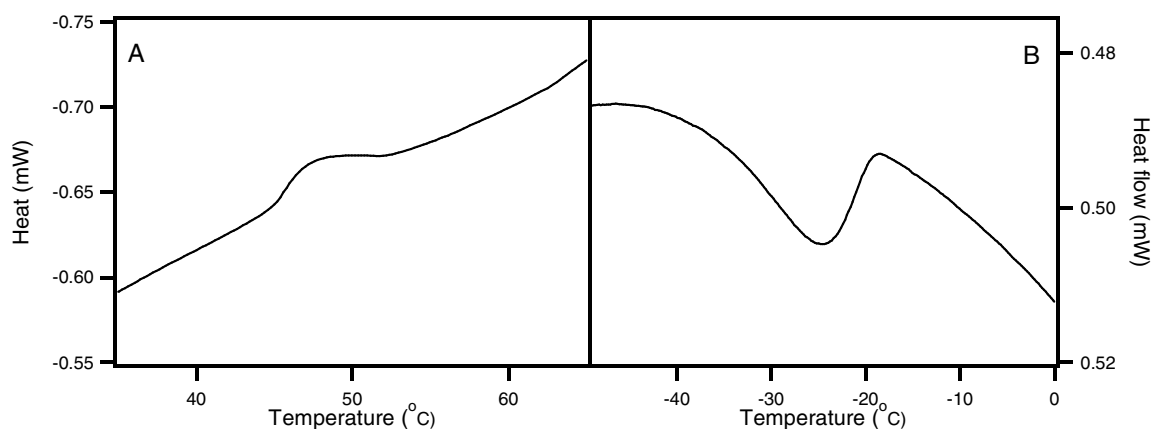
Figure 1.10 The DSC data: A) PFO solution in THF heated from 20 °C to 60 °C. The transition temperature was measured to be 48 °C and •H was calculated to be 31.70 kJ mol^{-1} of monomer. B) The same solution as in A) cooled to -90 °C. The exothermic transition was at -25 °C and the •H was calculated to be -12.37 kJ mol^{-1} of monomer.

The DSC scan of PFO gel in toluene when heated from 20 to 90°C has a large endothermic transition at ~46 °C, with an enthalpy of 0.4299 J g^{-1} of gel. When the sample was cooled to -90 °C, there was an exothermic transition at ~-54 °C with an enthalpy of -0.1834 J g^{-1} of gel. Upon re-heating the sample to 90 °C, another endothermic peak was observed near the same temperature. However, the enthalpy of the second heat transition does not have the same value, which indicates that the β-phase does reform but he sample does not have the time to fully gel. Nonetheless, this extreme hysteresis in transition temperature is often observed in gel formation.[41-43] Similar results were seen in the DSC scan of the PFO gel in THF. All DSC results are summarized in Table 1.2.

21

Solvent	Solution or Gel	Dissolution Transition Temp (°C)	Heating ΔH (kJ mol^{-1} of monomer)	Reformation Transition Temp (°C)	Cooling ΔH (kJ mol^{-1} of monomer)
Toluene	solution	51	21.04	-56	-5.90
THF	solution	48	31.70	-25	-12.37
Toluene	gel	46	167.10	-54	-7.13
THF	gel	51	40.04	-21	-23.80

Table 1.2   Summary of the enthalpies obtained from the DSC results for PFO solutions and gels in either toluene or THF and their transition temperatures.

DISCUSSION

It is clear that in the initial aggregated solution the majority of the PFO in the β-phase is in the remnants of larger aggregates that did not dissolve at room temperature. As previously described in other solvents systems, concentrated solutions of cyclohexane, THF, and toluene exhibit a substantial absorbance peak at 437 nm. This absorbance can be greatly reduced upon filtration indicating the large aggregates contain much of the -phase PFO. This is confirmed through absorption spectra and AFM images. After filtering, a decrease in the -phase absorption peak is observed, while the AFM images show a decrease in the number of aggregates present on the film. The NSOM fluorescence image also confirms that the aggregates have a strong 437 nm absorption. Finally, as seen in toluene, the fluorescence anisotropy of the emission excited at 440 nm shows a large anisotropy value of 0.3 compared to 0.13 when excited at 400 nm, indicating the -phase is associated mostly with large, slowly rotating aggregates. There is no doubt that the -phase is strongly associated with aggregation.

The aggregates that will not dissolve are vestiges of polymer chains with large -phase regions formed during the drying of the polymer powder. They are not in equilibrium with the solvated α-chains in solution. If the aggregates were the result of the association between solvated chains, then the aggregation would display a strong

concentration dependence. In contrast, the number of aggregates as monitored by the -phase absorbance is concentration independent even over three orders of magnitude (Figure 1.3). The aggregates also do not seed the formation of the -phase. Mixing a heated fully solvated -phase solution with a portion of the original aggregated solution did not change the amount of -phase present, even after a couple days. Given this, the polymer aggregates are clearly not simple -stacked chains like molecular dye aggregates. While polymer and molecular aggregates both demonstrate a red-shifted absorption spectrum, the physical nature of these two species are found to be dramatically different. Molecular aggregation is an equilibrium process in which the formation and dissolution of the aggregates is a strong function of monomer concentration.[44] In this case the PFO aggregates remain in a similar ratio of - to -phase over a wide range of concentrations. The results indicate that the -phase fraction in the polymer at room temperature is in a meta-stable state stabilized by the aggregates and suspended in the solution regardless of concentration or solvent quality.[10, 45]

The disappearance of both the aggregates and the -phase occurs only upon solution heating above a transition temperature. The extent of polymer in the -phase can be quantified from the magnitude of the 437 nm absorption peak. To quantify the amount of -phase the absorption spectra were fit with two model spectra of the - and -phase. The model spectra were generated from a singular value decomposition (SVD)[46, 47] of the kinetics spectra acquired as a time series at 47°C shown in Figure 1.11. The SVD produced only two basis spectra with significant amplitude verifying the hypothesis that the overall spectrum was the result of two interconverting species. The spectra for the and species were produced from a linear combination of the two significant basis spectra. The -phase spectrum was one of the basis spectra and it exactly matched that of the fully heated solution. The -phase was based primarily on the second basis spectrum.

23

A small portion of the first basis was added to the second such that it had no negative amplitude. A linear combination of these two spectra could be used to fit all the spectra in the kinetics decay. A representative fit is shown in Figure 1.11, which is of an unheated PFO solution in toluene. The dashed line is the -component and the dotted line is the -component. The solid line is the actual data and the composite fit is indistinguishable. The portion of the sample in the -phase could then be calculated from the amplitude of the -component in the fit of any given spectrum. The fraction of the sample in the -form was estimated to be ~25%. Similar analysis showed only 3.6% of this original fraction of -phase returned upon cooling to -78°C for 40 minutes, these results are summarized for all the solvents in Table 1.1.
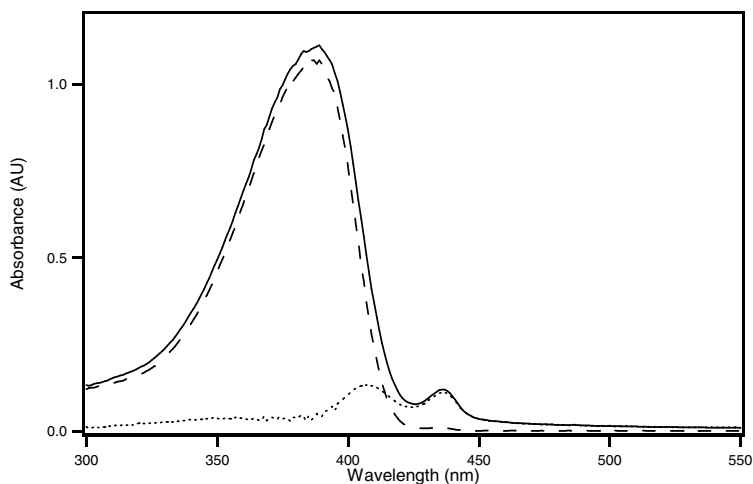
Figure 1.11 Singular value decomposition calculation of an aggregated and heated PFO solution in toluene. The solid line is original absorption spectrum of the aggregated solution. The dashed line is the absorption spectrum of the β-phase and the dotted line is the calculated absorption spectrum of the β-phase.

The fraction of this maximum -phase component can be measured as a function of temperature upon heating the original solution. The -phase component can be determined by fitting spectra at each temperature. Figure 1.10 shows the absorption

spectrum of PFO in the β-phase for a toluene solution. At temperatures around room temperature, the solution maintains its maximal β-phase component. As the solution is heated the β-phase component disappears sharply around 53°C. The rapid change is reminiscent of a phase transition or a collective polymer transition. Previously, Monkman *et al.* quantified the β-phase formation at lower temperatures in a similar fashion treating the change as an equilibrium process between the α and β-phase segments. Such a treatment yields a ΔH of -74.48 kJ mol^{-1} and a ΔS of -284.5 J K^{-1} mol^{-1} in MCH at ~-18°C for the formation of the β-phase.[30] However, such an analysis is very difficult to interpret. It is not clear what constitutes an α or β-phase in this "reaction." Is it a monomer, several monomers, or a polymer chain? Without this knowledge it is impossible to interpret the "per mol" in thermodynamic quantities. The study by Monkman *et al.* implied these quantities are per mole monomer, but this is only one limit. As the absorbance results from the extended conjugation across several monomer units this would be a more natural choice. However, given that it is not clear exactly how many units make up a "chromophore;" this leads to an ambiguity in what is defined as a mole of the α- and β-phases.

Like the formation, the disappearance of the β-phase could be interpreted as an equilibrium process, but unlike the formation the dissolution is found to have a large hysteresis in the transition. If the solution is heated until all the absorbance at 437 nm has gone to zero and then cooled to room temperature, none of the β-phase absorbance returns unless the sample is cooled to extremely low temperatures. The same is true if the sample is heated until only half of the 437 nm absorbance is gone, and once this solution returns to room temperature the amount of β-phase does not change and the remaining α-phase does not cause more to form. This would indicate that the thermodynamically

stable state at room temperature is the fully solvated chain in the -phase, and that any polymer that remains in the -phase is trapped in the polymer aggregates.

However, we can learn something about the enthalpy of the   to -transition from the calorimetry. The total heat from converting the polymer from the -phase in the aggregates to the -phase in solution can be measured. The total heat measured using the DSC was 0.1353 J g^{-1} of solution.   The PFO solution is 1 wt% polymer, yielding an enthalpy of 13.53 J g^{-1} of polymer. Using the estimate that 25% of the polymer is in the aggregated form, the transition energy is 54.12 J g^{-1} of aggregated polymer. This number can be converted to an enthalpy that is per mol monomer with the molecular mass of the monomer unit. This yields a transition enthalpy of 21.04 kJ mol^{-1} of monomer. The transition at 53 °C does not correspond to any transition for solid PFO itself, since the lowest temperature transition observed was an endothermic transition at 157 °C. This enthalpy is three times less than that extracted from the equilibrium measurement for the -phase formation.[30] In addition, the total enthalpy measured in the DSC is not simply the   to   transition, but includes the break up of the aggregates and the solvation of the polymer chains. The enthalpy of this transition was also measured in THF solutions, yielding an enthalpy of 31.70 kJ mol^{-1} monomer. This transition is more endothermic as would be expected given that THF is a worse solvent for PFO. The transition will require more heat because there is a less favorable solvation energy for the polymer chains in THF. This   to   transition is at the same temperature despite the differences in the solvent quality.

Solvent quality has the strongest affect on the -phase formation. In all the solvents except $CHCl_3$, if the sample is cooled to a much lower temperature the -phase was observed to return. In concentrated solutions (1 wt%) this leads to gelation whereas in dilute solutions the PFO concentration is not high enough to sustain a gel. The

temperatures at which the -phase are observed to return in the UV-Vis are tabulated in Table 1.1. For the two solvents measured in the DSC, the to -phase transition temperatures are nearly identical to the gelation temperature measured in the calorimeter, indicating that a common process is associated with both the return of the -phase and the gelation. The transition temperature for different solvents for the formation of the -phase demonstrates a clear trend with solvent quality. For the poorest solvent, cyclohexane, the transition is at the highest temperature, 10 °C; however, this transition temperature is just above the solvent's freezing point (7 °C). For the best solvent, chloroform, the -phase does not reform at any temperature, though, the cooling range is limited by CHCl$_3$'s freezing point, -65 °C. The intermediate solvents show that the better solvent, toluene, reforms at -55 °C and THF at -25 °C. The total amount of -phase reformed also depends on the solvent quality. The poorer solvents exhibited a greater amount of -phase returning upon cooling to the transition temperature. This is likely due to greater aggregation in the poor solvents. By simply looking at the Hildebrandt parameters it would appear that if CHCl$_3$ is the best solvent, and then THF should be a better solvent than toluene.[34, 35] However, one can just as easily argue the opposite trend for THF and toluene, utilizing a three dimensional solvation parameter such as the Hansen parameters. Toluene and THF are clearly both moderately poor on either solvation scale placing them between the best solvent chloroform and the worst solvent cyclohexane. The trend in solvent quality can be seen in the cooling transition in Table 1.1. The worst solvent converts to -phase at 10 °C, the intermediate solvents at -25 °C and -55 °C, and in the best solvent it never returns. As the -phase is not stable in any solvent at room temperature, it requires stabilization by either a meta-stable gel or aggregates to prevent it from converting back to the -phase. Cooling the solutions at a low temperature for longer generally produces more -phase, while a larger fraction of -

phase could also be reformed if the solvent was cooled significantly below the transition temperature. This was possible in only THF as the other solvents had freezing points close to the polymer phase transition. If the THF was cooled to -78 °C a full 37% of the α-phase could be converted to the β-phase.

The calorimetry of the gels exhibited similar trends to the aggregated solutions. Both gels were formed from concentrated solutions outside the calorimeter and their melt and β-phase reformation were studied in the calorimeter. The gels exhibited an endothermic peak associated with the melting of the gel upon initial heating. The first heat cycle of the gel melt transition occurs at a slightly lower temperature as the β to α-phase transition in the aggregated solutions. However, the enthalpy of the transitions was larger as it includes both the gel melting and β to α transition. Previous studies examining the melting of the PFO gels in cyclohexane did not observed this sharp melting transition.[35] However, this study followed the β-phase in thin films cast from a gel that was heated to 190 °C, and considering that the boiling point of cyclohexane is 81 °C, this indicates that a significant portion of the solvent would evaporate before the β to α transition. The evaporation of cyclohexane would greatly slow the transition and eliminate the sharp temperature response.

The dilute and concentrated solutions both show the appearance of the β-phase at the cooling transition temperature, but only the concentrated solution gels. Therefore, it is reasonable to conclude that the gelation is not responsible for the β-phase, but instead the β-phase forms and then gelation occurs. In a similar fashion, aggregation was found not to be responsible for the β-phase in dilute solutions of MCH.[30] The appearance of the β-phase in dilute solutions in the absence of aggregation has been interpreted to indicate that intermolecular interactions are not responsible for the formation of the β-phase. While this rules out interactions from other chains, it does not rule out intramolecular

interactions of the chain with itself. As the temperature is lowered the solvent quality decreases until at some temperature the chains collapse on themselves to reduce solvent contact. For poorer solvents the point where the chains collapse on themselves will occur at higher temperatures than for good solvents.[48] This is the same trend that is observed for the solvent effects for the -phase formation. This implies that a collapse of the polymer chain leads to stronger interactions between the chain and itself, and it is these interactions that lead to the change in backbone conformation. Theoretically such a collapse could be monitored by light scattering. Unfortunately the propensity for the polymer to aggregate after collapsing precludes the effective measurement of the hydrodynamic radius of the polymer as the measurement is dominated by the large aggregates.

In the absence of a change in the polymer chain conformation, it is unclear why solvent quality would have such a dramatic affect on the to transition. The two conformations should have very similar interactions with the solvent. A good solvent for the -phase should be a good solvent for the -phase. It is not clear why one phase would exhibit a dramatically different preference for one solvent over another. However, if the chain collapses, the polymer backbone experiences two distinct environments: one dominated by solvent-polymer interactions, and one in which there are significantly more interactions of the chain with itself. It is reasonable to deduce that the polymer in the collapsed state has more intramolecular interactions and this is the source of the to transition. When two chain segments are in close proximity they prefer the -phase conformation. This idea of the PFO chain folding back on itself is consistent with the sheet like model observed by Knaapila *et al*.[49]

CONCLUSION

This research has demonstrated that PFO solutions have a rich phase diagram with different conformations of both the polymer chain and the polymer backbone. The chains can be either in a freely solvated -phase or in a collapsed state with a large -phase component. The -phase segments tend to aggregate at lower concentrations while in more concentrated solutions, they lead to gelation. The thermodynamics of the - to - phase transition are complicated by meta-stable aggregates and the gelation, both of which cause a large hysteresis in the transition. The calorimetry reveals that the enthalpy of the transition from an aggregated -phase to a fully solvated -phase chain is 21.04 kJ mol^{-1} monomer in toluene and 31.70 kJ mol^{-1} monomer in THF. This is significantly lower than the enthalpy reported for the reverse transition in MCH.[30] This discrepancy could be due to a difference in the per mole quantity of the enthalpy. The ambiguity in the enthalpy derived from the calorimetry arises from the quantification of the fraction of the polymer originally in the -phase. The ambiguity in the number extracted from the equilibrium constant is the definition of per mole - or - phase. Those experiments measured the concentration from the lowest energy electronic absorption in the polymer, which results from a delocalized state conjugated over several monomers. Taking six monomer units as the conjugation length,[50] the enthalpy Monkman *et. al.*[30] calculated would be converted to 12.5 kJ mol^{-1} monomer. This is significantly closer to the current measurements of 25-30 kJ mol^{-1} monomer (depending on solvent quality). The current measurement is an upper limit of the -phase to -phase transition since it also includes the energy for the break up of the aggregates. The toluene enthalpy of 21.04 kJ mol^{-1} monomer is likely closer to the to transition as it has a smaller solvation enthalpy. If the previous equilibrium numbers obtained by Monkman *et. al.*[30] are assumed to be per mole conjugated segment, the seemingly large entropy change will also decrease by a

30

factor of six on a per monomer basis. This could be easily understood with a collapse of the polymer chain giving the to phase change. These ideas will be examined further with experiments that look at the dilute equilibrium in different solvents as well as how molecular weight shifts the transition. If the polymer collapse is the source of the to transition a clear reduction in the transition temperature should be observed for lower molecular weight polymers.

Polymer devices often utilize spin-cast films in which the polymer conformations are kinetically trapped in states similar to which they were in solution. The rich phase space, solvent dependence, and strong hysteresis observed in the polyfluorene system implies that a large variety of different morphologies can be made from processes that seem to be similar. The fact that subtle changes will arise from molecular weight and polymer defects in addition to solvent choice and processing history complicates matters. In conclusion, the results indicate that great care should be taken in reproducing studies of conjugated polymer films and solutions as the properties of solutions are easily changed by their processing conditions.

REFERENCE

1. Lin, W.-J.; Chen, W.-C.; Wu, W.-C.; Niu, Y.-H.; Jen, A. K.-Y., Synthesis and optoelectronic properties of starlike polyfluorenes with a silsequioxane core. *Macromolecules* **2004,** 37, 2335-2341.

2. Halkyard, C. E.; Rampey, M. E.; Kloppenburg, L.; Studer-Martinez, S. L.; Bunz, U. H. F., Evidence of aggregate formation for 2,5-Dialkylpoly(*p*-phenyleneethynylenes) in solutions and thin films. *Macromolecules* **1998,** 31, (25), 8655-8659.

3. Pei, J.; Liu, X.-L.; Chen, Z.-K.; Zhang, X.-H.; Lai, Y.-H.; Huang, W., First hydrogen-bonding-induced self-assembled aggregates of a polyfluorene derivative. *Macromolecules* **2003,** 36, 323-327.

4. Marsitzky, D.; Klapper, M.; Mullen, K., End-Functionalization of Poly(2,7-fluorene): A key step toward novel luminescent rod-coil block copolymers. *Macromolecules* **1999,** 32, 8685-8688.

5. Redecker, M.; Bradley, D. D. C.; Inbasekaran, M.; Woo, E. P., Mobility enhancement through homogeneous nematic alignment of a liquid-crystalline polyfluorene. *Applied Physics Letters* **1999,** 74, (10), 1400-1402.

6. Ranger, M.; Rondeau, D.; Leclerc, M., New well-defined poly(2,7-fluorene) derivatives: photoluminescence and base doping. *Macromolecules* **1997,** 30, 7686-7691.

7. Blatchford, J. W.; Jessen, S. W.; Lin, L.-B.; Gustafon, T. L.; Fu, D.-K.; Wang, H.-L.; Swager, T. M.; MacDiarmid, A. G.; Epstein, A. J., Photoluminescence in pyridine-based polymers: Role of aggregates. *Physical Review B* **1996,** 54, (13), 9180-9189.

8. Surin, M.; Hennebicq, E.; Ego, C.; Marsitzky, D.; Grimsdale, A. C.; Mullen, K.; Bredas, J.-L.; Lazzaroni, R.; Leclere, P., Correlation between the microscopic morphology and the solid-state photoluminescence properties in fluorene-based polymers and copolymers. *Chemistry of Materials* **2004,** 16, 994-1001.

9. Nguyen, T.-Q.; Yee, R. Y.; Schwartz, B. J., Solution processing of conjugated polymers: the effects of polymer solubility on the morphology and electronic properties of semiconducting polymer films. *Journal of Photochemistry and Photobiology A: Chemistry* **2001,** 144, 21-30.

10. Chuen, H.; Tanto, B.; Chunwaschirasiri, W.; Larson, B.; Winokur, M. J., Near-term aging and thermal behavior of polyfluorene in various aggregation states. *Applied Physics Letters* **2004,** 84, (1), 22-24.

11. Lim, E.; Jung, B.-J.; Shim, H.-K., Synthesis and characterization of a new light-emitting fluorene-Thieno[3,2-*b*]thiophene-based conjugated copolymer. *Macromolecules* **2003,** 36, 4288-4293.

12. Bliznyuk, V. N.; Carter, S. A.; Scott, J. C.; Klarner, G.; Miller, R. D.; Miller, D. C., Electrical and photoinduced degradation of polyfluorene based films and light-emitting devices. *Macromolecules* **1999,** 32, 361-369.

13. Leclerc, M., Polyfluorenes: Twenty years of progress. *Journal of Polymer Science, Part A: Polymer Chemistry* **2001,** 39, 2867-2873.

14. Sirringhaus, H.; Wilson, R. J.; Friend, R. H.; Inbasekaran, M.; Wu, W.; Woo, E. P.; Grell, M.; Bradley, D. D. C., Mobility enhancement in conjugated polymer field-effect transistors through chain alignment in a liquid-crystalline phase. *Applied Physics Letters* **2000,** 77, (3), 406-408.

15. Shikler, R.; Chiesa, M.; Friend, R. H., Photovoltaic Performance and Morphology of Polyfluorene Blends: The Influence of Phase Separation Evolution. *Macromolecules* **2006,** 39, 5393-5399.

16. Halls, J. J. M.; Arias, A. C.; MacKenzie, J. D.; Wu, W.; Inbasekaran, M.; Woo, E. P.; Friend, R. H., Photodiodes based on polyfluorene composites: influence of morphology. *Advanced Materials (Weinheim, Germany)* **2000,** 12, (7), 498-502.

17. Kim, J.; Swager, T. M., Control of conformational and interpolymer effects in conjugated polymers. *Nature* **2001,** 411, 1030-1034.

18. Nguyen, T.-Q.; Doan, V.; Schwartz, B. J., Conjugated polymer aggregates in solution: control of interchain interactions. *Journal of Chemical Physics* **1999,** 110, (8), 4068-4078.

19. Jenekhe, S. A.; Osaheni, J. A., Excimers and Exciplexes of Conjugated Polymers. *Science (Washington, D. C.)* **1994,** 265, 765-768.

20. Collison, C. J.; Rothberg, L. J.; Treemaneekarn, V.; Li, Y., Conformational Effects on the Photophysics of Conjugated Polymers: A Two Species Model for MEH-PPV Spectroscopy and Dynamics. *Macromolecules* **2001,** 34, (7), 2346-2352.

21. Schwartz, B. J., Conjugated Polymers as Molecular Materials: How chain conformation and film morphology influence energy transfer and interchain interactions. *Annual Review of Physical Chemistry* **2003,** 54, 141-172.

22. Bunz, U. H. F.; Imhof, J. M.; Bly, R. K.; Bangcuyo, C. G.; Rozanski, L.; Vanden Bout, D. A., Photophysics of Poly[p-(2,5-didodecylphenylene)ethynylene] in Thin Films. *Macromolecules* **2005,** 38, 5892-5896.

23. Kline, R.; McGehee, M., Morphology and Charge Transport in Conjugated Polymers. *Polymer Reviews* **2006,** 46, (1), 27-45.

24. Shu, C.-F.; Dodda, R.; Wu, F.-I.; Liu, M. S.; Jen, A. K.-Y., Highly efficient blue-light-emitting diodes from polyfluorene containing bipolar pendant groups. *Macromolecules* **2003,** 36, 6698-6703.

25. Klarner, G.; Lee, J.-I.; Lee, V. Y.; Chan, E.; Chen, J.-P.; Nelson, A.; Markiewicz, D.; Siemens, R.; Scott, J. C.; Miller, R. D., Cross-linkable polymers based on dialkylfluorenes. *Chemistry of Materials* **1999,** 11, (1800-1805).

26. Xia, C.; Advincula, R. C., Decreased aggregation phenomena in polyfluorenes by introducing carbazole copolymer units. *Macromolecules* **2001,** 34, 5854-5859.

27. Kulkarni, A. P.; Jenekhe, S. A., Blue light-emitting diodes with good spectral stability based on blends of poly(9,9-dioctylfluorene): Interplay between morphology, photophysics, and device performance. *Macromolecules* **2003,** 36, 5285-5296.

28. Khan, A. L. T.; Sreearunothai, P.; Herz, L. M.; Banach, M. J.; Kohler, A., Morphology-dependent energy transfer within polyfluorene thin films. *Physical Review B* **2004,** 69, 085201/1-085201/8.

29. Cadby, A. J.; Lane, P. A.; Wohlgenannt, M.; An, C.; Vardeny, Z. V.; Bradley, D. D. C., Optical Studies of Photoexcitation of poly(9,9-dioctyl fluorene). *Synthetic Metals* **2000,** 111-112, 515-518.

30. Dias, F. B.; Morgado, J.; Macanita, A. L.; da Costa, F. P.; Burrows, H. D.; Monkman, A. P., Kinetics and Thermondynamics of Poly(9,9'-dioctylfluorene) B-Phase Formation in Dilute Solution. *Macromolecules* **2006,** 39, 5854-5864.

31. Azuma, H.; Asada, K.; Kobayashi, T.; Naito, H., Fabrication of α- and β-phase poly(9,9-dioctylfluorene) thin films. *Thin Solid Films* **2006,** 509, 182-184.

32. Winokur, M. J.; Slinker, J.; Huber, D. L., Structure, photophysics, and the order-disorder transition to the beta phase in poly(9,9-(di-*n,n*-octyl)fluorene). *Physical Review B* **2003,** 67, 184106/1-184106/11.

33. Grell, M.; Bradley, D. D. C.; Ungar, G.; Hill, J.; Whitehead, K. S., Interplay of Physical Structure and Photophysics for a Liquid Crystalline Polyfluorene. *Macromolecules* **1999,** 32, 5810-5817.

34. Bradley, D. D. C.; Grell, M.; Long, X.; Mellor, H.; Grice, A., Influence of aggregation on the optical properties of polyfluorene. *SPIE* **1997,** 3145, 254-259.

35. Grell, M.; Bradley, D. D. C.; Long, X.; Chamberlain, T.; Inbasekaran, M.; Woo, E. P.; Soliman, M., Chain geometry, solution aggregation and enhanced dichroism in the liquid-crystalline conjugated polymer poly(9,9-dioctylfluorene). *Acta Polymerica* **1998,** 49, 439-444.

36. Skoog, D. A.; Holler, F. J.; Nieman, T. A., *Principles of Instrumental Analysis*. 5th ed.; Thomson Learning, Inc: Crawfordsville, MD, 1998.

37. Cowie, J. M. G., *Polymers: Chemistry and Physics of Modern Materials*. 2nd ed.; Blackie Academic & Professional: Glasgow, 1996.

38. Dunn, R. C., Near-Field Scanning Optical Microscopy. *Chemical Reviews* **1999,** 99, 2891-2927.

39. Vanden Bout, D. A.; Kerimo, J.; Higgins, D. A.; Barbara, P. F., Near-Field Optical Studies of Thin-Film Mesostructured Organic Materials. *Accounts of Chemical Research* **1997,** 30, 204-212.

40. Teetsov, J.; Vanden Bout, D. A., Near-field scanning optical microscopy (NSOM) studies of nanoscale polymer ordering in pristine films of Poly(9,9-dialkylfluorene). *Journal of Physical Chemistry B* **2000,** 104, 9378-9387.

41. Guenet, J.-M., On the molecular structure of isotatic polystyrene physical gel as revealed by differential scanning calorimetry and nuetron diffraction. *Macromolecules* **1986,** 19, 1961-1968.

42. Fang, J.; Kiran, E., Crystallization and gelation of Isotatic poly(4-methyl-1-pentene) in n-pentane and in n-pentane+CO_2 at high pressures. *Journal of Supercritical Fluids* **2006,** 38, 132-145.

43. Guenet, J.-M., *Thermoreversible Gelation of Polymers and Biopolymers*. Academic Press Limited: San Diego, 1992.

44. Nuemann, B., On the Aggregation behavior of Pseudoisocyanine Chloride in Aqueous Solution as Probed by UV/vis Spectroscopy and Static Light Scattering. *Journal of Physical Chemistry B* **2001,** 105, 8268-8274.

45. Chen, S. H.; Su, A. C.; Chen, S. A., Noncrystalline phases in poly(9,9-n-octyl-2,7-fluorene). *Journal of Physical Chemistry B* **2005,** 109, (20), 10067-10072.

46. Saltiel, J.; Eaker, D. W., Principal Component Analysis Applied to 1-Phenyl-2-(2-naphthyl)ethene Fluorescence. Four Components not Two. *Journal of the American Chemical Society* **1984,** 106, 7624-7626.

47. Kulcsar, A.; Saltiel, J.; Zimanyi, L., Dissecting the Photocycle of the Bacteriorhodopsin E204Q Mutant from Kinetic Multichannel Difference Spectra. Extension of the Method of Singular Value Decomposition with Self-Modeling to Five Components. *Journal of the American Chemical Society* **2001,** 123, 3332-3340.

48. Rubinstein, M.; Colby, R. H., *Polymer Physics*. Oxford University Press: Oxford, 2003.

49. Knaapila, M.; Garamus, V. M.; Dias, F. B.; Almasy, L.; Galbrecht, F.; Charas, A.; Morgado, J.; Burrows, H. D.; Scherf, U.; Monkman, A. P., Influence of Solvent Quality of the Self-Organization of Archetypical Hairy Rods-Branched and Linear Side Chain polyfluorenes: Rodlike Chains versus "Beta-Sheets" in solution. *Macromolecules* **2006,** 39, (19), 6505-6512.

50. Ng, M.-F.; Sun, S. L.; Zhang, R. Q., A comparative study of optical properties of poly(9,9-dioctylfluorene) and poly(*p*-phenylenevinylene) oligomers. *Journal of Applied Physics* **2005,** 97, 103513/1-103513/6.

Chapter 2: Fluorescence Lifetime Imaging NSOM of Mixed PFB/F8BT Films

INTRODUCTION

Conjugated polymers have been extensively studied for use in a number of electronic devices including: light emitting diodes (LEDs),[1-6] photovoltaics,[7-9] and transistors.[10] Specifically, researchers have become more interested in photovoltaics due to the increasing need to find alternative energy sources.[11] An advantage to using conjugated polymers in photovoltaics is the ease of solution processing, making them an inexpensive alternative to the traditional silicon based technology. A variety of different types of conjugated polymers have been studied for use in these devices; however, the polyfluorenes, which are a specific conjugated polymer family, have shown promise for making devices.[12] Of recent interest is the mixing of two different polyfluorene copolymers to increase the device efficiency, where one polymer is a good hole transporter and the other is a good electron transporter.[9]

Mixing the two different polymers together in the same solvent and then spin casting from the solution results in phase separated domains.[9, 13, 14] The phase separated domains occur during spin casting because one of the copolymers is slightly more soluble in the solvent than the other.[15, 16] Then after being spin cast into a film, the solvent begins to evaporate and the copolymer that is less soluble begins to phase segregate from the other making domains in the film, rich in one polymer or the other.[17] At the heterojunction between the domains the two polymers remain mixed and create an area where electron-hole pairs can be separated.[16] The electron-hole pairs are generated by light absorption that can then subsequently migrate in the material over distances of 10 nm. This means for an exciton to migrate to a heterojunction the phase segeration must

be on the order of 10's of nanometers to separate charges efficiently. Changing the morphology of the films, affects the heterojunctions, leading to an increase or decrease in the device efficiency.[14, 17-19] These changes in the film morphology can depend on solution composition, spin cast speeds used, solvent, temperature of substrate or solution.[12, 15, 17]

Currently, the two conjugated copolymers of specific interest are poly(9,9-di-*n*-octylfluorene-*alt*-benzothiadiazole) (F8BT) and poly(9,9'-di-*n*-octylfluorene-*alt*-bis-N-N'-(4-butylphenyl)bis-N,N'-phenyl-1,4-pheylenediamine) (PFB), which have shown promise for use in photovotaics.[9, 14, 17] In F8BT/PFB mixtures, the F8BT has a higher electron affinity, while the PFB has a high mobility for hole transport.[9, 14] These polymers were chosen due to the offset of their HOMO and LUMO relative to the other polymer. In addition, polymer blends of F8BT/PFB have been studied using near-field scanning optical microscopy (NSOM),[13, 16] scanning transmission X-ray microscopy (STXM),[20] atomic force microscopy (AFM),[11, 12, 14, 15, 17] and scanning Kelvin probe microscopy (SKPM).[18]

PFB

F8BT

38
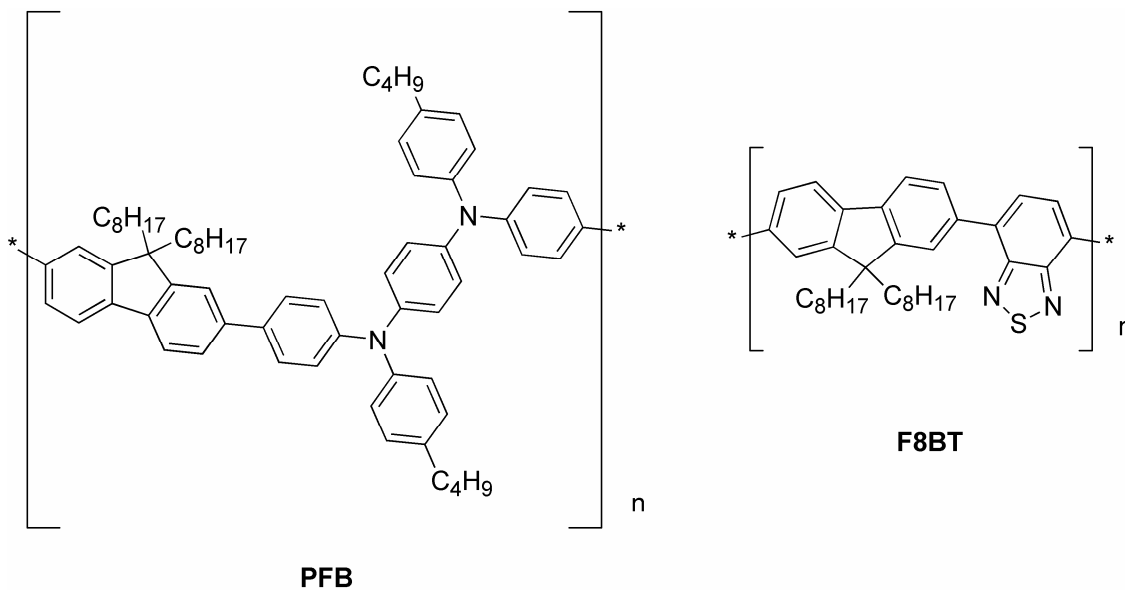
In this chapter, we used fluorescence lifetime imaging near-field scanning optical micrsocopy (FLI-NSOM) to investigate F8BT/PFB polymer films and to obtain lifetime decays in the nanoscale domains. Lifetime decays of pure F8BT and pure PFB films were taken in the far-field as a comparison to the mixed films. Ideally, the samples would be excited at a wavelength where both polymers absorb, such as 400 nm; however, we found that almost no fluorescence could be collected at this wavelength even in the near-field and with long integration times. Therefore, to obtain enough counts to be detected, the mixed polymer films were excited at 440 nm, which is near the absorption maximum of F8BT, but at a minimum for PFB. At this wavelength, we were able to obtain more fluorescent images. The topography image showed ordered domains, similar to what other researchers have observed and the fluorescence images showed regions of greater fluorescence for one polymer than the other. It is anticipated that the lifetimes of the two different regions will have the same lifetime decays of their pure film, but at the heterojunction a mixture of the lifetime decay should be observed.

EXPERIMENTAL

Materials

Poly(9,9 '-dioctylfluorene-co-benzothiadiazole   (F8BT)   and   poly(9, 9 '-dioctylfluorene-co-bis-N,N '-(4-butylphenyl)-bis-N,N '-phenyl-1,4-phenylenediamine) (PFB) were used as purchased from American Dye source.

F8BT/PFB films

A 1:1 mixture of 15 mg/mL PFB and 15 mg/mL F8BT was made in p-xylene. An aliquot of the mixture was then spin casted onto a cleaned coverslip at a rate of 1000 rpm. The sample was then allowed to air dry prior to use.

Time correlated single photon counting (TCSPC) setup

TCSPC data was collected in the far-field using a PicoQuant PicoHarp 300 card with 4 ps resolution. A frequency doubled Ti-Sapphire laser was utilized to excite the sample at either 400 or 440 nm. The laser pulses at 81 MHz (12 ns) and the pulses were synched with the TCSPC system using a photodiode, which acted as the stop pulse. The fluorescence from the sample was collected on a micro photon device (MPD), which acted as the start pulse. The MPD was coupled to the PicoHarp 300 card. The fluorescence lifetimes were collected using the PicoQuant software.

TCSPC Technique

In TCSPC, the instrument is able to detect single fluorescent photon events. The basic principle of the instrument measures the time difference between a start and stop pulse and then bins the photons at the correct times. This is possible by using a pulsed laser system that is monitored by a photodiode. When the laser excites the sample, a photon is emitted and collected on a detector (MPD). The emitted photon then starts the clock by signaling the time-to-amplitude (TAC) which triggers the voltage ramp. This voltage ramp is stopped when the next laser pulse is detected on the photodiode. This detection process is a reverse timing procedure. The TAC then provides a voltage that is proportional to the length of time between the start and stop pulses. Then a multichannel analyzer (MCA) converts the voltage recorded from the TAC to a specific time channel. The single photon events are then binned according to their arrival time. Upon averaging thousands of photons, a fluorescence lifetime decay can be constructed.

Fluorescence lifetime imaging near-field scanning optical microscopy (FLI-NSOM)

Lifetime images of the PFB/F8BT films were collected using the TCSPC setup described above. The NSOM ECU was connected to the TimeHarp 100 card to act as an

external clock. The lifetime images were collected simultaneously with the NSOM images using the continuous mode function in the TCSPC software. It was determined that the number of bins should be no larger than 277 or the software would not have enough memory to store the entire image. The bins are directly related to the collection window's time range, the larger the time range the more bins are collected. The resolution of the NSOM image is also important for FLI, the resolution corresponds to the number of blanks that needs to be inputted into the continuous mode window. The number of blanks is equal to the number of pixels divided by 32. For a 200 resolution NSOM image, there are 40,000 pixels; therefore, the number of blanks is 1250. The following picture is an example of FLI-NSOM setup.

FLI-NSOM Technique

Fluorescence lifetime imaging (FLI) NSOM is a technique that allows for the collection of time resolved florescence to be obtained per pixel at the same time a fluorescence near-field image is collected. The FLI uses the same principle as described in the TCSPC technique section above. The current NSOM setup, described in Chapter 3, was modified to enable FLI imaging as well as the traditional topography and fluorescence imaging. Figure 2.1 shows the current FLI-NSOM setup. A frequency doubled Ti-Saph laser at 440 nm, emits pulses at an 81 MHz frequency and is used to excite the sample, as well as the stop pulse. In order to detect the stop pulses, a beamsplitter after the frequency doubling crystal was used to reflect a portion of the laser light to a photodiode. The photodiode was then coupled into the TimeHarp 100 timing card located in a separate PC and synched with the laser pulses. The start pulse is obtained using a multi photon device (MPD) in place of an APD. The MPD is able to collect photons for use in real time fluorescence images as well as acting as the start pulse for time resolved measurements. The sample is excited by coupling the laser light into a

41

fiber optic tip that has been mounted onto a tuning fork (described in Chapter 3). The tip is then brought into feedback with the sample raster scanned. Topography, fluorescence, and time resolved measurements can then be obtained simultaneously on a per pixel basis. As the sample is excited, the photons detected on the MPD starts the clock and the clock is stopped when a laser pulse reaches the photodiode. During scanning the PicoQuant software is operated in continuous mode, which uses an external clock from the NSOM to determine how long lifetime decays are collected at each pixel. By obtaining lifetime decays at each pixel, it is possible to detect different lifetimes for different parts of the sample. In the current study, a polymer mixed film containing PFB/F8BT was studied because it forms phase separated domains that potentially have different lifetimes.
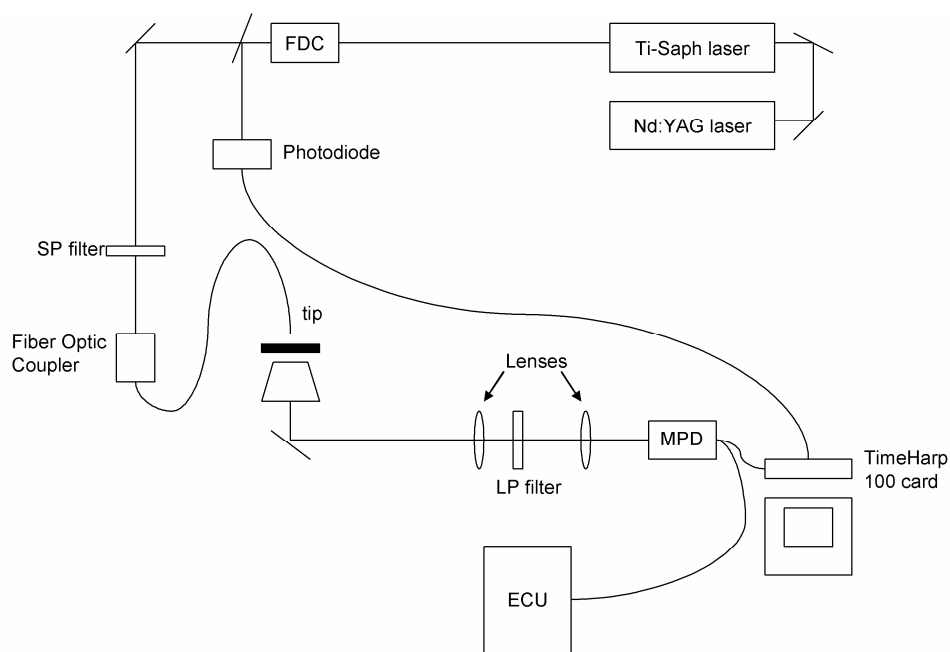
Figure 2.1   The current FLI-NSOM set up. Abbreviations: SP, short pass; FDC, frequency doubling crystal; LP, long pass; MPD, micro photon device.

RESULTS AND DISCUSSION

Fluorescence lifetime decays were taken of pure F8BT and PFB films in the far field to use as a comparison to the mixed F8BT/PFB films lifetimes. The pure films were both excited at 400 nm, which is near the maximum of PFB (λ_{max}= ~320 nm) and near the minimum of F8BT (λ_{max}= ~470 nm). The lifetime of the pure F8BT was found to fit a two exponential decay, with a fast and slow component. The fast lifetime had a decay of 0.917 ns (A_1= 1181 counts) and the slow component had a decay time of 24.1 ns (A_2= 14.47) (Figure 2.2a). When the pure PFB sample was excited at the same wavelength, it had a two exponential decay as well but a faster lifetime. The slower component had a decay time of 1.134 ns (A_1= 33.8 counts) and a faster component with a decay time of 0.292 ns (A_2= 294 counts) (Figure 2.2b). Next, a lifetime decay was taken of a mixed F8BT/PFB film. As it turns out, the lifetime of the mixed film had almost the same lifetime as the pure PFB film (Figure 2.2c). The slow decay of the mixed film was 1.48 ns (A_1= 26.3 counts) and the fast decay was 0.351 ns (A_2= 441 counts).
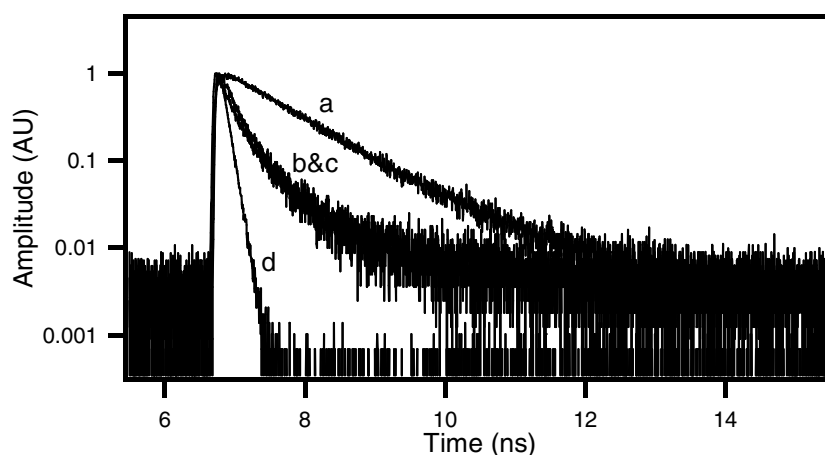
Figure 2.2.   Lifetime decays of a pure F8BT film (a), a pure PFB film (b), a mixed F8BT/PFB film (c), and the IRF (d) all excited at 400 nm.

The samples were not very fluorescent at 400 nm, so the same samples were excited with 440 nm light, which is closer to the fluorescence maximum of F8BT (λ_{max}= ~470 nm). When the pure F8BT film was excited at 440 nm, the lifetime decay still fit a two exponential decay with a slow component of 900 ps (A_1= 406 counts) and a fast component of 19.5 ps (A_2= 1380 counts) (Figure 2.3a). At 440 nm the absorption of PFB is at a minimum and so not much fluorescence is expected. Subsequently, when the pure PFB film was excited at 440 nm, the fluorescence decay captured ended up overlaying the IRF perfectly (Figure 2.3b). The same was true for a mixed F8BT/PFB film. The lifetime decay of the mixed film showed no true lifetime decay and looked more like the IRF (Figure 2.3c). Observing no lifetime decay for the pure PFB film when excited at 440 nm made sense because there was no absorption at that wavelength. However, there should have been a lifetime decay detected for the mixed film that was faster than the pure F8BT film since the film contained both F8BT and PFB. The lack of lifetime decay indicates that the PFB present in the film quenches any fluorescence of F8BT and therefore the lifetime decay is instrument limited.
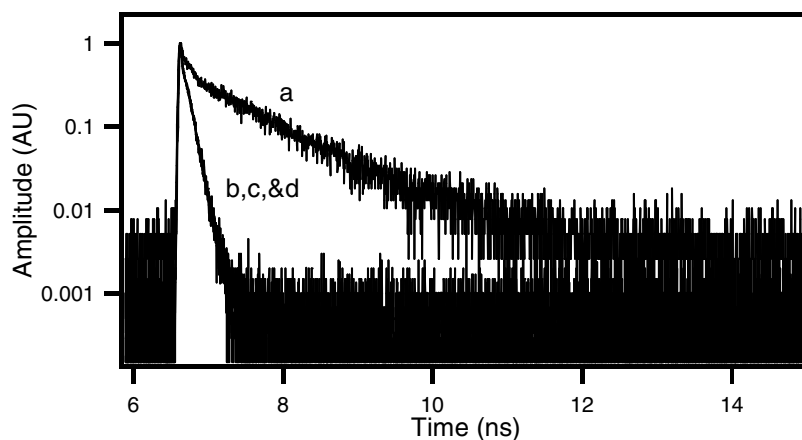
Figure 2.3   The fluorescence lifetime decays of a pure F8BT film (a), a pure PFB film (b), a mixed F8BT/PFB film (c), and the IRF (d).

44

The lifetime decays of the pure F8BT film excited at 400 nm and 440 nm were compared to determine if the excitation wavelength affected the lifetime decay. Figure 2.4 show both lifetime decays of pure F8BT. In Figure 2.4, the decays do not overlay one another, which is due to the differences in the IRF at the different wavelengths. However, the initial slopes of the decays are similar and when the lifetime decays are compared (τ_1=0.917 ns at 400 nm, and τ_1= 0.900 ns at 440 nm), they confirm that the excitation wavelength does not change the lifetime decay. There is a difference in the second lifetimes. When F8BT was excited at 400 nm, its second lifetime decay had a slower lifetime (τ_2= 24.1 ns), while the second lifetime decay of F8BT when excited at 440 nm had a much faster component (τ_2=19.5 ps). These differences could be due to scattered light or the differences in the IRFs at the different wavelengths.
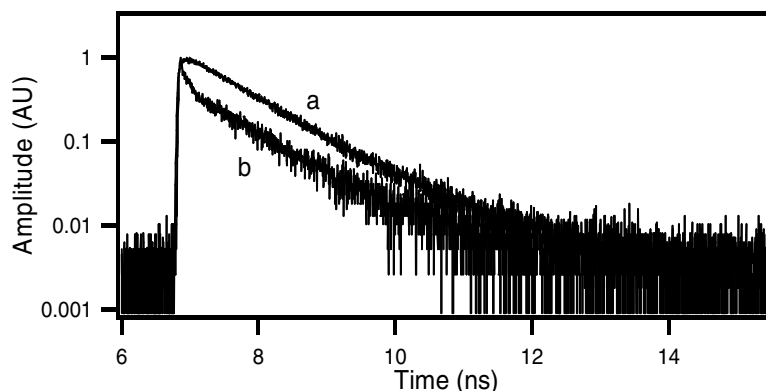
Figure 2.4   Lifetime decays of F8BT excited at 400 nm (a) and 440 nm (b).

FLI-NSOM was utilized to image a mixed F8BT/PFM film in order to look at its morphology and obtain fluorescence lifetime decays of the phase separated regions. Ideally the sample would be excited where both the F8BT and PFB can be excited, such as 400 nm. However, when the mixed polymer film was excited at 400 nm there is barely any fluorescence detected, even when the sample was being excited with the

evanescent field and long integration times were used. Therefore, the film was excited at 440 nm, which will excite only the F8BT. Figure 2.5 is the topography and fluorescence of the F8BT/PFB mixed film. The topography image showed phase separated domains that appear as spots. The lower lying areas of the film contain mostly PFB and the higher areas are mostly F8BT. The fluorescence image also showed domains. The lower lying domains in the topography corresponded with the dark spots in the fluorescence image, which is consistent with what should be observed for PFB when excited at 440 nm. While the higher lying areas are definitely F8BT rich.
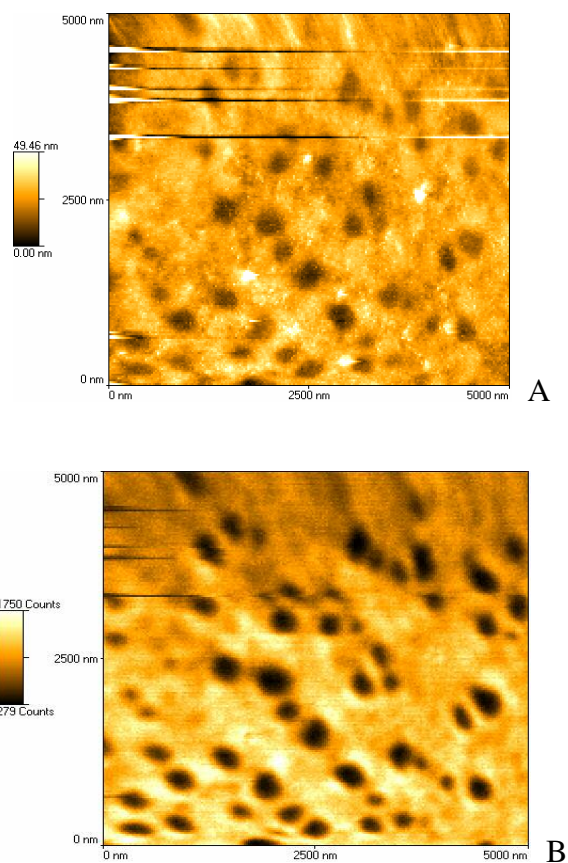
Figure 2.5   NSOM images of a mixed F8BT/PFB film excited at 440 nm. A) Topography image, B) Total fluorescence image.

Utilizing an IGOR routine written by Dr. Vanden Bout, we were able to form a lifetime image from all the decays collected at each pixel. The fluorescence lifetime image looks like the fluorescence image obtained from the NSOM (Figure 2.6). Average lifetimes were taken of the dark spots (PFB) and the bright spots (F8BT). The lifetime decay of the F8BT region was fit with a two exponential decay and had a slow component with a decay time of 1.151 ns (A_1= 31.76 counts) and a fast component with a decay time of 0.2496 ns (A_2= 708.7 counts) (Figure 2.6B). In contrast, the lifetime of the F8BT region in the mixed films is a faster lifetime than that of the pure F8BT film. The average lifetime decay of the PFB region was also fit with a two exponential decay and a slow component with a decay time of 1.149 ns (A_1= 31.91 counts) and a fast component decay time of 0.2492 ns (A_2= 710.4 counts) (Figure 2.6B). As it turns out, the lifetime decays for the dark spots and bright areas are the same, which can be seen in Figure 6B; that the lifetimes overlap almost perfectly, expect for tail end of the decays. This discrepancy could be due to differing dark counts. Since the lifetimes of the dark and the bright regions were almost identical, this confirms that the film did not fully phase separate with the regions of PFB in fact having some F8BT and vice versa. Similar results were observed by McNeil *et al.* who used scanning transmission x-ray microscopy to study TFB/F8BT thin films. They observed that in regions thought to be TFB rich actually had a large percentage of F8BT present and in F8BT regions a large percent was PFB.[20] Ideally, if the film had fully phase separated into regions solely of PFB and F8BT, then in the lifetime decays, we should have seen a lifetime resembling pure PFB in the dark regions and a lifetime decay resembling pure F8BT in the bright regions. Then at the heterojunctions between the two phases, the lifetime should be a mixture of the two. The lifetime at the heterojunction should be comprised of a fast component and a second longer decay that is due to the exciplex formation and it should have a decay time

47

of ~54 ns or longer.[19] The strong intermixing of the two polymers will lead to effective

charge separation, but lead to strong recombination and poor collection of charges.

A
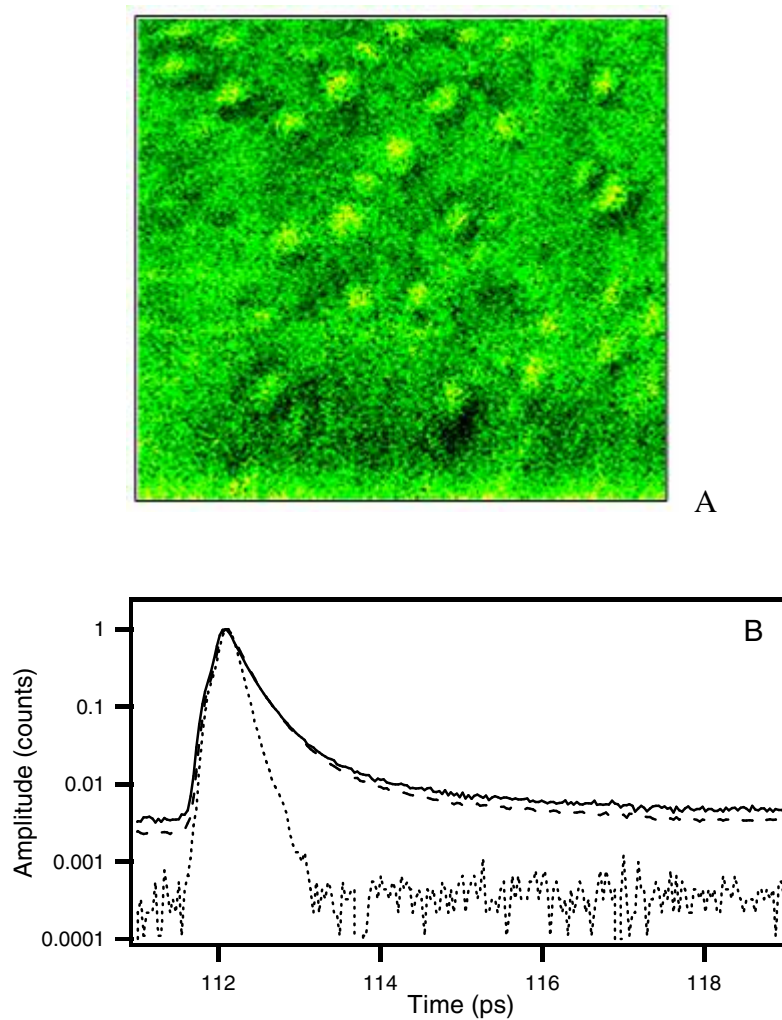
Figure 2.6   A) The fluorescence lifetime image of a F8BT/PFB film. B) Average
lifetime decays of the dark spots (solid line) and bright areas (dashed line).
The dotted line is the IRF.

CONCLUSION

In this chapter, we have demonstrated that FLI-NSOM is able to obtain high

resolution images of F8BT/PFB mixed films. Using an image analysis program, we were

able to extract average lifetime decays for areas either F8BT or PFB rich. However, upon fitting the lifetime decays, it was determined that they had the exact same lifetimes. The lifetime decays also did not show the long lived component from the exciplex, indicating that efficient charge separation had not taken place. However, this was consistent with what other researchers had observed in polymer blends of F8BT and PFB. Although the polymer film did not have different lifetimes in the various regions, we were able to demonstrate that FLI-NSOM is a powerful tool that can obtain information about the sample on the nanoscale. Future experiments would include photoconductivity measurements on these films and also trying to determine a better process to obtain more phase segregation.

REFERENCES

1. Bliznyuk, V. N.; Carter, S. A.; Scott, J. C.; Klarner, G.; Miller, R. D.; Miller, D. C., Electrical and photoinduced degradation of polyfluorene based films and light-emitting devices. Macromolecules 1999, 32, 361-369.

2. Chuen, H.; Tanto, B.; Chunwaschirasiri, W.; Larson, B.; Winokur, M. J., Near-term aging and thermal behavior of polyfluorene in various aggregation states. Applied Physics Letters 2004, 84, (1), 22-24.

3. Halkyard, C. E.; Rampey, M. E.; Kloppenburg, L.; Studer-Martinez, S. L.; Bunz, U. H. F., Evidence of aggregate formation for 2,5-Dialkylpoly(p-phenyleneethynylenes) in solutions and thin films. Macromolecules 1998, 31, (25), 8655-8659.

4. Lim, E.; Jung, B.-J.; Shim, H.-K., Synthesis and characterization of a new light-emitting fluorene-Thieno[3,2-b]thiophene-based conjugated copolymer. Macromolecules 2003, 36, 4288-4293.

5. Leclerc, M., Polyfluorenes: Twenty years of progress. Journal of Polymer Science, Part A: Polymer Chemistry 2001, 39, 2867-2873.

6. Nguyen, T.-Q.; Yee, R. Y.; Schwartz, B. J., Solution processing of conjugated polymers: the effects of polymer solubility on the morphology and electronic properties of semiconducting polymer films. Journal of Photochemistry and Photobiology A: Chemistry 2001, 144, 21-30.

7. Halls, J. J. M.; Arias, A. C.; MacKenzie, J. D.; Wu, W.; Inbasekaran, M.; Woo, E. P.; Friend, R. H., Photodiodes based on polyfluorene composites: influence of morphology. Advanced Materials (Weinheim, Germany) 2000, 12, (7), 498-502.

8. Shikler, R.; Chiesa, M.; Friend, R. H., Photovoltaic Performance and Morphology of Polyfluorene Blends: The Influence of Phase Separation Evolution. Macromolecules 2006, 39, 5393-5399.

9. Arias, A. C.; Corcoran, N.; Banach, M.; Friend, R. H.; MacKenzie, J. D.; Huck, W. T. S., Vertically segregated polymer-blend photovoltaic thin-film structures through surface-mediated solution processing. Applied Physics Letters 2002, 80, (10), 1695-1697.

10. Sirringhaus, H.; Wilson, R. J.; Friend, R. H.; Inbasekaran, M.; Wu, W.; Woo, E. P.; Grell, M.; Bradley, D. D. C., Mobility enhancement in conjugated polymer field-effect transistors through chain alignment in a liquid-crystalline phase. Applied Physics Letters 2000, 77, (3), 406-408.

11. Coffey, D. C.; Ginger, D. S., Time-resolved electrostatic force microscopy of polymer solar cells. Nature 2006, 5, 735-740.

12. Donley, C. L.; Zaumseil, J.; Andreasen, J. W.; Nielsen, M. M.; Sirringhaus, H.; Friend, R. H.; Kim, J.-S., Effects of packing structure on the optoelectonic and charge transport properties in poly(9,9-di-n-octylfluorene-alt-benzothiadiazole). Journal of the American Chemical Society 2005, 127, 12890-12899.

13. Cadby, A.; Dean, R.; Fox, A. M.; Jones, R. A. L.; Lidzey, D. G., Mapping the fluorescence decay lifetime of a conjugated polymer in a phase-separated blend using a scanning near-field optical microscope. Nano Letters 2005, 5, (11), 2232-2237.

14. Arias, A. C.; MacKenzie, J. D.; Stevenson, R.; Halls, J. J. M.; Inbasekaran, M.; Woo, E. P.; Richards, D.; Friend, R. H., Photovoltaic performance and morphology of polyfluorene blends: A combinded microscopic and photovoltaic investigation. Macromolecules 2001, 34, 6005-6013.

15. McNeill, C. R.; Frohne, H.; Holdsworth, J. L.; Dastoor, P. C., Near-field scanning photocurrent measurements of polyfluorene blend devices: Directly correlating morphology with current generation. Nano Letters 2004, 4, (12), 2503-2507.

16. Cadby, A. J.; Dean, R.; Elliot, C.; Jones, R. A. L.; Fox, A. M.; Lidzey, D. G., Imaging the fluorescence decay lifetime of a conjugated-polymer blend by using a scanning near-field optical microscope. Advanced Materials (Weinheim, Germany) 2007, 19, 107-111.

17. Snaith, H. J.; Arias, A. C.; Morteani, A. C.; Silva, C.; Friend, R. H., Charge generation kinetics and transport mechanisms in blend polyfluorene photovoltaic devices. Nano Letters 2002, 2, (12), 1353-1357.

18. Chiesa, M.; Burgi, L.; Kim, J.-S.; Shikler, R.; Friend, R. H.; Sirringhaus, H., Correlation between surface photovoltage and blend morphology in polyfluorene-based photodiodes. Nano Letters 2005, 5, (4), 559-563.

19. Morteani, A. C.; Friend, R. H.; Silva, C., Exciton trapping at heterojunctions in polymer blends. Journal of Chemical Physics 2005, 122, (24), 244906/1-7.

20. McNeill, C. R.; Watts, B.; Thomsen, L.; Belcher, W. J.; Greenham, N. C.; Dastoor, P. C., Nanoscale quantitative chemical mapping of conjugated polymer blends. Nano Letters 2006, 6, (6), 1202-1206.

AMYLOID FIBRILS

Chapter 3: Spectroscopy and Microscopy of Various Fluorescent Dyes Bound to Amyloid Fibrils

INTRODUCTION

Amyloid fibrils

Amyloidosis is associated with over 20 different neurodegenerative diseases, such as Alzheimer's, Creutzfeldt-Jakob, Huntington's, and Parkinson's diseases.[1-3] It occurs when normally soluble proteins polymerize and form insoluble, highly ordered aggregates, called amyloid fibrils, due to diverse biochemical conditions.[4] Amyloidosis is not just associated with neurodegenerative diseases, but is also known to form in other organs, such as the pancreas in diabetes patients.[4] The name amyloid was first used by Virchow in 1851, which means starch-like. Friedrich and Kekule later discovered that amyloid fibrils were mostly comprised of proteins and not starches like cellulose; however, the name amyloid was kept. Researchers, since the discovery of amyloid fibrils, have been trying to understand their structure and formation, in order to determine a means to prevent them from forming. Although extensive research has been done on amyloid fibrils, the cause of amyloid fibril formation still remains unclear.

Although the cause of amyloid fibrils is still unknown, the structure of the fibrils has been determined through X-ray diffraction, circular dichroism (CD), and electron microscopy (EM). The X-ray diffraction patterns showed simple repeat patterns with spacings that were characteristic of the cross β-sheet structure.[5] CD was used to monitor the protein unfolding and subsequent fibril formation as a function of time. Bouchard *et al.* observed that prior to heating an insulin solution, two minima at 208 nm and 222 nm

that are indicative of α-helical structure. Then upon heating the solution the two minima disappear and a new, singular minimum forms at 216 nm, and this minimum is characterized as containing all a -sheet structure.[6] EM was able to image the fibrils and found that the fibrils consisted had a diameter of ~7-12 nm and were of various non-branching lengths.[5, 7] The EM images also showed that the fibrils were twisted along the fibril axis. These techniques were able to determine the amyloid fibril structure, which is comprised of anti-parallel pleated -sheets that are oriented perpendicular to the fibril axis.[2, 4-9] A variety of proteins are known to form amyloid fibrils by heating and harsh conditions such as low pH and increased ionic strength; however, several of them are not disease related[7] and it is thought that amyloid formation is generic to all polypeptides.[9] Researchers have found that the protein's primary structure plays a minor role in the formation of amyloid fibrils and that proteins that form fibrils are not the same size, sequence, or secondary structure;[2] however, once they form amyloid fibrils they all share the same cross β-sheet structure.[4, 5]

The actual mechanism of fibril formation is still debated, but most scientists agree that the general mechanism is a nucleation polymerization reaction. For a nucleation reaction to occur a few requirements are needed: first, the monomer concentration must be above the critical concentration; second, there is a lag phase before fibrils will form; and third, the rate of the formation is dependent upon the protein concentration.[10] The reaction first occurs with the formation of a nucleus, which is formed when a protein monomer misfolds and attaches to other misfolded proteins forming the nucleus. Powers *et al.* determined that just prior to the nucleus formation was the peak of activation energy and upon formation of the nucleus the structure was stabilized and fibril formation occurred rapidly afterwards.[10] After the nucleus has formed then other misfolded monomers were able to attach to the nucleus causing elongation and the forming long

protofilaments. Then two or more protofilaments twist around one another to form protofibrils and then finally two or more protofibrils twist around one another to form mature fibrils.[7, 11] The coiling of the protofilaments around one another is possibly due to burial of the hydrophobic amino acids. This coiling forms a higher order fibril structure[7].

Spectroscopy as a means to study amyloid fibrils

The first use of spectroscopy in understanding amyloid fibrils was done by staining the fibrils with Congo red (CR) dye in 1922 by Benhold.[4] Later on polarization microscopy was incorporated by Divry and Florkin and they found that apple green birefringence was observed when viewed through cross polarizers.[12-17] The staining of CR provided a simple method to test for amyloid fibrils.[4] CR is a long symmetric molecule with two negatively charged sulfate groups and is still used today as an amyloid specific dye. The spectral properties of CR when bound to fibrils did not show much change in the excitation and emission, as it is not very fluorescent. Nevertheless, researchers did find that there was enhanced absorbance and a metachromic shift in the absorption spectrum.[13, 18] The CR orientation within a fibril was determined to be parallel to the fibril axis by Jin *et al.*, who looked at polarization in Alzheimer's disease plaques.[17] Although, CR has been observed to bind to amyloid fibrils, it has also been found to bind to proteins in their native conformation.[14, 19]

CR
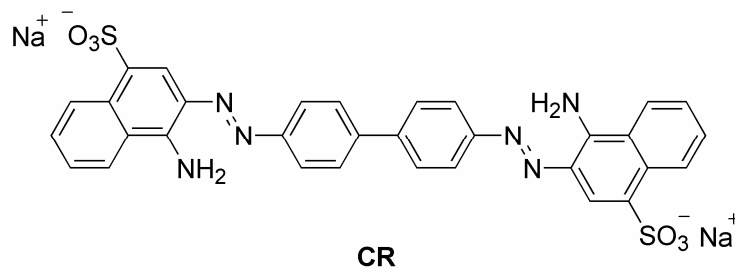
Thioflavin T was introduced by Vassar and Culling in 1959 as another amyloid specific dye. The ThT structure is very different from CR, it is a smaller positively

charged dye, and it was found to have a higher affinity and bind more selectively bind to amyloid fibrils than CR.[20] It also had a unique spectral properties upon binding to amyloid fibrils, which was an enhanced fluorescence signal was observed at ~480 nm.[21-26] There was also a red-shift in the excitation maximum to ~450 nm.[24, 27] Recently, Krebs *et al.* determined that the ThT molecule incorporated itself between the β-sheets and oriented itself parallel to the fibril axis.[21] One benefit of ThT is that it does not bind to proteins in their native conformations or in a partially folded state. Both ThT and CR have been found to bind with no distinction between the primary amino acid sequences and are thought to bind to different sites.
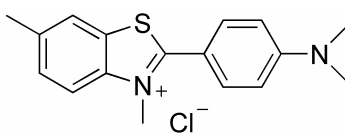
ThT

Although, CR and ThT have been used extensively for amyloid fibril characterization, scientists are always looking for different dyes that can be used for *in vivo* imaging. However, the biggest obstacle is trying to synthesize dyes that can pass through the blood/brain barrier. A family of uncharged benzothiazole derivatives has shown promise for this purpose. The uncharged benzothiazoles were found to have a higher binding affinity for amyloid fibrils than ThT.[28] Since these dyes are relatively new not much is known about their spectral properties. The benzothiazole dye specifically being used in this research is 2-[4'-(dimethylamino)phenyl]-benzothiazole.

BTA-2

55
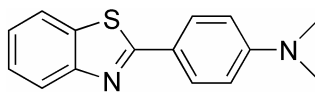
In this chapter, we will discuss in detail the spectroscopy and microscopy of three different dyes bound to bovine insulin amyloid fibrils, Congo red (CR), thioflavin T (ThT), and BTA-2. Bovine insulin is a relatively inexpensive protein that is known to form amyloid fibrils at low pH and high temperatures. The dyes, CR and ThT, have been extensively studied by other researchers and therefore we will use the known properties to gain a better understanding of how these dyes orient themselves within the fibrils. BTA-2 is a relatively new dye in the last 10 years and has been found to have a higher binding affinity than ThT,[28] but its spectral properties are relatively unknown. Absorption and fluorescence spectroscopy was used to study the effects of the dye binding on its electronic properties. Upon binding CR did not show any real change in its optical properties; however, it was used extensively in isothermal titration calorimetry binding studies, which are discussed in the next chapter. ThT spectral properties made it and ideal candidate for polarized near-field scanning optical microscopy (NSOM) studies, which were used to determine the orientation of the ThT dye within a single fibril. BTA-2 provided us with an alternative dye for our NSOM studies and had very interesting spectral properties depending on the solvent medium. Other microcopies were used such as atomic force microscopy (AFM) to look at the topography of fibril films and fluorescence microscopy to see the ThT fluorescence in fibrils while in solution.

EXPERIMENTAL

Materials

Gold seal coverslips were purchased through Fisher Scientific. Insulin from a bovine pancreas was used as purchased from Sigma-Aldrich and was stored at -20 °C in a desiccator. 3-aminopropylethoxy silane, 0.1% Poly(Lysine) solution in water, Congo

red, and Thioflavin T were used as purchased from Sigma-Aldrich with no further purification. BTA-2 was synthesized as described below.

Fibril formation

Fibrils were prepared by dissolving insulin in pH 2 water (0.5 mg/mL). The solution was then filtered through a 0.2 μm filter into a small vial, the solution was filtered to remove insulin not in the monomeric form. A stir bar was added to the solution and then Parafilm was placed around the cap to prevent evaporation. The solution was then placed in an oil bath and heated at 60 °C for 24 hours. After heating, the fibrils were allowed to cool to room temperature before centrifuging. The fibril solution was pipetted into an epindorf and centrifuged using an Eppendorf 5415R centrifuge at 3000 rpm for 2.5 min. The fibrils were centrifuged to remove any large globules. After centrifuging the supernatant was removed and pipetted into a new epindorf. Solutions were stored in a refrigerator (~10 °C) until needed; however, fibril solutions more than 10 days old were no longer used.

BTA-2 synthesis

BTA-2 was synthesized as described in literature by Alagille *et al.*[29] Further purification was done beyond the literature. First, the BTA-2 was dissolved in ethanol and then was filtered through a Buckner funnel to remove any undissolved particulates. Next nanopure water was added to the BTA-2/ethanol mixture until a shimmery, pale yellow precipitate formed. The precipitate was then filtered using a Buckner funnel, and then the solid was placed in a Petri dish to dry. The BTA-2 was characterized by ^{1}H NMR and high resolution mass spectrometry.

Fibril solutions

Fibril solutions used for ThT absorption and fluorescence studies were prepared by diluting a portion of the stock fibril solution with nanopure water and adding an aliquot of a 0.8 mg/mL ThT solution in water. ThT solutions were made by dissolving it into water or glycerin. Fibril solutions used for BTA-2 absorption and fluorescence studies were prepared three ways. The first solution was prepared by diluting an aliquot of the stock fibril solution with pH 2 water and then adding an aliquot of 0.9 mg/mL BTA-2 in CH_3CN. The second fibril solution used the same amount of stock fibrils and BTA-2, but was diluted with nanopure water. The third fibril solution was made again using the same amount of stock fibril solution and BTA-2, but was diluted with a 1:1 mixture of nanopure water: CH_3CN. The same three solutions containing BTA-2 alone were made the same way but without the fibrils.

Fibril solutions for fluorescence microscopy were made by diluting an aliquot of the stock fibril solution with nanopure water and then adding an aliquot of 0.8 mg/mL ThT solution in water. For NSOM samples, a fibril solution was made using an aliquot of the stock fibril solution and then diluted with pH 2 water and an aliquot of 0.9 mg/mL BTA-2 solution in CH_3CN. Fibril solutions for AFM studies were made by diluting a portion of the stock fibril solution with water at various concentrations.

Coverslip preparation

Coverslips were cleaned using a March Plasma CS1701F RIE etching system at 200 W and 35 sccm O_2 for 10 minutes. After cleaning the coverslips were used immediately.

Poly(Lysine) (PL) Coating

PL is comprised of positively charged amine groups, that coat the surface of the substrate in order to adhere biological samples. The cleaned coverslips were placed onto kimwipes to be functionalized with PL for fibril adhesion. A 10 uL aliquot of PL was pipetted onto the surface and then smeared all over the coverslip using the edge of another coverslip. Excess PL was dragged off the end of the coverslip onto a kimwipe. The coverslips were then covered with a Petri dish and allowed to air dry for 10 min.

Silanization

By silanating the surface of a coverslip, the silanes form covalent bonds with the glass surface's hydroxyl groups, while the positively charged amine groups stick out away from the surface. A 2% solution of 3-aminopropylethoxy silane (1 mL) and acetone (49 mL) was mixed in an oven dried glass jar with stopper. The acetone was dried using molecular sieve 24 hours prior to use. The acetone must be dry because the silanes will react with any water present. The silane solution was made fresh every time. Three Columbian jars and a beaker of deionized water were set out on the bench. The silane solution was poured into the first Columbian jar. The second Columbian jar contained dried acetone and the third Columbian jar contained deionized water. Four coverslips were placed in the first Columbian jar containing the silane solution for 1 min. The coverslips were then removed and placed in the Columbian jar containing the dried acetone for 1 min. After 1 min, the coverslips were then transferred to the Columbian jar containing the deionized water for 1 min. Finally each coverslip was dipped vigorously in the beaker of deionized water to ensure that they were completely rinsed off. The coverslips were then allowed to air dry under a Petri dish. Note, if the coverslips have white streaks or spots they were not rinsed well enough and the procedure will need to be repeated with clean coverslips. Also, once the coverslips are functionalized, care should

be taken to avoid touching them with bare hands because this will defunctionalize the silanes and then the fibrils will not bind to them.

Fibril Adhesion

This procedure can be used on either silanated coverslips or PL coated coverslips. Once the functionalized coverslips are dry a previously prepared fibril solution (see above) was pipetted all over the surface of the coverslip (if the coverslips are uniformly functionalized they should be hydrophilic and the fibril solution should be uniformly wetted across the film). The samples were covered and left alone for 10 min. They were then gently rinsed in a Petri dish of deionized water to remove any excess solution and fibrils. The samples were then placed on a Kimwipe and covered with a Petri dish to prevent dust from settling on the sample and allowed to air dry.

Absorption Spectroscopy

Absorption spectra were obtained using a Beckman DU 7400 UV-Visible Diode-array spectrophotometer. The spectra were collected using a 1.5 mL volume Starna quartz cuvette with a path length of 1 cm (this cuvette was also used for fluorescence spectroscopy).

Fluorescence Spectroscopy

Fluorescence and anisotropy measurements were acquired using a Photon Technologies International Quanta Master Model C Cuvette based scanning fluorometer. Bandpass filters of appropriate wavelength were used to ensure a monochromatic excitation beam. Long pass filters were used in the emission path to help eliminate scattered excitation light. For anisotropy measurements, polarizers mounted on a rotation stage were placed in the excitation and emission path. The following polarizations were collected: HH, HV, VH, VV (H=horizontal polarization, V=vertical polarization), where

the first letter denotes the polarization of the excitation and the second letter is the polarization of the emission. The G-factor of the instrument was determined by dividing the intensity of the HV polarizations by the intensity of the HH polarizations for each wavelength. The anisotropy was calculated for each wavelength using the following equation:

$$r = \frac{I_{VV} - (G * I_{VH})}{I_{VV} + (2 * G * I_{VH})}$$

Fluorescence Spectroscopy of Fibril Films

The three fibrils solutions made with BTA-2, described above, were made into films. Coverslips were cleaned, coated with poly(lysine), and the fibrils attached to the surface. Once the samples were dry, fluorescence spectra were taken obtained for all three using a home-built sample scanning inverted microscope. The samples were excited with a 405 nm CW laser by illuminating the sample off a dichroic mirror and through a 1.25 numerical aperture microscope objective. The sample fluorescence was collected through the same microscope objective onto a spectrometer (Acton) equipped with a CCD camera (Princeton Instruments, LN-400EB).

Time Correlated Single Photon Counting (TCSPC)

TCSPC lifetimes were taken on an EG&G Ortec TRUMP-PCI Multichannel analyzer. The fibril solutions and ThT in glycerin were excited at 440 nm by a Spectra-Physics Ti-Saph laser that was frequency doubled using a second harmonic generator. A 440 nm band pass (BP) filter was placed in the excitation path to ensure the excitation was at the correct wavelength. A 500 nm BP filter was place in the emission path before the MCP. A mounted polarizer on a rotation stage was in the emission path and was set to the magic angle of 54.7°. Lifetime data of fibrils with ThT, and ThT in glycerin were

collected at the magic angle. An instrument response function (IRF) lifetime was taken at the end of the day. The lifetime data of the fibril samples with bound ThT were collected for 2 min. While lifetime data of ThT in glycerin was collected for 1 min. The time per channel was ~23.2 ps. Lifetime data was analyzed in PicoQuant's FluoroFit software program.

Near-field Scanning Optical Microscopy (NSOM)

Near-Field Optical Microscopy (NSOM) images were collected using an Aurora system (Thermomicroscopes/Veeco). A frequency doubled Ti-Sapphire laser was utilized to excite the sample at either 400 or 440 nm. Near-field probes were manufactured in-house and mounted on piezo-electric tuning forks for shear-force feedback. Samples containing BTA-2 were excited at 400 nm and the fluorescence of was collected through a 418 nm long pass filter and then split using a polarizing beam splitter onto an avalanche photo-diode (APD) and a micro photon device (MPD). The MPD also collected lifetime data. Samples containing ThT were excited at 440 nm and the fluorescence was collected through a 455 nm long pass filter and then split using a polarizing beam splitter onto two APDs.

NSOM Technique

NSOM is a powerful technique that can be used to gain topographical information and optical information concurrently. NSOM is able to image samples with a higher spatial resolution than other optical microscopy techniques because it is able to resolve beyond the traditional diffraction limit. Typical far field optical microscopy has a resolution limit of half the wavelength of light used; however, in NSOM the resolution is determined by the size the tip aperture and not the wavelength of light used. A NSOM tip is a coated, pulled fiber optic tip with a subwavelength aperture ideally between 50-

62

100 nm.   When the confined light exits the subwavelength aperture, it forms an evanescent field, which has an illumination distance of ~10nm from the end of the tip before it quickly diverges.   Therefore in order to excite in the near-field the tip must be brought into close proximity to the sample.

In order to obtain high resolution NSOM images, a good quality NSOM probe is needed.   NSOM probes are made using a micropipette puller, which heats a fiber and then pulls it to a very small tip.   The tips are then coated with aluminum in a thermal evaporator.   The tips are checked after coating by coupling a red HeNe laser into the fiber optic in order to ensure that they have an aperture and that no pinholes are present. However, the size of the aperture can not be quantitatively determined without using a scanning electron microscope (SEM).   Figure 3.1 is a SEM image of a coated tip.   After characterizing, a good tip will be mounted onto a high frequency tuning fork.   When placed into the NSOM, a good tip should have a high quality factor (or Q).   The quality factor is resonance quality of the tip and is calculated by dividing the maximum frequency by the full width at high maximum.   Generally, a Q-factor higher than 300 is considered good.
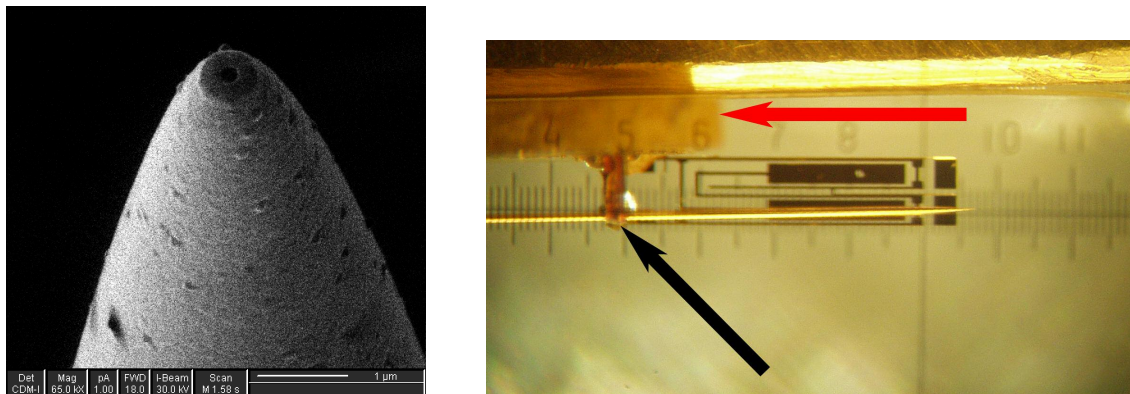
Figure 3.1   Left image is a SEM image of an aluminum coated near-field tip. The right
image is of a near-field tip being mounted onto a tuning fork (picture was
taken by Kevin Channon from Cavendish Laboratory).

The basic NSOM operation implores a feedback loop in order to keep the tip within a 10 nm distance from the surface. The sample is placed on a piezo electric stage with the tip oscillating at its resonant frequency above it. Then in order to bring the tip into feedback, the piezo electric stage is slowly raised until the tip oscillation is dampened from the interaction with the surface. Once in feedback the sample is raster scanned and an image collected in far field optics in a pixel by pixel approach. By using this method, correlated topography and fluorescence images can be taken simultaneously.

The current NSOM used in the Vanden Bout research group is shown in figure 2. The illumination source is Tsunami Ti-Sapphire laser that is coupled into a frequency doubling crystal. The emitting light after the frequency doubling crystal can range from 390-440 nm depending on where the Ti-Saph laser is tuned.   The laser light is then passed through a short pass filter to remove any infrared light and then coupled into a fiber optic coupler that is coupled into the NSOM tip. When in feedback, the NSOM tip excites the sample and the fluorescence from the sample is collected through a high numerical aperture objective.   The fluorescence then is focused through a lens and

filtered through a long pass filter of appropriate wavelength to remove any laser excitation light. The fluorescence is then collected onto an avalanche photo diode (APD). If polarized fluorescence images are desired then the fluorescence can be split using a cubic beamsplitter and collected the polarized fluorescence on two APDs.
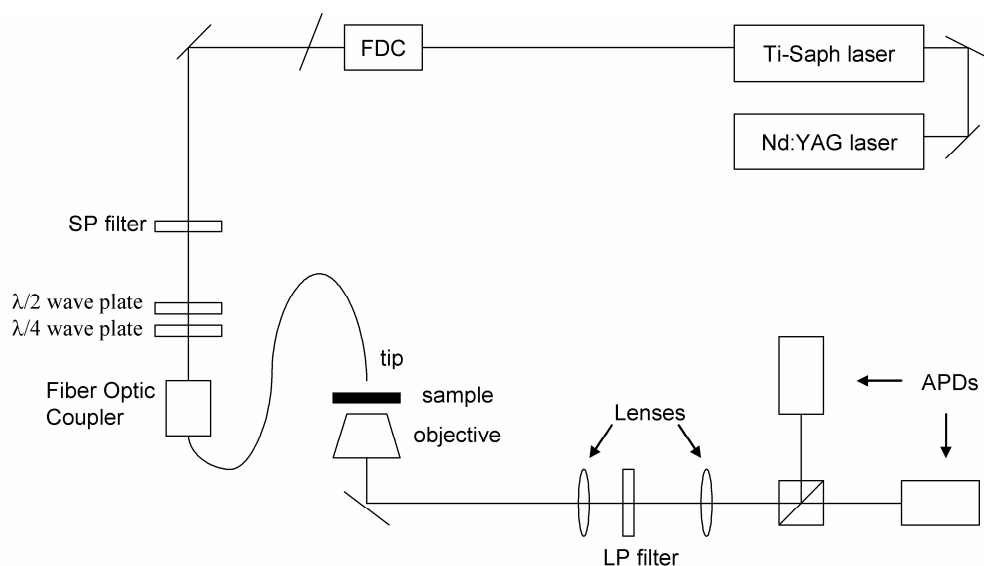
Figure 3.2   Current NSOM setup used. Abbreviations: FDC, frequency doubling crystal; SP, short pass; LP, long pass; APD, avalanche photodiode.

Atomic Force Microscopy

Atomic Force Microscopy (AFM) images were taken on a Nanoscope II (Digital Instruments/Veeco) multimode scanning probe microscope in tapping mode. Underwater AFM images were collected using the Digital Instruments/Veeco underwater tip holder with a contact mode tip in tapping mode. The procedure for underwater imaging is as follows: the AFM sample is placed in the AFM and the microscope was adjusted so that the surface was in focus (once the surface was found the microscope was not moved again because it was impossible to find the sample surface once water has been placed on the surface), then a drop of deionized water was pipetted onto the sample, next DI water

was injected into one of the tip holder's side holes, until the tip was completely immersed in water, after that, the tip holder was carefully placed into the AFM, so that a column of water between the tip and the sample was formed, and finally the tip was then brought in close to the surface manually.

AFM Technique

Atomic Force Microscopy (AFM) is a scanning probe technique used to examine the surface topography of films. The AFM works by raster scanning the sample under a sharp tip on a cantilever. As the tip is tracked across the surface, a laser beam is shone down onto the tip where it is reflected onto a photodiode. And as the tip is attracted and repelled by the surface, the magnitude of deflection is then plotted versus tip position. There are three main ways the tip can interact with the surface, in contact mode, non-contact mode, and tapping mode. Specifically, in this research tapping mode was utilized because it is a more gentle technique than contact mode and will not damage the sample. In tapping mode the tip is oscillated at a resonance frequency above the surface and it only taps the surface for a very small fraction of the time.

Fluorescence Microscopy

Fluorescence microscopy images were obtained on an Olympus BX60 microscope with a Diagnostic Instruments SPOT camera. Images were collected using a 100X oil immersion objective. Samples were made by placing an 8 μL aliquot of a fibril solution containing ThT onto a microscope slide which was then covered with a coverslip. The sample was then illuminated with a mercury lamp through a filter cube.

RESULTS AND DISCUSSION

Spectroscopy

Congo Red

      Absorption and fluorescence spectroscopy was used to study the binding of CR to amyloid fibrils. Two solutions containing the same concentration of CR were made, with one in water only and one containing fibrils. The absorption spectrum of a CR solution in water had two peaks, one at 350 nm and the larger second peak had a maximum absorption of ~500 nm. When the CR solution was excited at 500 nm, the emission spectrum had no vibrational structure and a wavelength maximum at ~620 nm. When fibrils were introduced into the solution, the absorption spectrum still had two absorption peaks. The first absorption peak at 350 nm decreased slightly, while the second absorption peak red-shifted to ~530 nm. When the CR/fibril solution was excited at 500 nm, there was enhanced fluorescence and the emission spectrum slightly blue-shifted to ~610 nm. Figure 3.3 shows the normalized absorption and emission spectra for both CR alone in solution and bound to amyloid fibrils. When CR was alone in water, it had a very low quantum efficiency and will only have detectable fluorescence when the fluorometer slit widths are opened to ~2 mm (or ~8 nm). The low quantum efficiency is due to the CR structure being a floppy molecule, and which decays mostly through non-radiative channels. When CR in solution was excited, the photon relaxes to a lower vibrational state before emitting as non-radiative decay. Then when CR was bound to the fibrils, it caused the CR structure to become more rigid, which slightly blue-shifted the emission and caused an increase in the quantum efficiency, seen by the increase in the fluorescence signal. However, the fluorescence signal increases by a little less than an order of magnitude, which suggests that most of the decay is still dominated by non-

radiative decay. The low quantum efficiency of CR even when bound to fibrils does not make it a good candidate for NSOM studies where a more fluorescent dye is needed.
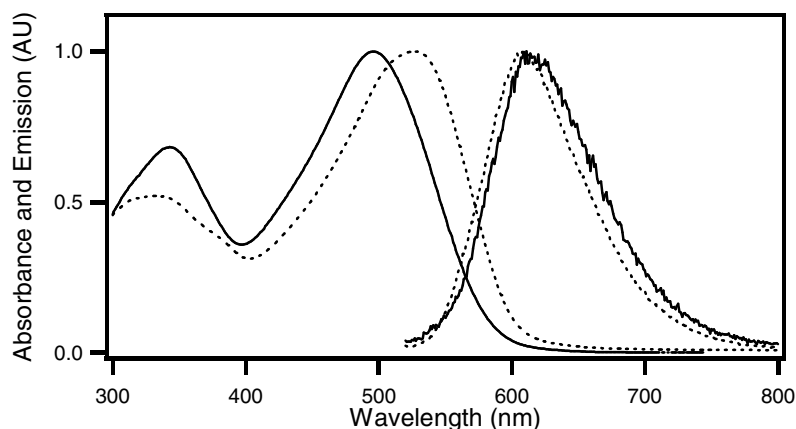
Figure 3.3   Normalized absorption and emission spectra for CR in water (solid lines) and bound to fibrils (dotted lines).

Anisotropy measurements were taken of CR free in solution and when CR was bound to the fibrils. Figure 3.4A shows the anisotropy plotted with the emission spectrum of CR free in solution. CR free in solution has an average anisotropy of ~0.33; this is unusual for a small molecule dye in solution, which should have a anisotropy of zero. However, CR is known to form micelles above a 6 μM concentration, the solution used for the anisotropy measurements had a CR concentration of ~29 μM; well above the critical micelle concentration. Therefore the reason for the high anisotropy is probably due to the presence of slow rotating micelles in the solution. To prove that it was indeed micelles causing the anisotropy to be 0.33, a CR solution below the micelle concentration could be used to calculate the anisotropy; however, since the CR in solution has a low quantum efficiency, a concentration less than 6 μM would be almost impossible to detect enough fluorescence to calculate the anisotropy accurately. Figure 4B shows the

anisotropy plotted with the emission spectrum of CR bound to fibrils. When CR was bound to fibrils the average anisotropy was calculated to be ~0.36, which is reasonable because CR is now bound to a fibril which is a large slow rotating aggregate that confines CR and will not allow it to rotate freely in solution.
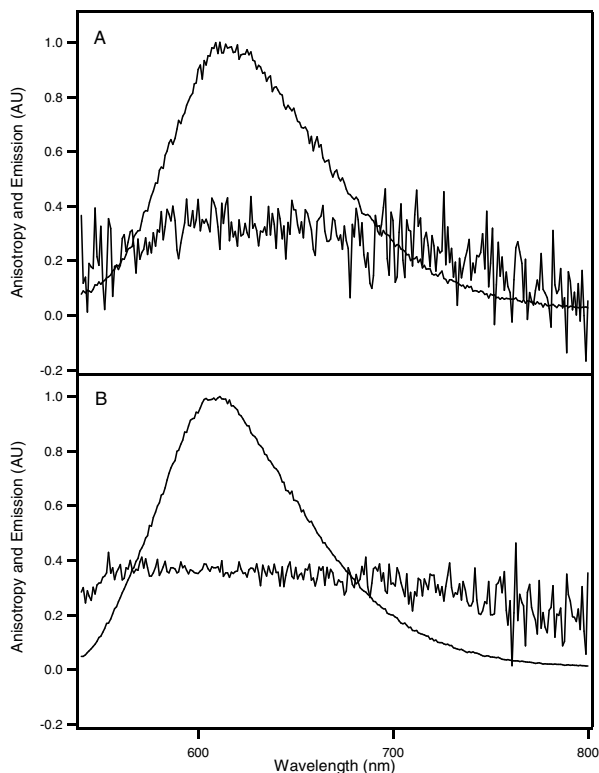
Figure 3.4   The anisotropy and emission of A) CR in water (r= 0.33) and B) CR bound to amyloid fibrils (r= 0.36).

Thioflavin T

Absorption and fluorescence spectroscopy were used to study the spectral changes of ThT when it binds to amyloid fibrils. ThT alone in water has an absorption maximum at 412 nm and an emission maximum at ~480 nm. The quantum efficiency of ThT in water is low, meaning it absorbs well, but loses most of its energy non-radiatively. This

is most likely from internal rotation around the single between the dimethylaniline group and the benzothiazole group. Then upon binding to amyloid fibrils, the excitation maximum has a bathochromic shift to 460 nm. Figure 3.5A shows the absorption, excitation and emission spectra for ThT free in solution and bound to amyloid fibrils. In the emission spectrum no significant shift was observed; however, the fluorescence intensity increased significantly (~106 fold increase in fluorescence). The increase in fluorescence intensity is due to the confinement of the ThT molecule within the fibrils, then when the ThT is excited it can no longer rotate around the single bond as it can in solution; thus, effectively keeping the molecule planar and increasing the ThT's quantum efficiency. This increase in the quantum efficiency of ThT can also be mimicked by dissolving ThT in a viscous medium such as glycerin. When ThT is dissolved in glycerin, it has an absorption maximum at 424 nm and an emission maximum at 495 nm, and the emission intensity is also increased (Figure 3.5B). The red-shift in of the absorption peak is indicative of the red-shift observed when ThT binds to amyloid fibrils, although it does not shift to the same wavelength because glycerin is not able to constrain ThT as well as the fibril structure. Then in the emission spectrum, the reason the ThT's intensity increases is because glycerin is so viscous, it does not allow ThT to release energy as non-radiative, and thus increases its fluorescence quantum yield. ThT has been extensively researched and these results fall in line with what other researchers have observed.[21-24, 27]
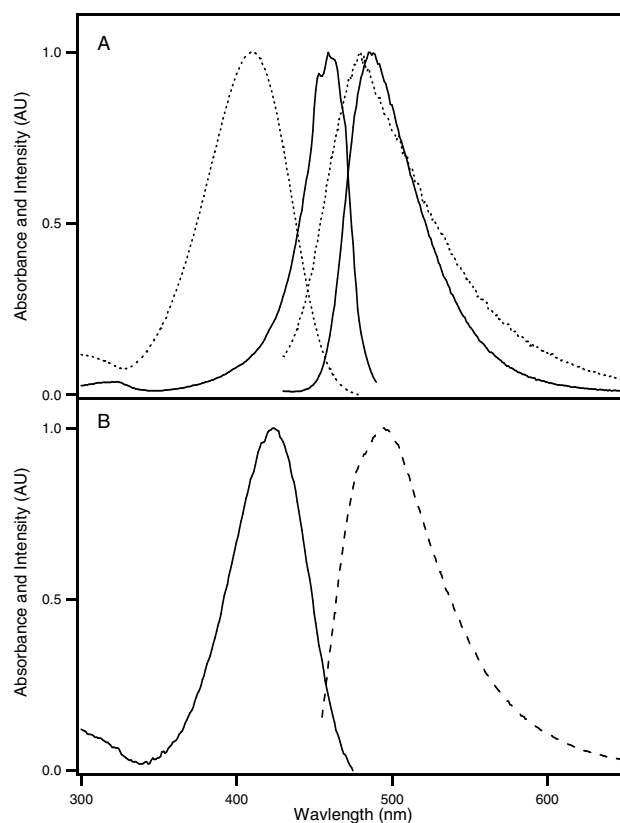
Figure 3.5   Absorption, excitation and emission of ThT in water, glycerin, and bound to
               fibrils.   A) Absorption and emission of ThT in water (dotted lines),
               Excitation and emission of ThT bound to amyloid fibrils (solid lines). B)
               Absorption of ThT in glycerin (solid line) and emission of ThT in glycerin
               (dashed line).

Time correlated single photon counting lifetimes were collected of ThT in glycerin and ThT bound to fibrils. Both samples were excited with 440 nm light and the fluorescence counts were collected at 500 nm. The lifetimes were collected through a polarizer set at the magic angle (54.7°). When ThT was in glycerin, the lifetime fit to a two exponential decay comprised of fast and a slow lifetime. The slow component had a lifetime of 526.4 ps (A_1= 9411 counts) and the fast component had a lifetime of 172.9 ps (A_2= 9890 counts) (figure 3.6b). The lifetime of the ThT bound to fibrils also fit a two

71

exponential decay, but had a longer lifetime than when ThT was in glycerin. The slow

component of the ThT bound to fibrils had a lifetime of 1.73 ns (A_1= 6544 counts) and

the fast component had a lifetime of 515.0 ps (A_2= 4180 counts) (Figure 3.6a). The

reason ThT has a faster lifetime in glycerin is because ThT still decays mostly through

non-radiative decay. Even though glycerin decreases the rotation around ThT's single

bond, it does not increase the quantum efficiency as much as when ThT is confined in the

fibrils. Therefore, ThT in glycerin still has a large non-radiative component giving it a

faster lifetime, whereas ThT's restricted rotation leads to higher quantum yield and a

longer lifetime decay.
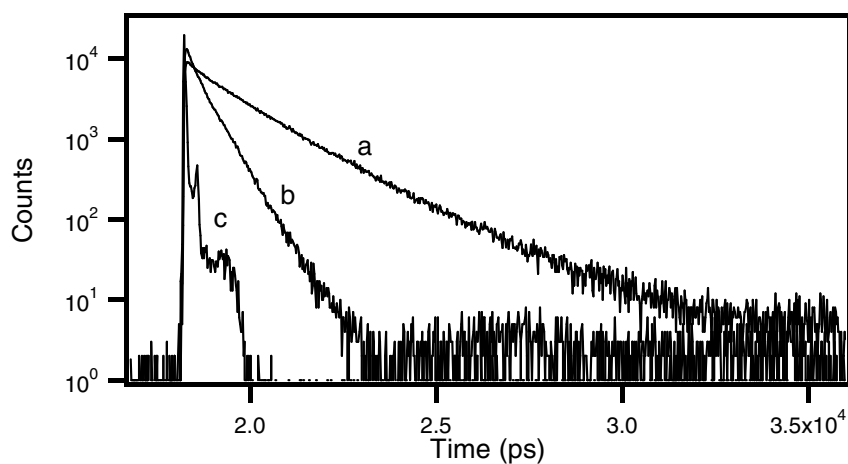
Figure 3.6   Lifetime decays of ThT in glycerin and bound to fibrils excited at 440 nm.
a) The lifetime of ThT bound to fibrils, b) the lifetime of ThT in glycerin, c)
the IRF.

Anisotropy measurements were also collected to study the effects of binding. ThT is a small molecule and when free in solution should have an anisotropy of zero; however, if the molecule is known to form micelles at high concentrations then the observed anisotropy can be greater than zero. This is the case with ThT, when it is dissolved in water the average anisotropy is 0.32, which indicates that micelles are in fact present in the solution. The anisotropy for a molecule is zero when the molecule rotates faster than the fluorescence lifetime and the anisotropy can be increased by slowing down the rotation of the molecule by either fixing it in film or using a more viscous solvent. Therefore, when ThT is dissolved in glycerin the anisotropy increases to ~0.3, indicating that the molecular rotation has indeed been slowed and that the dye no longer rotates faster than it emits. Finally, when ThT is bound to amyloid fibrils the average anisotropy was calculated to be ~0.38, and this indicates that the ThT dye is fixed in the amyloid fibrils and cannot rotate at all. Figure 3.7 shows the emission and anisotropy spectra for ThT in the three different mediums. The difference in anisotropy values between ThT free in solution and with amyloid fibrils confirm the fact that ThT is indeed binding to the fibrils.
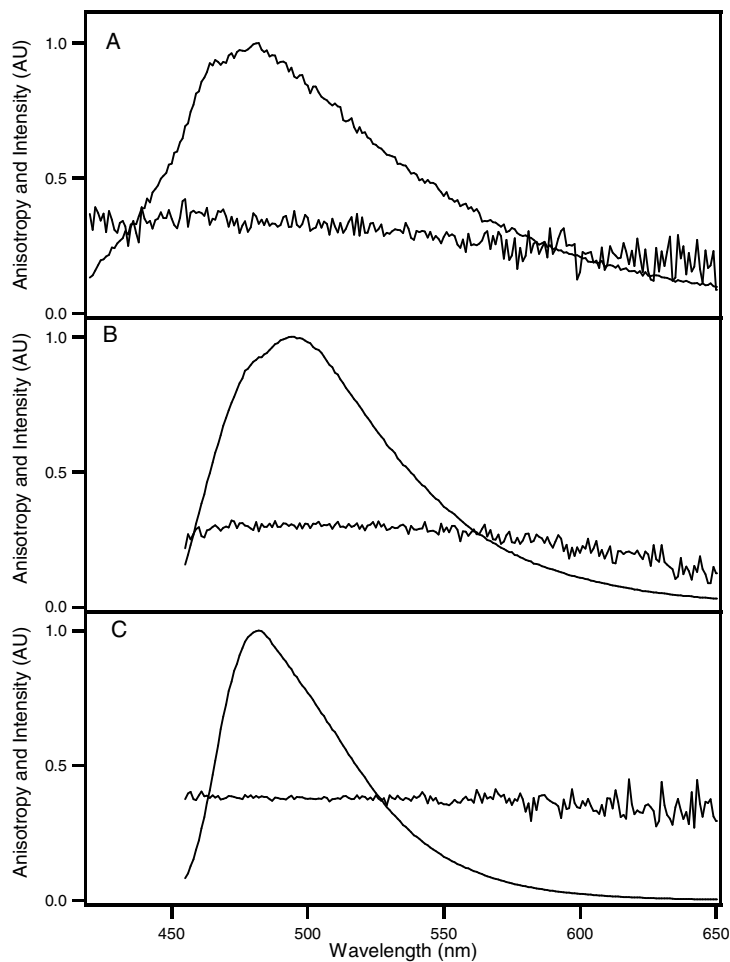
Figure 3.7   Anisotropies and emission spectra of ThT in water, glycerin and bound to fibrils.   A) ThT in water (r= 0.32), B) ThT in glycerin (r= 0.3), C) ThT bound to fibrils (r= 0.38).

Since the ThT does bind to amyloid fibrils, it was important to determine if there was a concentration dependence for ThT to bind to amyloid fibrils.   Therefore, an experiment was done where several solutions containing the same amount of fibrils were made, but each one had a different concentration of ThT ranging from 0.3 μM to 125 μM. An emission spectrum was taken of each sample by exciting at 440 nm.   Then the

fluorescence intensity at 484 nm was plotted versus the ThT concentration (Figure 3.8). The graph shows that as the concentration of ThT is increased the fluorescence's intensity increases linearly below the micelle concentration. Then above the micelle concentration the intensity slightly plateaus before reaching a peak in the fluorescence. Then upon increasing the ThT concentration further the intensity starts decreasing. The fibrils in the solution have a set amount of binding sites available for ThT to bind and therefore at really low concentrations there are more binding sites available then ThT molecules. So as more and more ThT molecules are added the fluorescence intensity will keep increasing until all the binding sites are saturated, and the fluorescence maximum will be reached. Then if more ThT dye is added after all the binding sites are occupied then the decrease in fluorescence intensity is possibly due to the self-quenching of the excess dye. The binding of ThT as a function of pH was also studied and those results are discussed in the ITC chapter.
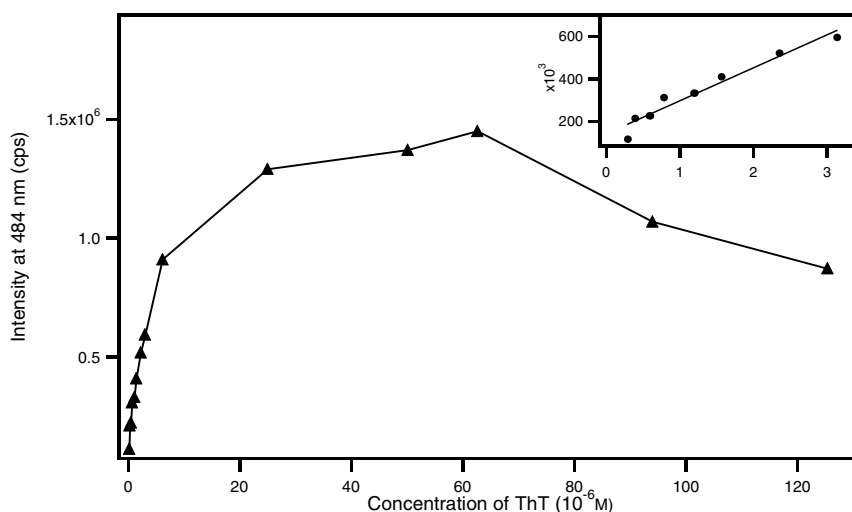
Figure 3.8   Graph of the intensity of ThT when bound (484 nm) versus the total ThT concentration added. The inset is plot of ThT concentration below the micelle concentration [$y = (1.5582*10^5 \text{ cps}/\mu M) x + 1.3903*10^5 \text{ cps}$].

BTA-2

BTA-2 was studied using absorption and fluorescence spectroscopy. BTA-2 is a structurally similar dye to ThT; however, it lacks the methyl group on the benzothiazole's nitrogen that makes ThT a charged molecule. When the positive charge is removed, the molecule goes from being soluble in water to being insoluble. This is a problem because the fibrils are in an aqueous solution. Previous researchers who have used BTA-2 were able to circumvent this problem by first making a stock BTA-2 solution in DMSO and then dissolving an aliquot of this solution in water or a buffered solution, since DMSO is miscible in water.[28, 30, 31] However, our ultimate goal was to use the BTA-2/fibrils solutions to make NSOM samples on poly(lysine) coated coverslips. Poly(lysine) is a positively charged molecule that enables the fibrils to adhere to the surface; however, DMSO has a formal negative charge and is extremely good at solvating positive charges. Consequently, it may compete with the amyloid fibrils for adhesion to the poly(lysine) surface or dissolve the poly(lysine) off the coverslips. This would then prevent the fibrils from adhering to the coverslip. Therefore, an alternative solvent, acetonitrile (CH_3CN), was used in order to avoid the potential problems associated with DMSO. Acetonitrile is miscible in water and does not contain a charged group that would compete with the fibrils for binding on the surface. BTA-2 was found to dissolve well in acetonitrile, which would enable BTA-2 to be dissolved in aqueous solutions.

Unfortunately, BTA-2 is a relatively new dye and little is known about sample preparation with fibrils in solution. Therefore, a series of three samples were made in order to determine the optimal sample preparation alone and with fibrils. The samples all contained the same amount of fibrils and BTA-2 dye concentrations, the only varying factor was the dilution solvent. The first sample was diluted with pH 2 water, which gave the solution a pale yellow color and had an approximate pH of 2. The second solution

was diluted with nanopure water and it became a cloudy yellow color, with an approximate pH of 5. The third solution was diluted with a 1:1 mixture of water and acetonitrile, and it had a rich yellow color, with an approximate pH of about 5. The pH of the solution is important because the pK_a of the nitrogen on the dimethyl aniline group has been reported to be ~2 (as reported by Klunk *et al.*[28]), and if the nitrogen is protonated this would potentially increase the solubility of BTA-2 in water. The cloudy yellow color associated with the BTA-2/fibril sample that was diluted with water is possibly due to the BTA-2 starting to crash out of solution, since at pH 5 the dimethyl aniline nitrogen would start to deprotonate. The reason the third BTA-2/fibril sample did not show any precipitate at pH 5 is because there was enough acetonitrile to keep the BTA-2 fully solvated. Since these solutions contained fibrils, it was important to have BTA-2 solutions made the same way without fibrils present in order to confirm binding had occurred and to look at the spectroscopy of BTA-2 free in solution. Also a solution containing ThT bound to fibrils and solution with ThT alone acted as controls for comparison, and to ensure binding to the fibrils was observed. It was decided that spectroscopy would not done on the samples containing BTA-2 samples diluted with water, since it was determined the BTA-2 had crashed out of solution.

Absorption, excitation, and emission spectra were taken of BTA-2 alone in pH 2 water. The absorption spectrum of the BTA-2 alone in pH 2 water had a single absorption peak with a maximum at ~430 nm. An emission spectrum was then taken by exciting at 420 nm (a 420 nm band pass filter was used, due to lack of a 430 nm band pass filter) and the emission spectrum had a single peak at ~475 nm. Next an excitation spectrum was taken collecting the emission at 475 nm. The excitation spectrum had a peak at 365 nm, which is significantly blue-shifted, 65 nm, from the absorption spectrum's peak. Since the excitation spectrum had a different peak from the absorption

spectrum, another emission spectrum was taken, this time exciting at 365 nm. When the sample was excited at 365 nm, the emission peak blue-shifted to ~440 nm and a 3.5 fold increase in the intensity was observed (Figure 3.9A). Figure 3.9B shows all the normalized spectra for BTA-2 in pH 2 water. The dramatic differences in the absorption and excitation spectra were unusual, but the shift in the emission spectra upon exciting at different wavelengths, suggested that another species of BTA-2 was present in the solution. To ensure that the spectral shifts were not due to impurities from the starting materials, absorption, emission, and excitation spectra were taken of benzothiazole and N,N-dimethylaniline. The starting materials spectra were out in the UV region and did not overlap with any of the BTA-2 spectra in solution. Therefore, the spectral shifts in the BTA-2 solutions were not due to impurities and must be caused by another species being present. ThT has been known to form micelles in solution and since BTA-2 has a similar structure; it is entirely possible that BTA-2 is forming micelles.
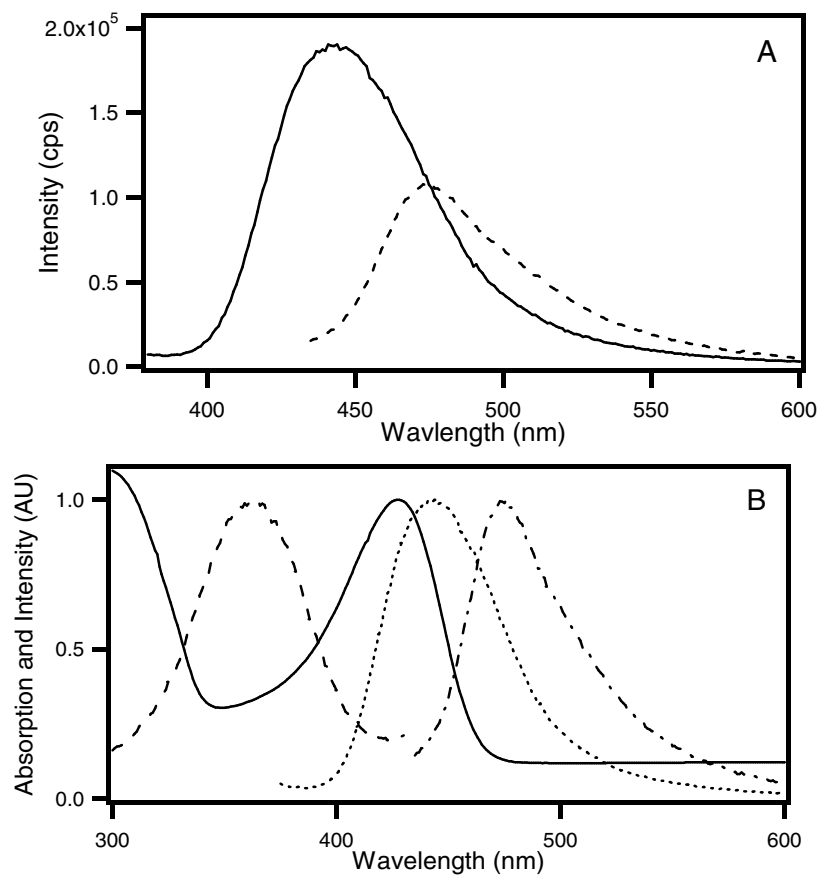
Figure 3.9   A) Emission spectra of BTA-2 in pH 2 water excited at 420 nm (dashed line) and excited at 365 nm (solid line). B)Absorption (solid line), excitation (dashed line), and emission spectra of BTA-2 alone in pH 2 water. The dotted-dashed line is the emission spectrum when excited at 420 nm and the dotted line is the emission spectrum when excited at 365 nm.

79

Anisotropy measurements would give some insight if micelles were indeed forming. If micelles were present, then the anisotropy should be greater than zero because the micelles are a slower rotating species than a free BTA-2 molecules. If a zero anisotropy was obtained, this would indicate a small freely rotating molecule, that rotates faster than it emits. The anisotropy was calculated for BTA-2 in pH 2 water first by exciting at 420 nm, near the peak of the absorption spectrum, and was found to have an average anisotropy of ~0.28 (Figure 3.10A). However, when the sample was excited at 365 nm, the peak of the excitation spectrum, the average anisotropy was calculated to be ~0.06 (Figure 3.10B). The anisotropy measurements indicate that there is indeed two different species present in the solution. The slower rotating species of BTA-2, which an absorption at 430 nm and an emission at 475 nm, is mostly like micelles. While the faster rotating species, which has an excitation maximum at 365 nm and emits at 440 nm, would be from the free BTA-2 molecules. Although, micelles are generally observed by an additional small red-shifted peak in the absorption spectrum along with the free dye absorption peak; the BTA-2 in pH 2 water only has a single absorption peak.
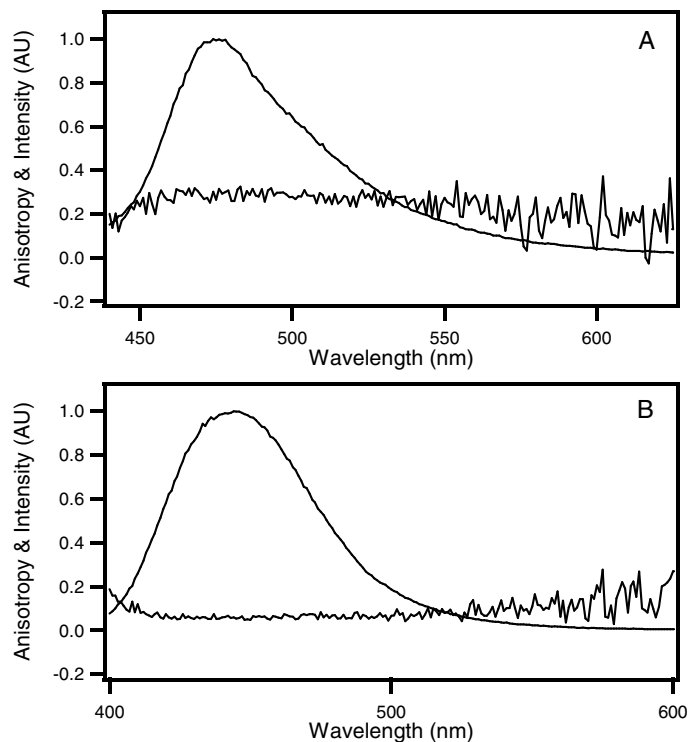
Figure 3.10 Anisotropy and emission spectra of BTA-2 in pH 2 water. A) Shows the anisotropy when the solution is excited at 420 nm (r= 0.28). B) The anisotropy when the solution is excited at 365 nm (r= 0.06).

The BTA-2 solution in a 1:1 mixture of water and CH_3CN gave further insight into determining if micelles were indeed forming. An absorption, emission, and emission spectra were taken of the BTA-2 alone in a solution diluted with a 1:1 mixture of CH_3CN and water. The absorption spectrum of the BTA-2 alone in solution was so concentrated that the absorption was maxed out at 3; however, there was a detectable peak at 430 nm, similar to the absorption peak observed when BTA-2 was in pH 2 water. This large absorption was odd, since the solution contained the same BTA-2 concentration as the BTA-2 solution in pH 2 water, and that solution had an absorption OD of 0.7 at 430 nm. The sample was not diluted to decrease the absorption because all the samples were made with the same and we wanted to be able to directly compare the samples. The BTA-2

solution was then excited at 420 nm, and the emission spectrum had a maximum peak at ~470 nm. The excitation spectrum was then taken collecting at 470 nm and a sharp peak at ~400 nm was observed. The excitation spectrum was blue-shifted from the 430 nm absorption peak, which was similar to what was observed when BTA-2 was in pH 2 water. Thus, another emission spectrum was taken this time exciting at the excitation peak, 400 nm. The emission spectrum of the BTA-2 solution excited at 400 nm, had a maximum peak at ~460 nm and was an order of magnitude more intense than the emission spectrum at 470 nm (Figure 3.11B inset). Figure 3.11B shows the normalized spectra for BTA-2 alone in 1:1 mixture of CH_3CN and water. Since the sample containing BTA-2 in 1:1 mixture of CH_3CN and water maxed out in the absorption spectrum, it was diluted in order to lower the OD. Upon diluting the sample, the peak at 430 nm disappeared; leaving a single peak at 360 nm (Figure 3.11A). The disappearance of the red-shifted peak at 430 nm suggests that there are in fact micelles present in the solution. It is known that small molecule dye aggregates are known to have red-shifted absorption peaks and upon dilution can be dispersed, leading to the disappearance of the red-shifted peak. Anisotropy measurements were performed in order to confirm if micelles were present in the solution. Anisotropy measurements were first taken of the BTA-2 in 1:1 mixture of water and CH_3CN by exciting at 420 nm. The average anisotropy was calculated to be ~0.22, indicating that there is slowly rotating species present. Next, anisotropy measurements were taken of the solution by exciting at 400 nm and the average anisotropy was found to be ~0.017 (Figure 3.11C). The absorption spectra and the anisotropy measurements confirm that micelles are indeed present in solution.
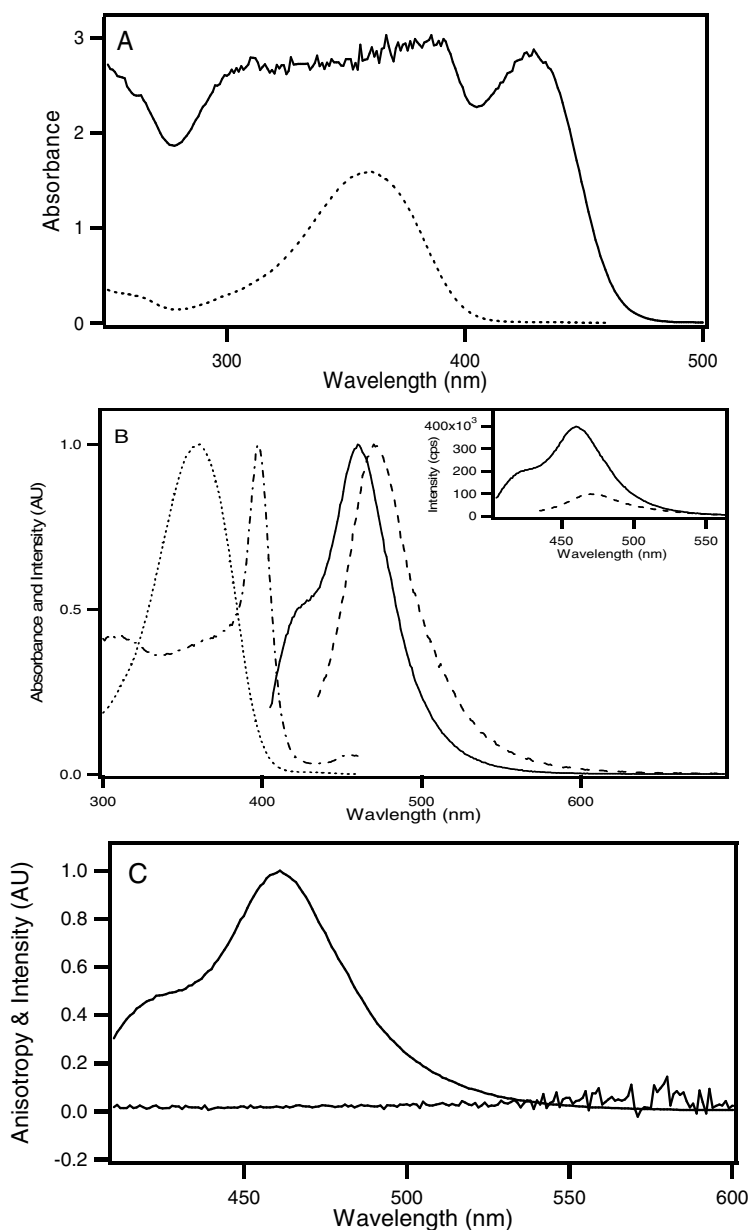
Figure 3.11 BTA-2 alone in a 1:1 mixture of CH_3CN and water. A) Absorption spectra: concentrated (solid line) and diluted (dotted line). B) Diluted absorption spectrum (dotted line), excitation spectrum (dashed-dotted line), emission spectrum excited at 420 nm (dashed line), and the emission spectrum excited at 400 nm (solid line). The inset shows the emission spectra when excited at 420 nm (dashed line) and excited at 400 nm (solid line). C) Anisotropy excited at 400 nm (r =0.017)

Micelle formation occurred in both BTA-2 solutions and was the cause of the spectral shifts observed in the solutions. The 430 nm peak in the absorption spectrum was due to the micelles; however, the excitation spectrum was from the free BTA-2 molecules in solution. A possible reason no peak at 430 nm was observed in the excitation scan was due to the micelles self quenching or because the free BTA-2 is so much more fluorescent that it overwhelms any micelle fluorescence. Then upon exciting at the excitation maximum, we are now exciting only the free BTA-2 molecules in solution and this would account for the blue-shift emission spectrum, relative to the emission spectrum when the micelles were excited. Comparing the two BTA-2 solutions used, similar spectral behavior was observed; however, the absorption spectrum of BTA-2 in pH 2 water had no additional absorption peak, only the 430 nm peak. This suggests that in pH 2 water, the majority of the BTA-2 molecules exist as micelles and what little free BTA-2 exists in solution does not absorb enough to be detected. Then if the sample was excited at the excitation peak, no fluorescence was observed from the micelle peak (λ_{max} = 475 nm) because the fluorescence intensity of the small amount of free BTA-2 was so intense that it drowned out any fluorescence from the micelles. The anisotropy measurements confirmed a slow rotating species present, which is consistent with micelles. In the 1:1 mixture of water and CH_3CN, the BTA-2 is mostly in its free state; however, micelle formation did occur at high concentrations. In pure CH_3CN, BTA-2 did form micelles even at high concentrations and had an anisotropy of 0.004 (Figure 3.12). This indicates that as more CH_3CN is added to the solution, the CH_3CN prevents micelle formation, which is why only a peak 360 nm is present. The decrease in micelle formation between samples was also observed in the anisotropy measurements. There was a decrease in the anisotropy at the micelle emission when more CH_3CN was present in solution, going from an anisotropy of 0.28 in pH 2 water to 0.22 in a 1:1 mixture of

water and CH₃CN. Therefore, this suggests that water promotes the formation of BTA-2 micelles, while CH$_3$CN favors the free monomeric BTA-2.
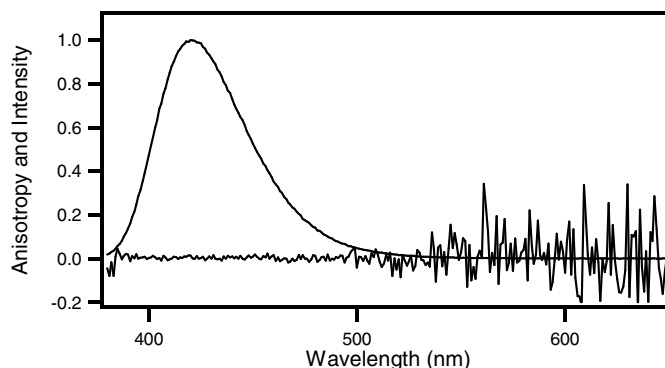
Figure 3.12 The anisotropy and emission spectrum of BTA-2 in CH$_3$CN (r= 0.004).

Now that micelle formation had been confirmed, the BTA-2 binding to fibrils was studied. An absorption spectrum was taken of BTA-2 bound to fibrils in pH 2 water. In the absorption spectrum, two peaks were observed, one at 385 nm and another peak at 430 nm, which is from the absorption of the micelles. An emission spectrum was first taken by exciting at 420 nm and had a maximum at ~475 nm, which is the same λ_{max} observed when BTA-2 alone in pH 2 water, indicating that there are still micelles present in the solution. An excitation spectrum was taken and the excitation maximum was at 380 nm. This maximum was at the same wavelength as the first peak in the absorption spectrum, which indicates that the first absorption peak is the absorption from the bound BTA-2. When the sample was then excited at the peak of the excitation spectrum, the emission spectrum had a maximum peak at 425 nm. The excitation spectrum and the emission spectrum (excited at 385 nm) corresponds to BTA-2 bound to fibrils. Figure 3.13A is the normalized spectra for BTA-2 bound to fibrils in pH 2 water. Anisotropy measurements were also taken by exciting the sample at 385 nm in order to confirm binding. The average anisotropy was calculated to be ~0.33 (Figure 3.13B). This

85

indicates that BTA-2 did indeed bind to the fibrils because an anisotropy of ~0.33 corresponds to what is expected for a confined small molecule unable to rotate.
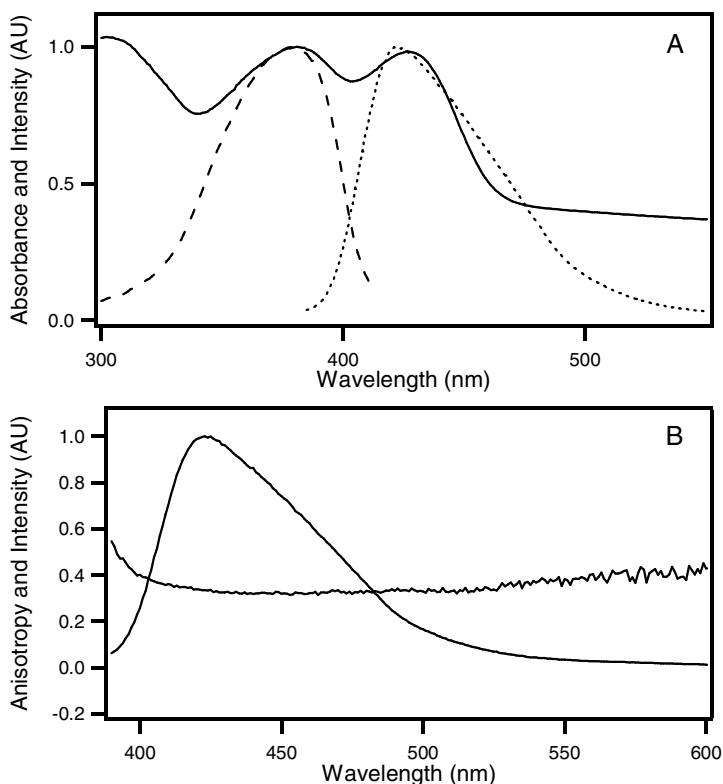
Figure 3.13 BTA-2 bound to fibrils in pH 2 water. A) Absorption (solid line), excitation (dashed line), and emission (dotted line) spectra. B) Anisotropy excited at 385 nm (r= 0.33).

Although BTA-2 forms micelles, it was still able to bind to the fibrils in pH 2 water. Figure 3.14 is the normalized excitation and emission spectra of BTA-2 free and bound to fibrils in pH 2 water. When BTA-2 is alone in solution the excitation maximum is at 365 nm and the emission maximum is at 440 nm, then upon binding to the fibrils the excitation maximum red-shifts to 380 nm and the emission maximum blue-shifts to 425 nm, and the emission intensity also increased by a factor of 6. This trend is similar to what was observed when ThT binds to amyloid fibrils. When BTA-2 binds to fibrils, the

86

emission blue-shifts and the quantum efficiency of the dye increased due to its confinement in the fibrils. Whereas in the excitation spectrum a red shift was observed because when BTA-2 is bound to the fibrils, the BTA-2 molecule has a slightly planar conformation and requires less energy to be excited. In comparing the quantum efficiency of BTA-2 to ThT when alone in solution, BTA-2 seems to have a higher quantum efficiency than ThT.
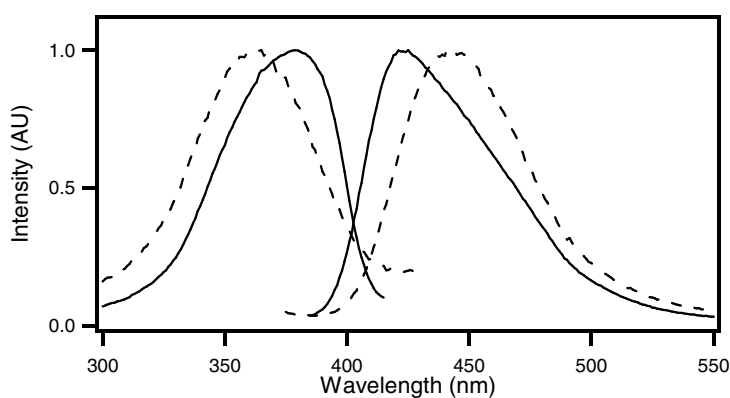
Figure 3.14 Excitation and emission spectra of BTA-2 alone (dotted lines) and bound to fibrils (solid lines) in pH 2 water.

Absorption, emission, and emission spectra were taken of the BTA-2 bound to fibrils in the solution diluted with a 1:1 mixture of CH_3CN and water. The absorption spectrum taken of the BTA-2 solution bound to fibrils was again maxed out with an OD of 3, but also had the micelle peak at 430 nm. Upon dilution of the solution, the 430 nm peak disappeared and the absorption spectrum had a single peak at 360 nm. An emission spectrum was then collected by exciting at 420 nm to see if only the micelles would emit. The peak of the emission spectrum was ~467 nm, which at the same wavelength the micelles emitted at in the solution containing only BTA-2. The excitation spectrum was taken and the spectrum showed a sharp peak at 400 nm, similar to what was observed when BTA-2 free in solution. When an emission spectrum was taken by exciting at 400

nm, the fluorescence peak was at 460 nm, again the same as that of the BTA-2 free in solution; however, the intensity increased by a factor of ~1.4 when BTA-2 was bound to the fibrils. Figure 3.15 shows all of the normalized spectra for BTA-2 bound to fibrils in a 1:1 mixture of CH_3CN and water.
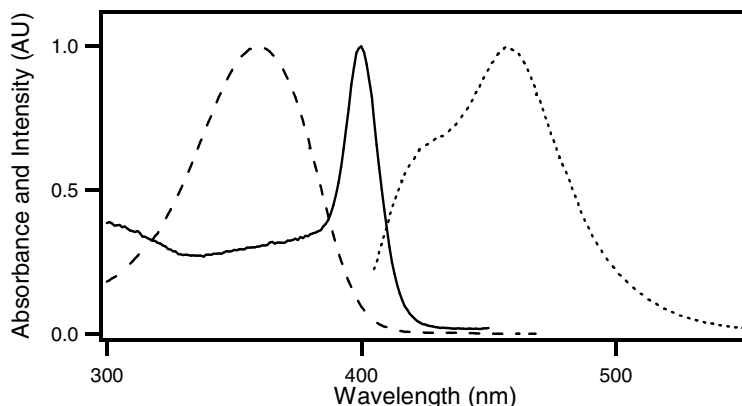
Figure 3.15   The absorption, excitation, and emission spectra of BTA-2 bound to fibrils in 1:1 mixture of CH_3CN and water.   BTA-2 bound to fibrils: absorption spectrum of the diluted solution (dashed line), excitation spectrum (solid line), and emission spectrum excited at 400 nm (dotted line).

In the BTA-2 samples that were diluted with CH_3CN and water, no spectral shifts were observed in the excitation or the emission spectra (Figure 3.16A), although the emission spectrum increased by a factor of ~1.4 when bound to fibrils. Binding was thought to occur until the anisotropy was calculated for the BTA-2/fibrils solution and found to have an average anisotropy of ~0.04 (Figure 3.16B). If the BTA-2 had bound to the fibrils then there would have been an increase in the anisotropy as seen in ThT binding and in BTA-2 binding at pH 2. Subsequently, if the BTA-2 did not bind to the fibrils, this would explain the lack of spectral shifts and why a larger increase in the fluorescence was not observed. One explanation for the lack of binding could be due to the mixed solvent medium. BTA-2 has been found to dissolve well in CH_3CN and will

not dissolve in water at all, whereas the fibrils are in an aqueous solution. Then when mixed with a 1:1 mixture of CH_3CN and water, a solvent sphere of CH_3CN forms around the BTA-2 molecules stabilizing them, whereas the water forms a solvent sphere around the fibrils; and thus in the solution the BTA-2 and fibrils are actually isolated from one another and binding cannot occur. From all this, it can be concluded that even though increasing the percentage of CH_3CN in the solution decreases the micelle formation, it consequently prevents the binding of BTA-2 to fibrils.
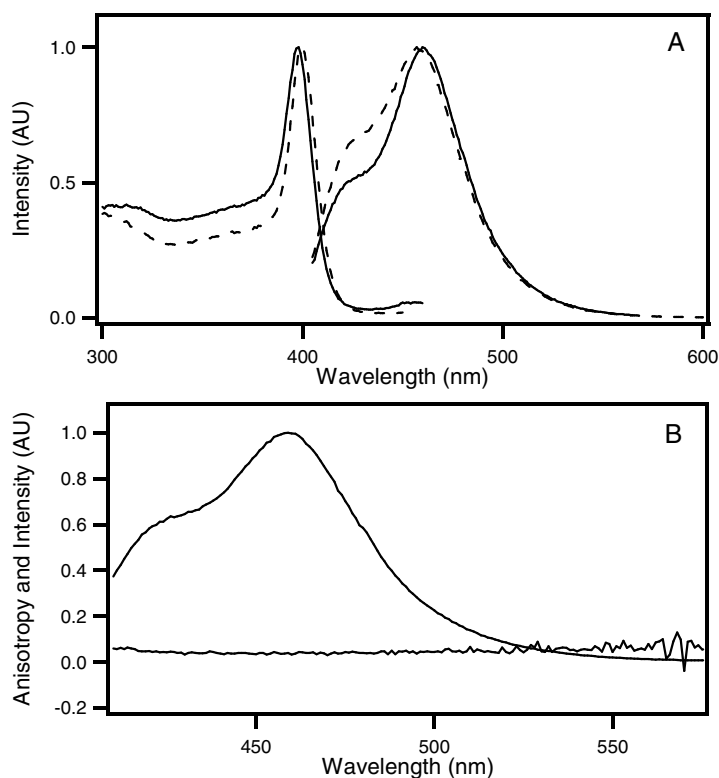
Figure 3.16 A) The normalized excitation and emission spectra for BTA-2 alone (solid lines) and bound to fibrils (dashed lines) in a 1:1 mixture of CH_3CN and water. The emission spectra were obtained by exciting at 400 nm. B) The anisotropy of BTA-2 bound to fibrils in a 1:1 mixture of CH_3CN and water excited at 400 nm (r= 0.04).

89

The fluorescence maximum varied between the two samples, so we wanted to determine if the emission shifts were possibly due to solvent effects. BTA-2 was dissolved in various solvents with a wide range of polarities, and the following solvents were used: cyclohexane, chloroform, ether, ethanol, acetone, and acetonitrile. Each BTA-2 solution was excited at 350 nm, which is the peak maximum of the excitation spectrum and the absorption spectrum. Figure 3.17 shows the normalized excitation and emission spectra for BTA-2 in CH_3CN, ether, and cyclohexane. In both the excitation and emission spectra, a red-shift is observed with increasing solvent polarity. The excitation spectra did not show a significant red-shift with increasing polarity; however, in the emission spectra a more significant spectral shift is observed. Since BTA-2 is itself a polar molecule, this suggests BTA-2 is stabilized by polar solvents. The more polar solvent molecules are able to orient themselves around the BTA-2 molecule in such a way that it lowers the energy required to excite it to the first excited state and subsequently the emission is a lower energy as well. However, when BTA-2 is dissolved in more nonpolar solvents, the solvent molecules do not stabilize the BTA-2 molecules as well, therefore increasing the amount of energy required to excite the BTA-2 molecule and a blue-shift is observed relative to the emission of BTA-2 in polar solvents. This would account for the emission differences of BTA-2 in pH 2 water and the 1:1 mixture of CH_3CN and water. The emission maximum of BTA-2 in pH 2 water was ~445 nm and the emission maximum in the 1:1 mixture was ~463 nm. Therefore, by increasing the amount of CH_3CN in the solution, the solvent becomes more polar and causes the BTA-2 emission to red-shift.
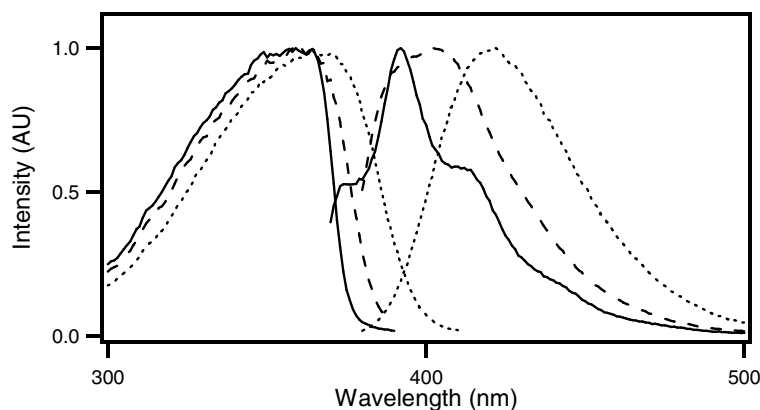
Figure 3.17 The excitation and emission spectra for BTA-2 in CH$_3$CN (dotted lines), ether (dashed lines), and cyclohexane (solid lines).

Ultimately, BTA-2 was going to be used as an alternative dye for NSOM samples and so it was important to determine if the BTA-2 bound to fibrils fluoresced in a film. Thus the two fibril samples containing BTA-2 were made into films by binding the fibrils to poly(lysine) coated coverslips and allowing them to dry. The fibril solutions contained high concentrations of fibrils, and therefore there were fibrils all over the surface. Fluorescence spectra could not be obtained using a standard fluorometer because the fluorescence of the coverslip drowned out any fluorescence the BTA-2 would emit. Therefore, the fluorescence spectra of the two films were obtained using a home-built sample scanning inverted microscope and collected in a spectrometer. The samples were placed in the microscope and excited at 405 nm using a diode laser. Figure 3.18 shows the emission spectra of both BTA-2/fibril samples and the background. The BTA-2/fibril film, made from the solution diluted with pH 2 water, was very intense and had an emission maximum at ~538 nm, which is significantly red-shifted from the emission maximum at 440 nm in solution. Since glass does fluoresce, background emission was taken and found to have an emission maximum at 486 nm, nowhere near the emission of

91

the film. Next an emission spectrum was taken of the BTA-2 fibril sample that was diluted with a 1:1 mixture of CH_3CN and water. The sample was not as intense as the other sample and it had an emission maximum at ~473 nm. Unfortunately, the background emission overlaps the emission of the film and would not be an ideal sample for NSOM. As a result, the best sample to use for NSOM studies is the BTA-2/fibril sample that was diluted in pH 2 water.
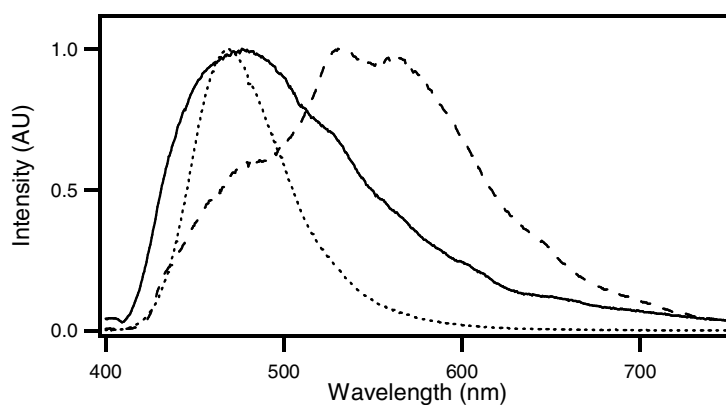
Figure 3.18 The emission spectra of BTA-2/fibril films made from the BTA-2/fibril solutions in pH 2 water or 1:1 mixture of CH_3CN and water. The emission spectrum for the film made from the BTA-2/fibril in the pH 2 water solution (dashed line). The emission spectrum for the film made from the BTA-2/fibril in the 1:1 mixture solution (dotted line). Background spectrum of a clean coverslip (solid line).

Microscopy

AFM

AFM was used to determine the length and width of the fibrils and to ensure that fibrils were present on the surface of the poly(Lysine) coated coverslips. AFM images were acquired of fibrils adhered to poly(lysine) coated coverslips. Figure 19A shows an AFM topography image of dried fibrils present on the surface. The image clearly shows that the length of the fibrils can be microns long, whereas, a line scan reveals the diameter of the fibrils to be between 5-15 nm (Figure 3.19B). The amount of fibrils present on the surface could also be changed by either increasing or decreasing the fibril solution concentration prior to making the films. Figure 3.19C shows an example of a more concentrated fibril film and a diluted fibril film. From the AFM images, it was determined that poly(lysine) was indeed a good adhesive for binding fibrils to a glass surface.
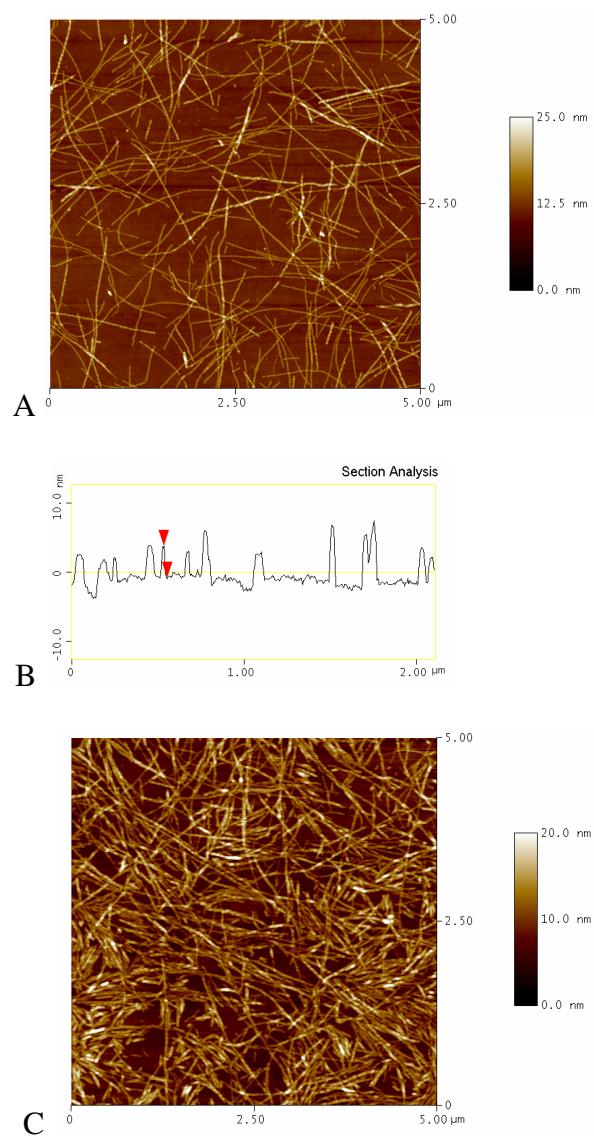
Figure 3.19 Two 5 μm AFM images of fibrils. A) A dilute fibril film. B) Line scan of
dilute fibril film. C) A concentrated fibril film.

At one point, poly(lysine) coated coverslips were binding fibrils sporadically and would not adhere the fibrils everywhere, and therefore a new means of adhering the fibrils to the surface of the glass coverslips was necessary. It was found that silanating the coverslips could provide an alternative method to using poly(lysine). By silanating the coverslips, the silanes form a covalent linkage with the hydroxyl groups sticking off of the surface of the glass. The surface is then functionalized with positively charged amine groups, similar to poly(lysine). Using the AFM, it was determined that the fibrils would in fact adhere to the silanated surface just as well as to a poly(lysine) coated coverslip; however, the silanating procedure is more arduous than coating with poly(lysine). It was discovered that the reason for the poor fibril adhesion to poly(lysine) coated coverslips was not due to the poor adhesive forces of the poly(lysine), but because prior to coating, the coverslips were not cleaned adequately, enough causing them not to be hydrophilic. Plasma etching was found to clean the coverslips extremely well and make the surface very hydrophilic, which then allowed for even coating of poly(lysine). From then on poly(lysine) coated coverslips were used since the procedure was easier and less time consuming.

Underwater AFM images were obtained in order to determine the actual size of the amyloid fibrils in their hydrated state. The images were acquired of fibrils adhered to a poly(lysine) coated coverslip and dried. For underwater imaging, a drop of nanopure water was placed on the dry sample surface in order to re-hydrate the fibrils. Figure 3.20 is a topography image of the amyloid fibrils underwater with a line scan. Upon doing a line scan it was determined that the average diameter of a fibril was 5-10 nm. Therefore hydrating the fibrils did not increase in the diameter of the fibrils as one would expect.
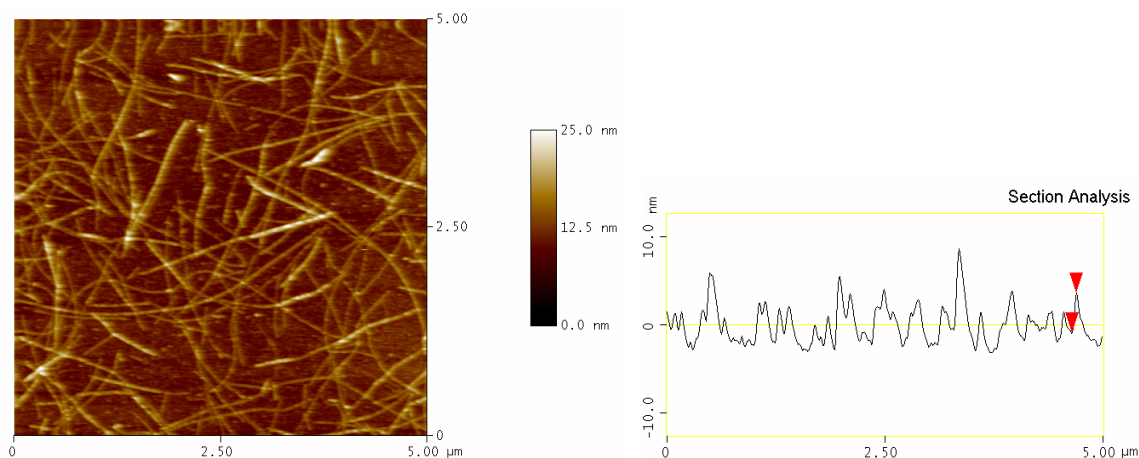
Figure 3.20   A 5 μm X 5 μm AFM image of fibrils underwater and line scan.

Fluorescence Microscopy

Since NSOM requires the fibril samples to be dry, fluorescence microscopy was utilized to image the fluorescence of ThT when bound to fibrils in solution. A small amount of a fibril/ThT solution was sandwiched between a coverslip and a microscope slide and then the sample was excited using a mercury lamp through a filter cube. Using a 100X oil immersion objective, the sample was brought into focus. At first it was hard to resolve the fibrils and we thought that there was no fluorescence, so a sample of the globular protein in solution, which is a by-product from making the fibrils, was stained with ThT and placed in the microscope. Since the globular protein was much larger than the individual fibrils, there was no problem resolving them in the microscope. Upon exciting the ThT bound to the globular protein, a bright green fluorescence was observed (Figure 3.21A). Afterwards, the sample containing only fibrils was placed back into the microscope and a fluorescence image of the ThT bound to the fibrils was obtained and green fluorescence observed (Figure 3.21B). In the image, individual fibrils could not be distinguished from one another; however, the sample solution contains a large

96

concentration of fibrils and the microscope was able to resolve where the fibrils overlap one another. The fluorescence microscope image clearly shows that the fluorescence comes from the ThT bound to the fibrils and not excess ThT dye floating around in the solution because fluorescence is not observed everywhere.
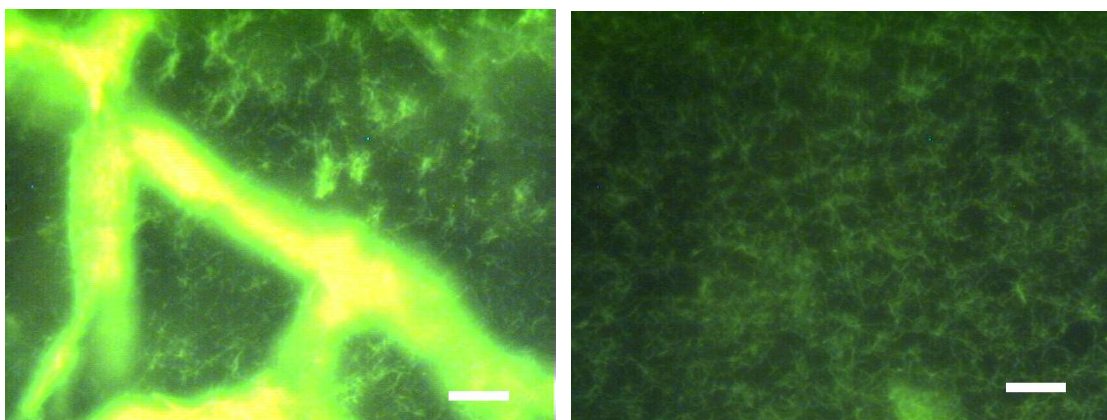
Figure 3.21 Fluorescence microscopy images of ThT bound to fibrils in water. A) Contains globular protein and ThT. B) Contains fibrils and ThT only. The scale bar in the images is 10 μm.

NSOM

NSOM was utilized to determine the orientation of ThT and BTA-2 when bound to the fibrils. Samples used for NSOM imaging were first imaged in the AFM to ensure fibrils were present on the surface and dispersed enough that individual fibrils could be imaged. The first NSOM images were obtained of ThT bound to fibrils. The sample was excited at 440 nm, which is the peak of the bound ThT excitation spectrum when in solution. The polarized fluorescence was split onto two different detectors and imaged along with the topography. Each pixel had to be integrated for 40 ms in order to obtain enough counts for detection. The topography showed a few fibrils present on the surface and they looked similar to what was observed in the AFM images. However, in the

fluorescence images, distinct polarized fluorescence was observed where there were fibrils in the topography. Figure 3.22a is the topography image obtained, Figure 3.22b is the vertical polarization, and Figure 3.22c is the horizontal polarization. In the vertical polarized image, there is only fluorescence where the fibril is oriented in the vertical direction, whereas in the horizontal fluorescence image, fluorescence was only observed where the fibrils were oriented in the horizontal direction. The fluorescence images clearly show that the ThT dye is oriented parallel to the fibril axis. However, the low fluorescence of the ThT and the background noise made it difficult to distinguish the real fluorescence from the background of the sample. Another factor is that the Stokes shift between the absorption and emission of the bound ThT is relatively small (40 nm) and in order to cut out most of the excitation light a 455 nm long pass filter was utilized; however, this also removed part of what little fluorescence there was to start. Therefore, we needed to find a way to increase the signal to noise ratio or find a more fluorescent dye to study.
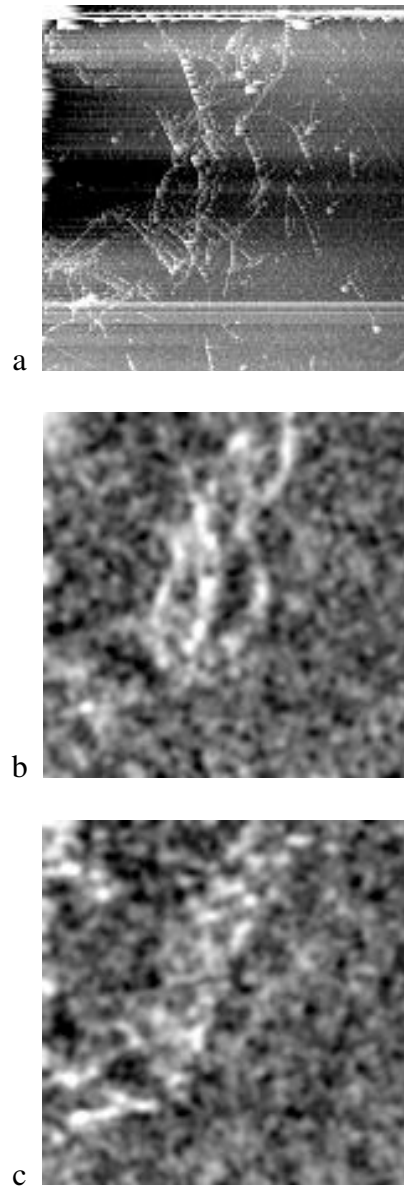
Figure 3.22   NSOM images of fibrils with ThT. A) Topography image of the fibrils. B) Fluorescence image in the vertical polarization. C) Fluorescence image in the horizontal polarization.

BTA-2 proved to be a nice alternative to ThT. BTA-2 has almost the same structure as ThT, but it is missing the methyl group on the benzothiazole N, making it an uncharged molecule. As discussed in the spectroscopy section, BTA-2 had an excitation maximum at ~380 nm and an emission maximum at ~425 nm in pH 2 water when bound to fibrils, this is a slightly larger Stokes shift than observed in ThT. However, when the film was excited at 405 nm, the excitation maximum significantly red-shifted to 538 nm, leading to a much larger Stokes shift than in solution. Since BTA-2 has a larger Stokes shift, it would be easier to filter out the excitation light and not eliminate most of the emission. Also Klunk *et al.* reported that BTA-2's binding affinity was 6-fold greater than ThT,[28] which would lead to more dye molecules binding and potentially lead to an increase in the fluorescence signal detected on the APD and MPD. Also BTA-2 could then be excited at 390-400 nm, which is the optimal emitting range for the Ti-Saph laser. The sample used for the NSOM experiments was the BTA-2 and fibril sample that had been diluted with pH 2 water. This sample was chosen because of the fluorescence spectrum obtained of the film using the single molecule setup, which had a significant amount of fluorescence and an emission maximum at ~538 nm. NSOM images of the fibrils were collected by exciting the sample at ~400 nm and collecting the polarized fluorescence. Figure 3.23 is the topography and the polarized fluorescence images of BTA-2 bound to amyloid fibrils. From the polarized fluorescence images, it was determined that the BTA-2's long axis was oriented parallel to the fibril axis; similar to the results observed in the ThT binding. A better signal-to-noise ratio was observed in the images; however, the number of fluorescent counts was still low (~60 counts max) and this was with an integration time of 40 ms. Although, BTA-2 did not significantly increase the signal to noise ratio, it still enabled us to finally obtain some good NSOM images of the amyloid fibrils.
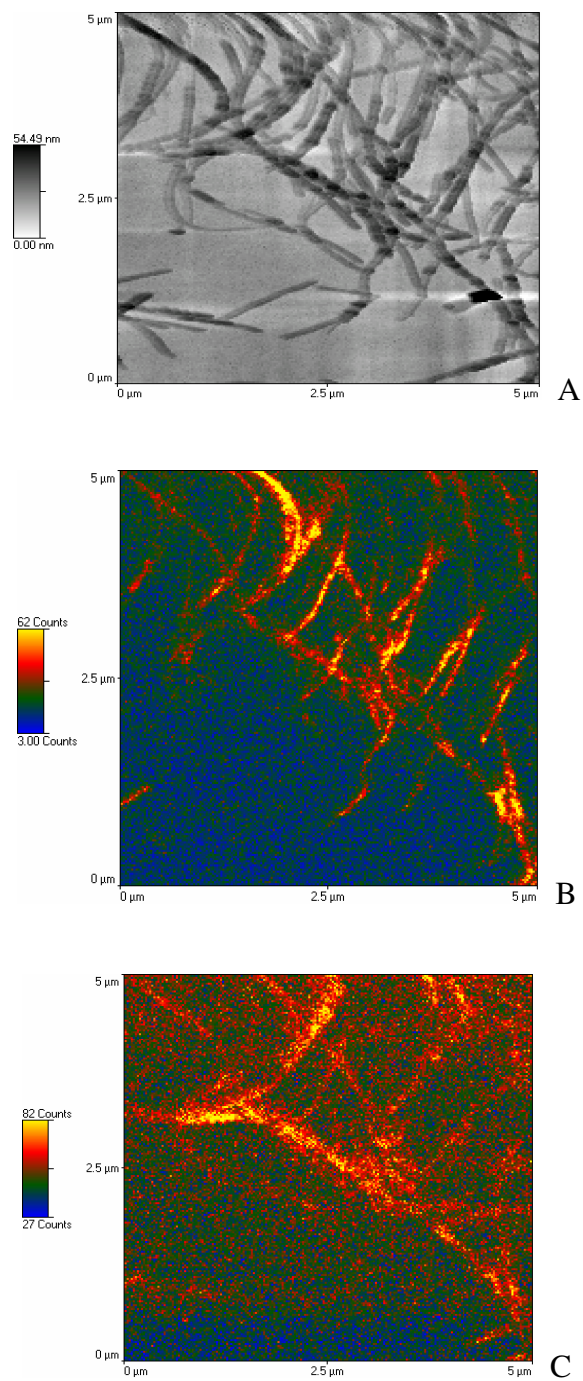
Figure 3.23 NSOM images of fibrils with BTA-2. A) The topography image of the fibrils. B) The fluorescence image in the vertical polarization. C) The fluorescence image in the horizontal polarization.

CONCLUSION

This research has shown the different spectral effects when different small molecule dyes bind to amyloid fibrils and probed the ThT and BTA-2 fluorescence when bound to fibrils using microscopy techniques. The spectroscopy of the dyes showed very dramatic results. In CR solutions, a small red-shift was observed in the absorption upon binding to the fibrils, and the emission spectrum had no shift, but enhanced fluorescence. The enhanced fluorescence indicates that the CR had bound to the fibrils as did the anisotropy data. However, CR's lack of fluorescence even in the presence of fibrils does not make it an ideal dye for use in NSOM studies. ThT was first studied due to its interesting spectral properties, which were already extensively reported on. When ThT is bound to amyloid fibrils a red-shift in the excitation spectrum was observed along with a several fold increase in the emission intensity, and the anisotropy data did confirm the binding to the amyloid fibrils. The lifetime decays showed that ThT had a faster lifetime in glycerin than when bound to fibrils, even though both solutions confined the rotation of the ThT. Another interesting phenomenon observed in ThT solution was the formation of micelles, which was determined by the nonzero anisotropy value obtained for ThT in water. The ThT concentration dependence plot showed that the increase in fluorescence was proportional to the increase in ThT concentration until all the binding sites had saturated and then the fluorescence decreased due to self-quenching of the excess dye.

The fluorescence microscopy images of ThT and fibrils provided evidence that all the fluorescence observed was coming directly from the ThT in the fibrils and not from excess dye in solution. This was also confirmed in the NSOM images, where the only fluorescence observed was from the fibrils. The polarized NSOM images also provided evidence that the ThT dye orients itself parallel to the fibril axis. ThT and CR have been

102

found to be amyloid specific dyes that show enhanced spectral characteristics when in the presence of amyloid fibrils.

BTA-2 proved to have very interesting spectral changes in different solutions and it was used as alternative dye to ThT. Differences in the emission spectra were observed when excited at either the absorption maximum or the excitation maximum. BTA-2 in pH 2 water solution had a distinct absorption peak at 430 nm, but the excitation spectrum was dramatically blue-shifted (peak at 365 nm) from the absorption peak. Similar results were observed for BTA-2 in a 1:1 mixture of water and CH_3CN, which had an excitation maximum at 400 nm and the absorption spectrum had a small peak at 430 nm. It was found that upon dilution that the 430 nm peak disappeared and a single peak at 360 nm was left. The 430 nm peak was then concluded to be due to micelle formation in the solution and the reason that no other peak was observed in the absorption of BTA-2 in pH 2 water was that the water promoted the formation of micelles. Then as the amount of CH_3CN was increased in solution the majority of the micelles dispersed into the solution. This counted for the differences in the emission spectrum when excited at 430 nm or the excitation maximum. Of the two solutions discussed in this chapter, BTA-2 binding only occurred in the solution diluted with pH 2 water. The solution diluted with a 1:1 mixture of water and CH_3CN did not yield any binding, which was determined from the lack of spectral shifts between the free BTA-2 and the bound, and also the anisotropy. It was surmised that the BTA-2 strongly favors CH_3CN in solution, and the CH_3CN forms a stabilizing solvent sphere around the BTA-2, while water prefers to solvate the fibrils, and thus the mixed solvents effectively shields the BTA-2 from the fibrils and prevents binding to the amyloid fibrils.

The NSOM images of BTA-2 bound to fibrils revealed that BTA-2 does bind parallel to the fibril axis, which is what one would expect since BTA-2 and ThT are

103

similar structurally. The fluorescence spectra of the BTA-2/fibrils films yielded information on where the emission occurs when excited at 405 nm. The BTA-2/fibril film made from the sample in pH 2 water had a red-shifted maximum relative to the solution emission maximum. The other BTA-2/fibril sample did have fluorescence but unfortunately the fluorescence was at the same peak as the background. This plus the fact that we now know that the BTA-2 does not actually bind to the fibrils in the 1:1 mixture of CH_3CN and water, did not make it an ideal sample for NSOM. Polarized NSOM images of BTA-2 did have a better signal to noise ratio than the ThT/fibril images; however, there were still not a lot of fluorescence from the sample. Therefore, future experiments would include trying to get more fluorescence signal in the NSOM images.

REFERENCES

1.   Fandrich, M.; Dobson, C. M., The behavior of polyamino acids reveals an inverse side chain effect in amyloid structure formation. *The EMBO Journal* **2002,** 21, (21), 5682-2690.

2.   Makin, O. S.; Serpell, L. C., Structures for amyloid fibrils. *The The FEBS Journal* **2005,** 272, 5950-5961.

3.   Murphy, R. M., Peptide Aggregation in Neurodegenerative disease. *Annual Review of Biochemistry* **2002,** 4, 155-174.

4.   Sipe, J. D., Amyloidosis. *Annual Review of Biochemistry* **1992,** 61, 947-975.

5.   Sunde, M.; Serpell, L. C.; Bartlam, M.; Fraser, P. E.; Pepys, M. B.; Blake, C. C. F., Common core structure of amyloid fibrils by synchrotron X-ray diffraction. *Journal of Molecular Biology* **1997,** 273, 729-739.

6.   Bouchard, M.; Zurdo, J.; Nettleton, E. J.; Dobson, C. M.; Robinson, C. V., Formation of insulin amyloid fibrils followed by FTIR simultaneously with CD and electron microscopy. *Protein Science* **2000,** 9, 1960-1967.

7.   Jimenez, J. L.; Nettleton, E. J.; Bouchard, M.; Robinson, C. V.; Dobson, C. M.; Saibil, H. R., The protofilament structure of insulin amyloid fibrils. *Proceedings of the National Academy of Sciences of the United States of America* **2002,** 99, (14), 9196-9201.

8.   Ban, T.; Yamaguchi, K.; Goto, Y., Direct Observation of amyloid fibril growth, propagation, and adaptation. *Accounts of Chemical Research* **2006,** 39, (9), 663-670.

9.   Dobson, C. M., Protein folding and misfolding. *Nature (London)* **2003,** 426, (6968), 884-890.

10.   Powers, E. T.; Powers, D. L., The Kinetics of Nucleated Polymerizations at High Concentrations: Amyloid Fibril Formation Near and Above the "Supercritical Concentration". *Biophysical Journal* **2006,** 91, 122-132.

11.   Khurana, R.; Ionescu-Zanetti, C.; Pope, M.; Li, J.; Nielson, L.; Ramirez-Alvarado, M.; Regan, L.; Fink, A. L.; Carter, S. A., A general model of amyloid fibril assembly based on morphological studies using atomic force microscopy. *Biophysical Journal* **2003,** 85, 1135-1144.

12.   Turnell, W. G.; Finch, J. T., Binding of the dye Congo Red to the amyloid protein pig insulin reveals a novel homology amongst amyloid-forming peptide sequences. *Journal of Molecular Biology* **1992,** 227, 1205-1223.

13.   Klunk, W. E.; Jacob, R. F.; Mason, R. P., Quanitfying amyloid by Congo red spectral shift assay. *Methods in Enzymology* **1999,** 309, 285-305.

14.   Khurana, R.; Uversky, V. N.; Nielson, L.; Fink, A. L., Is Congo Red an Amyloid Specific Dye? *Journal of Biological Chemistry* **2001,** 276, (25), 22715-22721.

15.   Benditt, E. P.; Eriksen, N.; Berglund, C., Congo Red Dichroism with Dispersed Amyloid Fibrils an Extrinsic Cotton Effect. *Proceedings of the National Academy of Sciences of the United States of America* **1970,** 66, (4), 1044-1051.

16.   Klunk, W. E.; Debnath, M. L.; Pettegrew, J. W., Development of small molecule probes for the beta-amyloid protein of Alzheimer's Disease. *Neurobiology of Aging* **1994,** 15, (6), 691-698.

17.   Jin, L.-W.; Claborn, K. A.; Kurimoto, M.; Geday, M. A.; Maezawa, I.; Sohraby, F.; Estrada, M.; Kaminsky, W.; Kahr, B., Imaging linear birefringence and dichroism in cerebral amyloid pathologies. *Proceedings of the National Academy of Sciences of the United States of America* **2003,** 100, (26), 15294-15298.

18.   Levine, H. I., Multiple ligand binding sites on AB(1-40) fibrils. *Amyloid* **2005,** 12, (1), 5-14.

19.   Mourtzis, N.; Cordoyiannis, G.; Nounesis, G.; Yannakopoulou, K., Single and double threading of Congo red into y-Cyclodextrin. Solution structures and thermodynamic parameters of 1:1 and 2:2 adducts, as obtained from NMR spectroscopy and microcalorimetry. *Supramolecular Chemistry* **2003,** 15, (7-8), 639-649.

20.   Dzwolak, W.; Pecul, M., Chiral bias of amyloid fibrils revealed by the twisted conformation of Thioflavin T: An induced circular dichroism/DFT study. *FEBS Letters* **2005,** 579, 6601-6603.

21.   Krebs, M. R. H.; Bromley, E. H. C.; Donald, A. M., The binding of thioflavin-T to amyloid fibrils: localisation. *Journal of Structural Biology* **2005,** 149, 30-37.

22.   Khurana, R. C., Chris; Ionescu-Zanetti, C.; Carter, S. A.; Krishna, V.; Grover, R. K.; Roy, R.; Singh, S., Mechanism of thioflavin T binding to amyloid fibrils. *Journal of Structural Biology* **2005,** 151, (3), 229-238.

23.   Voropai, E. S.; Samtsov, M. P.; Kaplevskii, K. N.; Maskevich, A. A.; Stepuro, V. I.; Povarova, O. I.; Kuznetsova, I. M.; Turoverov, K. K.; Fink, A. L.; Uverskii, V. N., Spectral properties of Thioflavin T and its complexes with amyloid fibrils. *Journal of Applied Spectroscopy* **2003,** 70, (6), 868-874.

24.   Levine, H. R., Quantification of beta-sheet amyloid fibril structures with Thioflavin T. *Methods in Enzymology* **1999,** 309, 274-284.

25.   Nielson, L.; Frokjaer, S.; Brange, J.; Uversky, V. N.; Fink, A. L., Probing the mechanism of insulin fibril formation with insulin mutants. *Biochemistry* **2001,** 40, 8397-8409.

26.   Nielson, L.; Khurana, R.; Coats, A.; Frokjaer, S.; Brange, J.; Vyas, S.; Uversky, V. N.; Fink, A. L., Effect of environmental factors on the kinetics of insulin fibril formation: Elucidation of the molecular mechanism. *Biochemistry* **2001,** 40, 6036-6046.

27.   LeVine III, H., Thioflavin T interaction with synthetic Alzheimer's disease β-amyloid peptides: Detection of amyloid aggregation in solution. *Protein Science* **1993,** 2, 404-410.

28.   Klunk, W. E.; Wang, Y.; Huang, G.-f.; Debnath, M. L.; Holt, D. P.; Mathis, C. A., Uncharged thioflavin-T derivatives bind to amyloid-beta protein with high affinity and readily enter the brain. *Life Sciences* **2001,** 69, 1471-1484.

29.   Alagille, D.; Baldwin, R. M.; Tamagnan, G., One-step synthesis of 2-arylbenzothiazole ('BTA') and -benzoxazole precursors for in vivo imaging of β-amyloid plaques. *Tetrahedron Letters* **2005,** 46, 1349-1351.

30.   Ye, L.; Morgenstern, J. L.; Lamb, J. R.; Lockhart, A., Characterisation of the binding of amyloid imaging tracers to rodent AB fibrils and rodent-human AB co-polymers. *Biochemical and Biophysical Research Communications* **2006,** 347, 669-677.

31.   Klunk, W. E.; Wang, Y.; Huang, G.-f.; Debnath, M. L.; Holt, D. P.; Shao, L.; Hamilton, R. L.; Ikonomovic, M. D.; Dekosky, S. T.; Mathis, C. A., The binding of 2-(4'-methylaminophenyl) benzothiazole to postmortem brain homogenates is dominated by the amyloid component. *Journal of Neuroscience* **2003,** 23, (6), 2086-2092.

Chapter 4: A pH dependent study of Congo red and Thioflavin T binding to amyloid fibrils using isothermal titration calorimetry

INTRODUCTION

Amyloid fibrils have become an area of increasing interest due to their role in over 20 different neurodegenerative diseases (e.g. Alzheimer's disease, Creutzfeldt-Jakob);[1-6] however, the cause of these diseases is still unknown. Each neurodegenerative disease is associated with a specific protein that misfolds and self-assembles with other similar misfolded proteins to form highly ordered, stable aggregates.[1, 7-10] Although, the proteins associated with these diseases form amyloid fibrils, researchers have found that other proteins not associated with neurodegenerative diseases will also form amyloid fibrils.[11, 12] This suggest that the ability to form amyloid fibrils is related to the polypeptide backbone of proteins and may be generic to all polypeptides.[3] The structure of the amyloid fibrils consists of anti-parallel β-sheets which are perpendicular to the fibril axis.[7] This β-sheet structure has been extensively studied using atomic force microscopy (AFM),[8, 9, 13] x-ray diffraction,[7, 14] fluorescence spectroscopy,[2, 10, 15] Fourier transform infrared spectroscopy (FTIR),[14] electron microscopy,[16] circular dichroism (CD),[14] and total internal reflection fluorescence microscopy (TIRFM).[17]

A common method for characterizing amyloid fibrils, which has been extensively utilized, is staining the fibrils with Congo red (CR) or thioflavin T (ThT) dyes and studying them via spectroscopy.[1, 11, 13, 18-20] Typically, researchers have classified fibrils as amyloid fibrils if they bind CR and ThT.[1, 5] These dyes are thought to be amyloid specific and they exhibit changes in their spectral properties when bound to amyloid fibrils. When CR is bound to amyloid fibrils, an apple green birefringence is observed when

viewed through cross polarizers.[20-24] When ThT binds to amyloid fibrils the excitation spectrum red-shifts to 450 nm and the fluorescence spectrum has enhanced emission at 482 nm.[11, 13, 19, 25, 26] CR and ThT were thought to bind to amyloid fibrils because of the ordered β-sheet structure.[11, 22] However, researchers have found that these dyes will not always bind to amyloid fibrils.[18, 27] Shinchuk *et al.* synthesized polyalanine, which formed amyloid fibrils, but observed no binding of CR or ThT.[27] Originally it was thought that CR would not bind to proteins in their native conformation because when CR was in the presence of native proteins no birefringence was observed [28]. However, it was later determined that CR does indeed bind to proteins in their native conformations.[29] This would suggest that the green birefringence is a product of the CR binding to amyloid fibrils specifically and not just too any protein. Given the common use of these dyes as assays for amyloid fibrils and the questions about their specificity it would be beneficial to further understand the binding mechanism of CR and ThT in order to better define what is considered an amyloid fibril.

Previous researchers have studied how CR binds to amyloid fibrils and have concluded that the CR binds parallel to the fibril axis [23]. While other scientists have studied the binding mechanism of CR to amyloid fibrils and proteins in order to determine which interactions are the most dominate.[20, 22, 30] The binding mechanism has been thought to be either due to hydrophobic interactions from aromatic -stacking,[21, 24] from electrostatic interactions between the charged sulfate groups on the CR and positively charged amino acids on the protein,[20, 28, 30, 31] or a combination of both. Even though there is evidence to support both mechanisms, the most widely excepted theory is that electrostatic interactions dominate CR binding to proteins.

The mechanism of ThT dye binding to amyloid fibrils is more complicated. Previous researchers have studied the ThT orientation within the β-sheets of the amyloid

fibrils. Krebs *et al.* found that ThT mostly likely inserts itself into the channels of the β-sheets, with its long axis parallel to the fibril axis[11]. The close proximity of ThT to the side chains of the β-sheets causes ThT to planarize, which yields an enhance fluorescence signal at 482 nm.[11, 19] Most recently Khurana *et al.* suggested that ThT forms micelles above 4 μM and it is these micelles that bind to amyloid fibril causing the enhance fluorescence.[13] However, it is unlikely that this mechanism is ubiquitous as micelles should have complicated the polarized fluorescence in the Krebs *et al.* study.[11]

In this paper we investigated the interactions of CR with insulin and insulin amyloid fibrils, and ThT with insulin amyloid fibrils using isothermal titration calorimetry (ITC). ITC is a sensitive technique for studying the binding interactions between proteins and ligands.[32-34] When binding occurs, the ITC measures the change in heat needed to keep the sample cell at a constant temperature with respect to a reference cell. From the ITC data, the binding constant, binding stoichiometry, enthalpy, and entropy can be extrapolated from a single experiment. The thermodynamic values obtained from the ITC data can then be used to gain more information into the specific interactions involved in the binding of CR and ThT to amyloid fibrils. Very few researchers have used ITC to explore amyloid fibrils and the binding of CR and ThT. One researcher used ITC to directly measure the thermodynamic parameters of fibril formation of β2m.[35] While another researcher studied the copper binding affinity to stefin B at two different pHs.[36] Kim *et al.* has been the only one to utilize ITC to study CR binding to amyloidgenic immunoglobulin light chain variable domains (SMAs) at pH 7.4; however, they only studied at the binding at one pH.[30] In this paper, the effects of pH on the dye binding to amyloid fibrils is explored. The bovine insulin monomer structure contains several charged amino acid with various pK_as: three positively charged amino acids (two histidines, one lysine, and one arginine) and four negatively charged glutamic

109

acids.[37] These amino acids can be protonated or deprotonated by changing the pH of the solution. Kim *et al.* claimed that CR binds by electrostatic forces; it was hypothesized that if CR binds to insulin by electrostatic forces then by deprotonating one of the amino acids in the protein, CR binding should be reduced.[30] The interactions that bind ThT to amyloid fibrils are still debatable, given that two different researchers have proposed different binding mechanisms.[11, 13] To determine if electrostatic interactions or hydrophobic interactions are the most dominate, ThT was bound to amyloid fibrils at two different pHs, one at a physiological pH and the other below the pK_a of glutamic acid. To determine how elimination of the negatively charged residues would affect binding of the positively charged ThT.

EXPERIMENTAL

Materials

Bovine insulin, Congo red (CR), and Thioflavin T (ThT) were used as purchased from Sigma-Aldrich and without further purification. Stock fibrils were made by dissolving insulin in pH 2 water and heating at 60°C for 24 hours. After heating the fibrils were sonicated until any large globules were broken up.

Sample Preparation

Buffer solutions were made consisting of 10 mM potassium phosphate/10 mM sodium carbonate/100 mM NaCl for studies done at pH 7.4 and pH 11. For studies done at pH 6.6, a buffer solution consisting of 10 mM potassium phosphate/10 mM sodium acetate/100 mM NaCl was made. Studies done at pH 3, a buffer solution containing of 10 mM potassium phosphate/10 mM malic acid/100 mM NaCl was made. CR and ThT solutions were prepared by dissolving solid CR or ThT in buffer. CR solutions were made at pH 7.4 or pH 11.1, while ThT solutions were made in pH 6.6 or pH 3 buffer.

110

Insulin solutions were made by dissolving monomeric insulin in either pH 7.4 or pH 11.1 buffer. The fibril solution used for ITC was made by diluting a portion (3mL) of stock fibril solution with stock buffer solution at either pH 6.6 or pH 3. The pH of all the solutions were checked and adjusted with 1 M NaOH or 1 M HCl if needed before the final dilution in order to maintain a constant pH in all solutions.

Determination of optimal fibril formation

For the fibril solutions used in the ITC, it was important to ensure that the solution contain mostly fibrils and little free insulin monomer; therefore, it was important to determine the optimal conditions for forming fibrils. Two different experiments were done, one to determine how long to heat the solution and the other to determine if stirring the solution while heating increased the fibril amount. The samples were ultracentrifuged to separate the fibrils from the free insulin in order to determine the amount of insulin that fibrillized. The first series of experiments heated three insulin solutions from the same stock solution at pH 2 for three different lengths of time: 3 hours, 6 hours, and 20.5 hours. After heating the samples were placed in a refrigerator until centrifuging. The samples were ultracentrifuged at 41,000 rpm for 1 hour at 8 °C. Afterwards the supernatant layer was removed and an absorption spectrum of each supernatant was taken to determine the amount of unfibrillized monomer (the extinction coefficient of insulin in pH 2 water, ε_{280}= 4392 cm^{-1}*M^{-1}). The percent of fibrillized monomer was calculated and was found to be 29.2 % for 3 hours, 24.8 % for 6 hours, and 36.7 % for 20.5 hours. Therefore it determined that to form the most fibrils the insulin solutions should be heated for at least 20.5 hours. Similarly, another experiment was conducted to determine if while heating the insulin solutions, they should be incubated or stirred to optimize the fibril formation. Two solutions, one stirred the other incubated, consisting of the same concentration of insulin in pH 2 water were heated for 24 hours at 60 °C. When finished

heating the solutions were ultracentrifuged, and the supernatant layer removed. An absorption spectrum (using the same extinction coefficient as stated above) was taken of the supernatant and the concentration of monomeric insulin remaining was calculated. The percent fibrillized was calculated to be 66.6 % for the stirred sample and 38.1 % for the incubated solution. It was then concluded that stirring the insulin solution formed the most fibrils. To ensure the greatest percentage of fibrils for the ITC experiment fibril solutions were made by heating and stirring for 24 hours.

Isothermal Titration Calorimetry (ITC)

The thermodynamics of CR binding to insulin and ThT binding to insulin fibrils was measured using a MicroCal VP-ITC microcalorimeter. All samples were degassed for ~20 min. before each titration. The CR binding to insulin experiments were done at 8°C, 26°C, and 46°C with 3.54 mM CR in the titrant syringe and 0.20 mM insulin in the sample cell, the reference cell contained pH 7.4 buffer. The CR binding to insulin experiments at pH 11.1 were done at the same temperature with similar concentrations (3.8 mM CR, 0.25 mM insulin). The ThT binding to fibrils experiments were done at 30°C, 45°C, and 60°C with 5.11 mM ThT in the titrant syringe and 0.71 mM fibrils (fibril concentration is based on the concentration of insulin monomer) in the sample cell, the reference cell contained pH 6.6 buffer. The ThT binding to fibrils experiments at pH 3 were done at the same temperatures and similar concentrations (5.18 mM ThT, 0.65 mM fibrils). The syringe stirred the sample cell at 450 rpm and delivered 10 μL injections over 20 s and a 480 s spacing was used between injections to ensure baseline equilibration. A background titration was obtained by titrating the same concentration either of CR or ThT used in the binding studies into buffer (the only parameter changed was the injection spacing to 360 s). Once the ITC run was started the data was collected automatically. After a binding study and background had been obtained, the data was

analyzed using Origin software from MicroCal. The background was subtracted from the binding data to account for heat of dilution. The MicroCal software offers three different curve fits: single set of identical sites, two sets of independent sites, and sequential binding sites that can be any number of sites. In the following equations: K is the binding constant, n is the number of binding sites, V_o is the active cell volume, M_t and [M] are the bulk and free concentration of macromolecule in V_o, X_t and [X] are the bulk and free concentration of ligand, Θ is the fraction of sites occupied by ligand X, Q is the total heat content of the solution in V_o, and ΔH is the molar heat of ligand binding. Equations for single set of identical sites:

$$K = \frac{\Theta}{(1-\Theta)[X]}$$
$$X_t = [X] + n\Theta M_t$$
$$Q = n\Theta M_t \Delta H V_o$$

Equations for two sets of independent sites:

$$K_1 = \frac{\Theta_1}{(1-\Theta_1)[X]}$$
$$K_2 = \frac{\Theta_2}{(1-\Theta_2)[X]}$$
$$X_t = [X] + M_t(n_1\Theta_1 + n_2\Theta_2)$$
$$Q = M_t V_o(n_1\Theta_1\Delta H_1 + n_2\Theta_2\Delta H_2)$$

The equations for sequential binding are more involved and are further explained in MicroCal's ITC data analysis in Origin® tutorial guide. After the ITC runs were completed, the solution in the sample cell containing fibril and ThT was removed and saved for ultracentrifugation.

ITC Technique

One of the most common uses of isothermal titration calorimetry (ITC) is to study protein interactions with small molecules or ligands. Understanding the interactions that occur when the ligands bind to the protein can yield useful information about the system. In particular, thermodynamic parameters can give information about the binding and other non-covalent bonds formation and breaking. A variety of methods are still used to determine the thermodynamic parameters of binding, one method is the van't Hoff analysis, which requires several experiments at different temperatures. Currently there are only two methods for the direct measurement of enthalpy, ITC and differential scanning calorimetry (DSC is discussed in Chapter 1). ITC is very sensitive technique that allows for the precise values enthalpy to be obtained and it can measure changes in heats on the μcal scale. One advantage to using ITC is it allows the researcher to study the interactions in physiological conditions with the protein free in solution. Another advantage is that in a single experiment the enthalpy, entropy, Gibb's Free energy, equilibrium constant, and binding stoichiometry terms can all be calculated. Subsequently, the change in heat capacity can also be determined by doing the experiment at different temperatures.

The ITC instrument design consists of two cells, a sample cell and a reference cell, and a syringe containing the titrant. The sample cell and reference cell are then maintained at a constant temperature throughout the entire experiment. In the MicroCal VP-ITC (Figure 4.1), which was used in our experiments, an adiabatic shield is placed between the cells and the surroundings, so that during an experiment when there is a change in the temperature of the sample cell compared to the reference cell, it is recorded as the binding energy. A thermocouple in the instrument is used as a feedback mechanism to make sure that when there is a temperature change in the sample cell heat

can be added or limited in order to maintain thermal equilibrium with the reference cell. Then if an exothermic process occurs, the feedback power will decrease and for an endothermic process the feedback power will increase as needed. After binding occurs, the feedback power returns to the baseline power and both cells are back at equilibrium. ITC experiments are easy to perform and can be done quickly in the span of a couple of hours because of the baseline stability and rapid equilibration between injections.
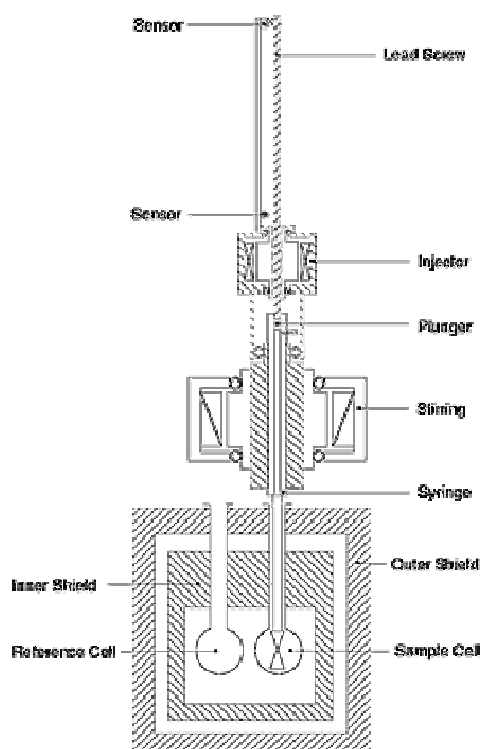
Figure 4.1   A diagram of the ITC showing the syringe, the sample cell and reference cell. Reprinted from http://www.microcal.com.

In an actual experiment, the sample contains the protein in a buffer solution and the reference contains just the buffer solution. Then a syringe containing the binding partner, the ligand, is placed into the sample cell. The syringe is contained in a spinner

115

with an automated plunger at one end controlled by a stepper motor. This allows for the syringe to rotate freely during the experiment and also to accurately inject a set amount of ligand into the sample cell. The end of the syringe is a flat paddle that stirs during the experiment to make sure a rapid mixing occurs within a few seconds after each injection. The ITC is controlled by a computer program where the temperature, the number of injections, the amount of each injection and other timing controls are inputted. The experiment is started and the computer is controls the experiment. During an experiment, the ligand in the syringe is titrated into the sample cell in set aliquots. Then the heat released or absorbed in the sample cell is measured in respect to the reference cell is measured in electrical power (μcal/s). This change in electrical power is the amount needed to maintain a constant temperature between the sample and reference cell. The first injection usually generates the most heat, since most of the ligand added binds to the protein. Then as more of the ligand is titrated into the sample, the resulting heat from the binding decreases as more of the binding sites are occupied. Eventually, all the available binding sites will be occupied and no more heat from binding will be observed in the baseline saturation. Then upon subsequent injections, any small heat changes are caused by the dilution of the titrant. When the titration is finished the data can be worked up in MicroCal's fitting software.

The peaks in the binding isotherm represent the sum of the heats associated with binding plus any other changes in the equilibrium during the titrations, it is considered to be change in enthalpy observed, ΔH_{obs}. Some other processes which can take place are ion exchange, pH changes, and ligand dilution. Therefore it is important to run background titrations so that any additional heats, evolved or absorbed, can be taken into account. For the most part a titration of the ligand solution into buffer is the only background titration that needs to be preformed. Ion exchange and pH changes should

produce very little heat if the ITC solutions were made carefully to ensure that each solution has the same concentrations of buffer and each has the exact same pH. Once a background titration is preformed, it can then be subtracted from ΔH_{obs} to obtain the enthalpy of binding at each injection. The peak of each injection are then integrated and plotted as kcal/mole of injectant versus the molar ratio of the components. This produces points that can be fitted with different binding models, such as: one to one independent binding model, two to one independent binding model, and a sequential binding model that has an unlimited number of sites that can used. From the best fit, the enthalpy and the binding constant can be calculated, and from there the entropy and Gibb's free energy can be calculated.

Ultracentrifugation

Ultracentrifugation was performed using a Beckman Optima TLX Ultracentrifuge. All the ITC samples containing ThT and fibrils at pH 6.6 and pH 3 were centrifuged along with the original fibril solution used in the ITC titrations. The samples were place in Beckman Quick-seal centrifuge tubes (Polyallomer, capacity 3.9 mL). The samples were inserted into the tubes using a syringe and the mass added was noted, then the samples were diluted with the appropriate buffer to the top of the tube. The centrifuge tubes were heat sealed. The samples were centrifuged at speed of 41,000 rpm for 1hour at 15 °C. After centrifuging the tops were cut off the tubes and the supernatant liquid was removed from each sample. The samples were analyzed using absorption spectroscopy to determine the concentration of ThT that did not bind to the fibrils or the amount of monomeric insulin that did not fibrillize.

Absorption Spectroscopy

Absorption spectra were obtained using a Beckman Coulter DU800 spectrophotometer. Absorption spectra were taken of the ITC solutions before titration to determine the actual concentrations and of the supernatant layers from ultracentrifugation samples. The spectra were collected using a Starna cuvette with a path length of 1 cm. Beer's law plots were done for all solutions used at the different pHs. The following extinction coefficients were determined: $\varepsilon_{500\ nm} = 34676\ M^{-1}cm^{-1}$ (CR at pH 7.4), $\varepsilon_{500\ nm} = 35018\ M^{-1}cm^{-1}$ (CR at pH 11), $\varepsilon_{412\ nm} = 19231\ M^{-1}cm^{-1}$ (ThT at pH 6.6), $\varepsilon_{412\ nm} = 21047\ M^{-1}cm^{-1}$ (ThT at pH 3), $\varepsilon_{280\ nm} = 4861.2\ M^{-1}cm^{-1}$ (insulin at pH 3), $\varepsilon_{280\ nm} = 4800\ M^{-1}cm^{-1}$ (insulin at pH 6.6), $\varepsilon_{280\ nm} = 4833.2\ M^{-1}cm^{-1}$ (insulin at pH 7.4), and $\varepsilon_{280\ nm} = 6104.3\ M^{-1}cm^{-1}$ (insulin at pH 11). All Beer's law plots were done using the same dual buffer systems as described above.

Fluorescence

Photon Technologies International Quanta Master Model C Cuvette based scanning fluorometer. Samples were excited at 440 nm. Bandpass filters of appropriate wavelength were used to ensure a monochromatic excitation beam. Long pass filters were used in the emission path to help eliminate scattered excitation light.

RESULTS AND DISCUSSION

Congo red binding to insulin/fibrils

ITC was used to determine the thermodynamic parameters of CR binding to fibrils at two different pHs. Figure 2B shows example isotherm of CR (3.256 mM) binding to fibrils (0.2076 mM) in a pH 7.4 buffer solution at 26 °C. The fibril concentration was determined after ultracentrifuging the ITC fibril solution using absorption spectroscopy and was calculated on an insulin monomer basis. The data

shows exothermic peaks as the CR is titrated into the fibril solution until all the binding sites have saturated at the baseline and the peaks become endothermic (Figure 4.2B). The endothermic peaks at the end of the titration are caused by excess CR being diluted, which is confirmed by a background titration of CR into buffer (Figure 4.2A). In the raw background titration, the first peak is the largest followed by steadily decreasing peaks as the concentration of available binding sites become occupied. CR has previously been found to form micelles in solutions of high ionic strength or above concentrations of ~5 μM[29, 38] and therefore the endothermic peaks seen in the raw background ITC data are the result of micelles dispersion.[30] The raw background ITC data was subtracted from the raw CR binding data, and the integrated peaks were then plotted as a function of heat/mole of injectant versus the CR molar ratio using MicroCal's Origin software (Figure 4.2C). The background subtraction is not exact because the amount of free CR present after the first injection in the binding isotherm is not equivalent to the amount of free CR in the background titration for the same injection. This is due to the fact that most of the CR binds to the fibrils leaving only a small portion of free CR. Now the amount of free CR in the background titration for the next injection is greater than in the binding isotherm for the same peak; however, the heat absorbed from the background titration has to be taken into account. As such, there is a small error from the direct subtraction of the background. Other background titration were done by titrating buffer into buffer and titrating buffer into the fibril solution to determine if any other process generated heat that needed to be taken into account. However, neither titration evolved a significant amount of heat (0.01-0.04 μcal/s) and thus was not subtracted from the binding isotherm. The plot of CR binding to fibrils at 26 °C showed one clear inflection point and the best fit obtained for the data was a two independent binding site model. However, the total binding stoichiometry is approximately one, which suggests that one

119

CR molecule binds to every one insulin monomer, since the fit was determined using the concentration of insulin monomer present.
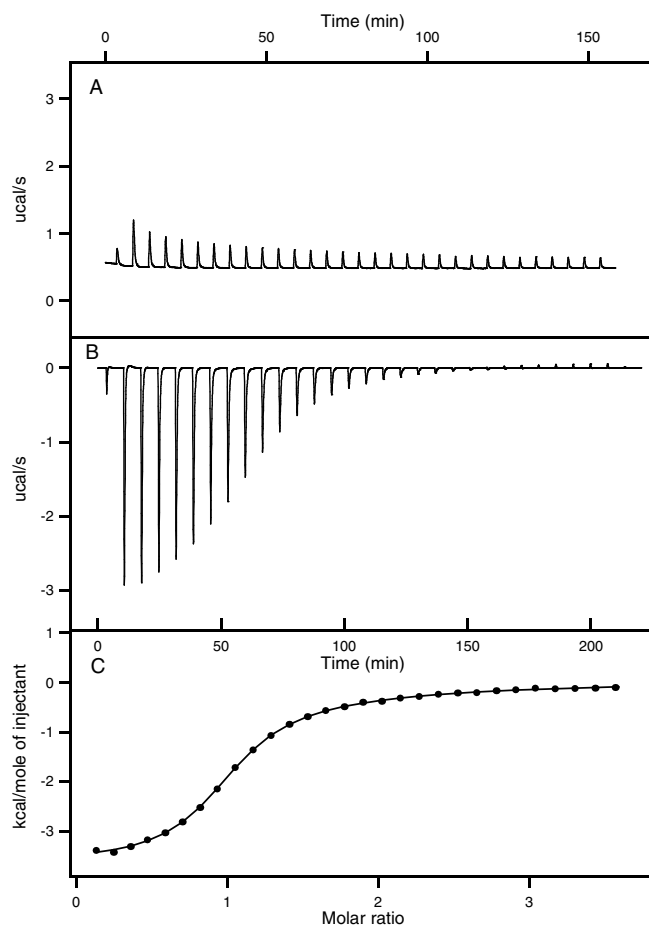
Figure 4.2   CR binding to fibrils in a pH 7.4 buffer solution at 26 °C, A) is the raw titration of a 3.256 mM CR solution into pH 7.4 buffer solution, B) is the raw titration data of the CR solution into a 0.2076 mM insulin solution, and C) is the integrated data that was fit.

The ITC solutions, from the sample cell after the titration, were ultracentrifuged as another way to quantify the binding stoichiometry. Upon absorption analysis of the supernatant removed after centrifugation, it was observed that only a small percentage of CR was bound to the fibrils (~7%). However, the binding isotherms showed that binding

120

was not saturated until more than half the total CR was injected into the sample. The fibril solution used for the ITC was then ultracentrifuged to determine the percentage of fibrillized insulin monomer present, which was calculated to be only 14% (the fibril solutions used for these experiments were done prior optimizing the fibrillization procedure). Since the ITC showed more CR binding being observed than the ultracentrifugation data, a titration of CR into insulin monomer was preformed to determine if CR bound to the free insulin monomer or if there was another equilibrium that needed to be taken into account for the background. The titration of CR into an insulin monomer solution revealed an isotherm with exothermic peaks nearly identical to those seen in the CR binding to fibrils.

Titrations of CR binding to both fibrils and insulin were obtained at pH 7.4 to determine if there was a difference between the binding of CR to insulin and fibrils. A CR solution (3.5 mM) was titrated into an insulin solution (0.2 mM) at pH 7.4 at three different temperatures (8 °C, 26 °C, and 46 °C) and the other CR into fibrils titration was described above were done at the same pH and temperatures. The fibrils solutions contained both fibrils and free monomeric insulin in the solution. The percent of fibrils present in the solution was determined through ultracentrifugation and was discussed above. The binding of CR to insulin data showed one clear inflection point with the best fit being a two independent binding model at 26 °C, similar to the above results when CR was titrated into a fibrils solution. Figure 4.3 shows an overlay of the binding curves of CR being titrated into fibrils and insulin at 26°C, which have approximately the same slope. At 46 °C, both binding studies used a two independent binding model, while binding studies preformed at 8 °C had a better fit with a single binding model. The decrease in binding at 8 °C could be the result of fewer binding sites being exposed on the protein at lower temperatures.[30] Then as the temperature increases, more binding sites

are exposed and more CR molecules are able to bind. At 26 °C the total binding stoichiometry (n) of CR binding to insulin was 1.36, while at the same temperature the binding stoichiometry of CR binding to fibrils was 2.12. Since the binding stoichiometries of CR binding to insulin and fibrils at the same temperature are close this would indicate that the CR binding mechanism does not change significantly when the insulin is fibrillized. This suggests that CR will bind to insulin in its native conformation; however, when CR does bind to amyloid insulin fibrils the only way to differentiate the binding between the native and the fibrils is through microscopy, specifically birefringence. This corresponds to what other researchers have observed.[29, 38]
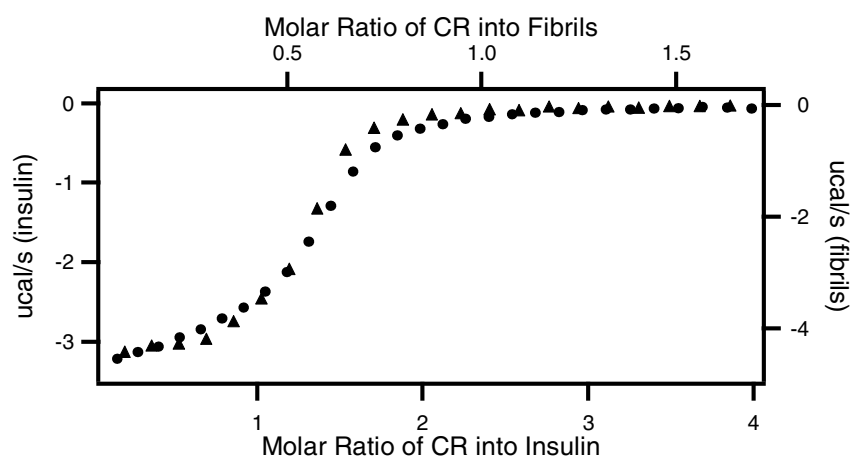
Figure 4.3   Overlay of binding isotherms from CR binding to fibrils (▲) and CR binding to insulin (●).

The CR binding results at pH 7.4 are summarized in Table 4.1, including the thermodynamic parameters calculated from both the ITC fitting analysis for insulin and the fibrils. The equilibrium constants for each experiment were on the order of 10^4 to 10^6 M^{-1}, indicating that CR binding is highly favorable. The large negative enthalpies, -3 to -4 kcal/mol, suggest that electrostatic interactions are significant in the CR binding to insulin. For all the binding constants there was a comparable entropy contribution

observed. The entropy contribution is expectant for the electrostatic binding as a result of freeing of the solvation shell around the charges. Again these results were the same whether in the presence of fibrils or just the insulin monomer. Therefore the electrostatic interactions between the negatively charged sulfate groups of the CR and positively charged amino acid side chains of lysine and arginine on the insulin backbone are the most dominant and not hydrophobic interactions from aromatic -stacking. These results are similar to what Kim *et al.* observed when CR bound to amyloidgenic immunoglobulin light chain variable domain (SMAs) using ITC.[30]

Temperature	Insulin			Fibrils		
(°C)	8	26	46	8	26	46
N_1	1.72	0.97	0.18	1.20	1.16	0.61
K_1 (M^{-1})	$3.61*10^4$	$9.79*10^4$	$1.67*10^8$	$1.67*10^4$	$7.35*10^3$	$4.01*10^5$
H_1 (kcal/mol)	-3.15	-3.01	-4.33	-3.98	-0.69	-4.994
T S_1 (kcal/mol)	2.71	3.82	7.68	1.45	4.60	3.19
N_2		0.39	0.87		0.96	0.014
K_2 (M^{-1})		$2.28*10^6$	$3.40*10^5$		$2.44*10^5$	$3.82*10^4$
H_2 (kcal/mol)		-3.26	-4.28		-3.64	$-1.25*10^2$
T S_2 (kcal/mol)		5.44	3.80		3.73	$-1.18*10^2$

Table 4.1   A summary thermodynamic parameters for CR binding to insulin and fibrils in a pH 7.4 solution at different temperatures.

To test the hypothesis that the CR binding to insulin is dominated by electrostatic forces, the pH of the solution was increased to pH 11.1 in order to deprotonate the positively charged lysine (pK$_a$ 10.4-11.1). By deprotonating the lysines the only positively charge amino acid left is arginine (pK$_a$ 12.0) and therefore a reduction in binding is expected for a process dominated by electrostatic interactions. A higher pH was not used because pH 11.1 is the end of the effective pH region for carbonate. The

CR binding was only investigated using insulin solutions, since it was determined from the above results that CR binds to fibrils and insulin monomer by a similar binding mechanism. The titrations of CR (0.25 mM) into insulin monomer (3.8 mM) were performed in a pH 11.1 buffer solution at 8 °C, 26 °C, and 46 °C. Figure 4 shows the background titration, binding isotherm, and the integrated data with its fit at 8 °C. The ITC results were different from the binding studies preformed at pH 7.4. First, there was a significant reduction in the heat evolved in each injection. The binding peaks were still exothermic, but the data never saturated at the baseline (Figure 4.4B). Typically the insulin concentration would be increased to obtain more signal, but this would mean the CR concentration would subsequently need to be increased as well. However, at ~4 mM the CR is almost a saturated solution and will begin to crash out of solution beyond this concentration. The largest peak in the isotherm was ~-1.2 μcal/s, which is ~-2.3 μcal/s less than the first peak in the binding isotherm at pH 7.4 (these values can be roughly compared since the concentrations used for both studies were approximately the same). The data was fit with a two independent binding site model (Figure 4.4C); however, the binding stoichiometry was reduced to 0.47 at 26 °C, which indicates that CR binding to insulin at pH 11.1 has indeed decreased. The equilibrium constant calculated from the data was reduced to 569.3 M^{-1}, a 2 order of magnitude decrease compared to the equilibrium constant at pH 7.4. The second equilibrium constant was found to be $2*10^4$ M^{-1}, but its binding stoichiometry was reduced to 0.015, an almost negligible contribution. The enthalpy contribution was slightly larger at pH 11.1 than at pH 7.4 at all temperatures; however, there was also a large decrease in the entropy at pH 11.1. Table 4.2 contains a summary of the thermodynamic parameters obtained from the ITC data. The binding of CR to insulin does decrease when the pH is increased and is significantly reduced at pH 11.1. The CR binding could be reduced further by increasing

124

the pH, since as it is, only a fraction (~1.26) of the lysines are deprotonated; which is probably why a more significant reduction in binding is not observed. Furthermore, the pHs used in these experiments were above CR's pKa (~6-7) and thus the sulfate groups should be negatively charged in all the experiments.
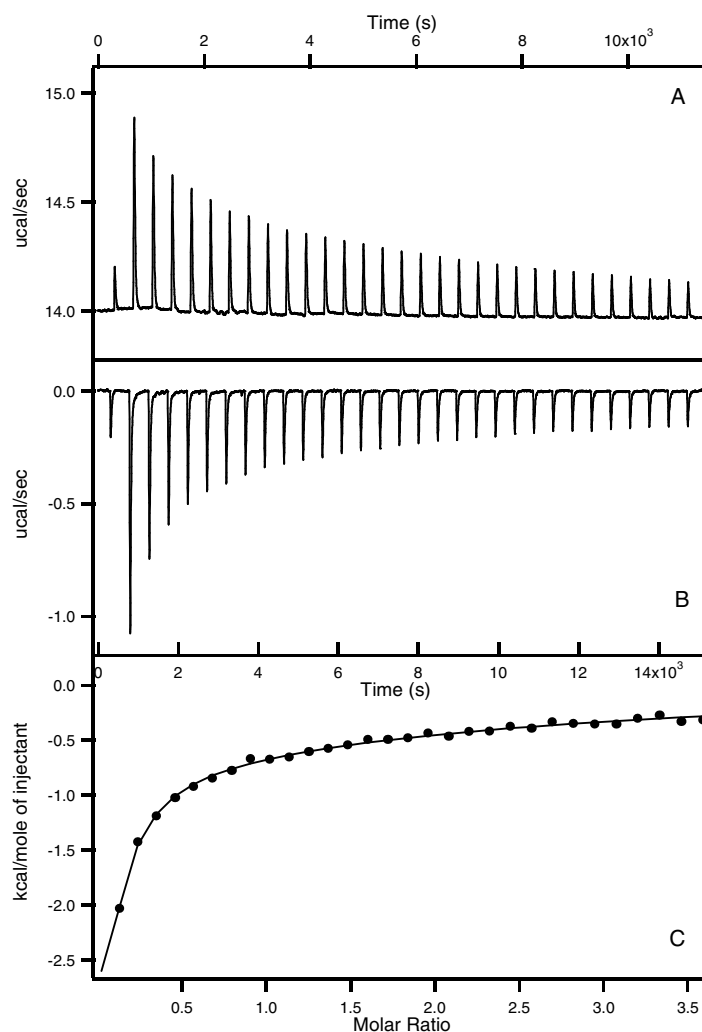
Figure 4.4   CR binding to fibrils in a pH 11.1 buffer solution at 8 °C, A) is the raw titration of a 3.8 mM CR solution into pH 11.1 buffer solution, B) is the raw titration data of the CR solution into a 0.25 mM insulin solution, and C) is the integrated data that was fit.

Temperature (°C)	8	26	46
N_1	0.45	0.47	1.26
K_1 (M^{-1})	$6.51*10^2$	$5.69*10^2$	$1.39*10^2$
ΔH_1 (kcal/mol)	-12.4	-6.34	-5.78
$T\Delta S_1$ (kcal/mol)	-8.73	-2.57	-2.65
N_2	0.035	0.015	0.18
K_2 (M^{-1})	$2.00*10^4$	$2.06*10^4$	$2.64*10^4$
ΔH_2 (kcal/mol)	-14.4	-13.5	-1.35
$T\Delta S_2$ (kcal/mol)	-6.86	-7.62	5.10

Table 4.2   The thermodynamic parameters for CR binding to an insulin solution in a
              pH 11.1 buffer solution at different temperatures.

Thioflavin T Binding to Fibrils

Titrations of ThT binding to fibrils were preformed in a pH 6.6 buffer solution at

three different temperatures (26 °C, 46 °C, and 60 °C). Titrations were only performed

using an amyloid fibril solution, because a titration of ThT into an insulin monomer

solution was performed and revealed no binding. Only endothermic peaks were

observed, which was consistent with the endothermic peaks observed when ThT is

titrated into buffer. Figure 4.5B is an example of the ITC raw data from a ThT (5.04

mM) into fibrils (0.6 mM) titration at 26 °C. The fibril concentration is calculated from

the amount of insulin monomer in the stock solution.   The titration isotherm is

completely different from the CR binding isotherm.   Instead of exothermic peaks

decreasing until the binding sites have saturated, the titration starts off exothermic then

goes endothermic then back to exothermic followed by endothermic peaks at the end of

the titration. The first peak of the binding isotherm was significantly larger than the rest

of the peaks, which implies that the majority of the binding occurs within the first

injection. The background titration of ThT into pH 6.6 buffer yields endothermic peaks

126

(~1.4 μcal/s to 1 μcal/s) that gradually decrease with subsequent injections (Figure 4.5A); however, there is not the dramatic decrease after the first peak as there is in CR. Since the background titration is subtracted from the raw binding isotherm, the endothermic peaks in the binding isotherm become exothermic peaks. The integrated peaks, from the subtraction of the raw binding and background, were calculated and the best fit determined for the data was a four sequential binding model (Figure 4.5C). The four equilibrium constants calculated were on the order of 10^{3}-10^{5} M^{-1} respectively, which suggests that the binding of ThT at pH 6.6 is very favorable at 26 °C. The first enthalpy term calculated was -0.37 kcal/mol, with an entropy value (TΔS) of 6.48 kcal/mol, and because of the large entropy contribution the binding would be more entropy driven likely from hydrophobic forces with a small electrostatic contribution. This is opposite to what was observed in the CR binding. The second and fourth enthalpy terms have a positive value with a larger positive entropy contribution (the titration done at 26 °C had negative values for the second enthalpy and entropy); however, these values tend to be less reliable than the first set of thermodynamic parameters due to the increase in error associated with multiple parameter fitting as well as background subtraction. Because of this, the analysis will focus on the first set of thermodynamic parameters. Table 4.3 is a summary of the thermodynamic parameters from ThT binding to the fibrils in a pH 6.6 buffer solution at three different temperatures.
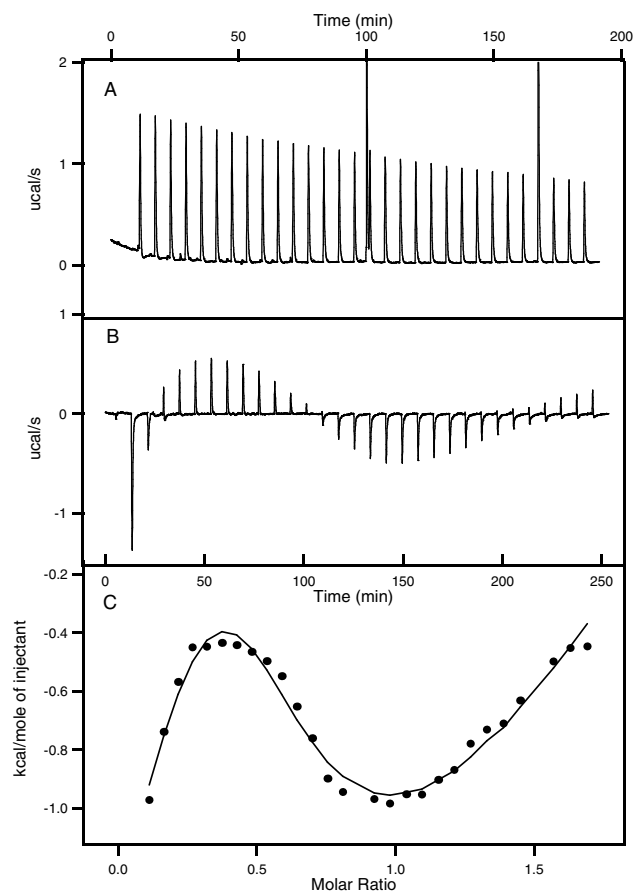
Figure 4.5   ThT binding to amyloid fibrils in pH 6.6 buffer solution at 26 ºC, A) is the raw background titration of a 5.04 mM ThT solution into a pH 6.6 buffer solution, B) is the raw background titration of the ThT solution into a 0.6 mM fibril solution, C) is the integrated data and the fit.

Temperature (°C)	26	46	60
K_1 (M^{-1})	$1.03*10^5$	$1.30*10^5$	$1.06*10^5$
ΔH_1 (kcal/mol)	-0.37	-2.59	-2.81
$T\Delta S_1$ (kcal/mol)	6.48	4.87	4.85
K_2 (M^{-1})	$2.49*10^3$	$1.87*10^5$	$3.34*10^5$
ΔH_2 (kcal/mol)	-28.2	5.77	3.48
$T\Delta S_2$ (kcal/mol)	-23.6	13.5	11.9
K_3 (M^{-1})	$4.58*10^3$	$6.81*10^4$	$4.93*10^4$
ΔH_3 (kcal/mol)	13.5	-21.7	-9.64
$T\Delta S_3$ (kcal/mol)	18.5	-14.6	-2.49
K_4 (M^{-1})	$3.27*10^6$	$7.44*10^4$	$6.39*10^4$
ΔH_4 (kcal/mol)	14.3	25.8	10.9
$T\Delta S_4$ (kcal/mol)	23.2	32.9	18.2

Table 4.3   Thermodynamic parameters for ThT binding to fibrils in a pH 6.6 buffer solution.

Since the ThT binding has a small enthalpy component, the concentration of fibrils was increased to 0.6 mM (compared to the insulin concentrations needed for the CR titrations), so that enough heat could be evolved to adequately detect binding. Typically, a minimum of 1 μcal/s evolved is required for the best detection; however, in the case of ThT binding to fibrils, the fibril concentration would have to be increased even further to obtain peaks of that magnitude. Increasing the fibril concentration further would have led to other problems, such as the fibril solution becoming more viscous with increasing concentration, which would cause problems with air bubbles accumulation and stirring in the sample cell. Even with the increase in fibril concentration, the amount of heat evolved was dramatically less than the amount of heat evolved with the CR binding. If the binding was exclusively hydrophobic interactions, very little heat would be evolved and it would be difficult to detect the binding with ITC at all. The small heat evolved in the ThT binding to fibrils at pH 6.6, indicates that binding is not strongly enthalpic in

nature and the binding is likely not through electrostatic forces alone, but also has a large contribution from hydrophobic interactions.

The next titrations were ThT binding to fibrils in a pH 3 buffer solution at 30 °C, 45 °C, and 60 °C. These titrations were performed at a pH lower than the pK_a of glutamic acid (pK_a 4.3-4.5) on the insulin backbone, in order to determine if the ThT binding had important electrostatic interactions needed for binding. If the ThT binding had significant electrostatic contribution then a reduction in binding should occur when the glutamic acid is protonated; conversely, if binding is through hydrophobic forces the protonation of glutamic acid should have little or no effect on binding. A titration was preformed using a 5.18 mM ThT solution and a 0.65 mM fibril solution in a pH 3 buffer. The raw binding data showed that the peaks started exothermic and then became endothermic (Figure 4.6B). When the background data was subtracted from the raw binding data all the endothermic peaks became exothermic. The best fit was found to be a three sequential binding site model. Table 4.4 is a summary of the thermodynamic binding data at pH 3. The ITC titrations revealed that there was a reduction in binding, and the first equilibrium constants were greatly reduced by more than an order of magnitude. In the first enthalpy term there was an increase in the enthalpy contribution and a decrease in the entropy. At pH 3 the binding is greatly reduced. A potential reason for the reduction in binding of ThT at pH 3 was thought to be from the protonation of the dimethlyamine group on the ThT dye; however, Klunk *et al.* determined the pK_a to be ~2 for a uncharged ThT derivative, 2-(4'-aminophenyl)-6-methylbenzothiazole.[39] Due to the similarities in the structure of the dyes it is assumed that the dimethylamine group on the ThT would have approximately the same pK_a. Therefore at pH 3, the reduction in binding is not due to the protonation of ThT, but from the protonation of the amino acids in the insulin monomer.
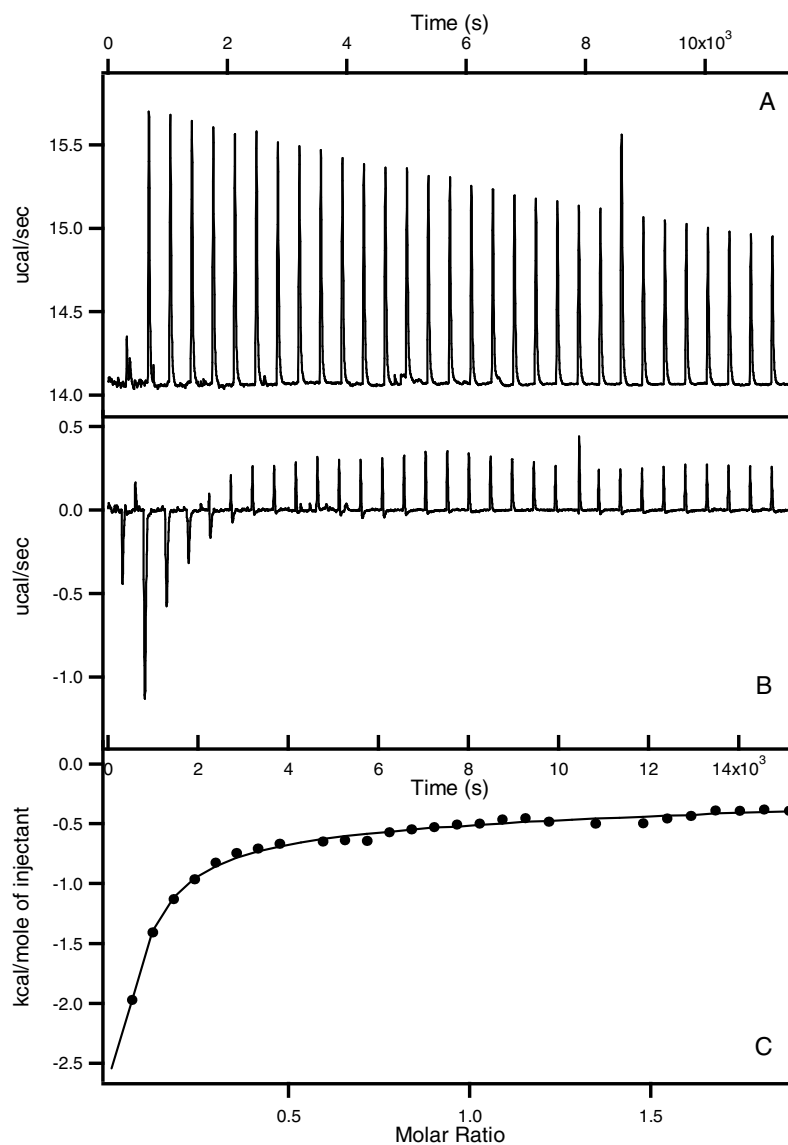
Figure 4.6   ThT binding to amyloid fibrils in pH 3 buffer solution at 30 °C, A) is the
raw background titration of a 5.18 mM ThT solution into a pH 3 buffer
solution, B) is the raw background titration of the ThT solution into a 0.65
mM fibril solution, C) is the integrated data and the fit.

Temperature (°C)	30	45	60
K_1 (M^{-1})	$6.65*10^2$	$2.43*10^3$	$1.54*10^3$
ΔH_1 (kcal/mol)	-8.79	-4.64	-7.52
$T\Delta S_1$ (kcal/mol)	-4.87	0.28	-2.66
K_2 (M^{-1})	$1.04*10^4$	$9.59*10^3$	$2.62*10^4$
ΔH_2 (kcal/mol)	9.65	5.23	6.96
$T\Delta S_2$ (kcal/mol)	15.22	11.02	13.69
K_3 (M^{-1})	$2.00*10^4$	$4.19*10^3$	$1.38*10^3$
ΔH_3 (kcal/mol)	-2.89	-3.20	-3.00
$T\Delta S_3$ (kcal/mol)	3.06	2.07	1.78

Table 4.4   Thermodynamic parameters for ThT binding to fibrils in a pH 3 buffer
         solution.

Ultracentrifugation of ITC ThT/fibril solutions

After each titration of ThT into fibrils the solution in the sample cell was removed
and saved for ultracentrifugation. The ITC solutions from the CR binding were not saved
for ultracentrifugation, since CR did not selectively bind to the fibrils, the bound could
not be isolated from the amount of free CR in solution. The ITC samples were
centrifuged in order to determine how much ThT was bound to the fibrils and as another
way to quantify the binding stoichiometry. Absorption spectra were taken of all the
supernatant layers and the original ITC solutions to determine the concentration. The
concentration calculated from the ThT absorption at 412 nm was then subtracted from the
total ThT concentration present in the centrifuge tube to give the concentration of ThT
bound to the fibrils. Table 4.5 shows the calculated percentages of ThT dye bound to
fibrils and the binding stoichiometry at both pH 6.6 and pH 3. At pH 6.6, the binding
stoichiometry was found to be ~1 ThT dye molecule bound to 2 insulin monomers, while
at pH 3 there was a large decrease in the number of ThT molecules binding to amyloid

fibrils and the stoichiometry was determined to be ~1 ThT dye molecules bound to every 20 insulin monomers. These results confirm the large decrease in ThT binding at pH 3 observed in the ITC experiments. The ITC fibril solutions were also ultracentrifuged to determine the percentage of insulin fibrillized, which would have to be taken into account when inputting the fibril concentration into the MicroCal fitting software. However it was determined that ~99% of the insulin present was fibrillized so no adjustments were made to the fibril concentrations. The increase in fibrillized insulin present in the ITC solution was a result of using the optimized method for making fibrils discussed in the experimental.

ITC Sample	pH 6.6 # of binding sites (ThT/insulin)	pH 3 # of binding sites (ThT/insulin)
F+ThT at 30°C	0.55	0.049
F+ThT at 45°C	0.54	0.049
F+ThT at 60°C	0.66	0.050

ITC Fibril solution	% Fibrillized
At pH 6.6	99.34
At pH 3	99.67

Table 4.5   Ultracentrifuge data for ThT binding to fibrils at pH 6.6 and at pH 3. Also the percent of fibrillized insulin in the ITC solutions.

Fluorescence

Fluorescence spectroscopy was used to observe how the change in pH affected the fluorescence intensity of the bound ThT dye. Figure 4.7 shows a plot of fluorescence intensity at 490 nm versus pH of the solution. The plot shows that the highest fluorescence intensity to be around pH 6.7 and as the pH decreases the fluorescence also

decreases slowly until finally dropping off sharply at pH 3.5, likewise as the pH increase past 6.7 the fluorescence intensity decreases steadily. The decrease in fluorescence at pH 3.5 corresponds with the decrease in binding observed at pH 3 in the ITC titrations. This furthermore confirms the ITC data by showing the decrease in ThT binding at lower pHs.
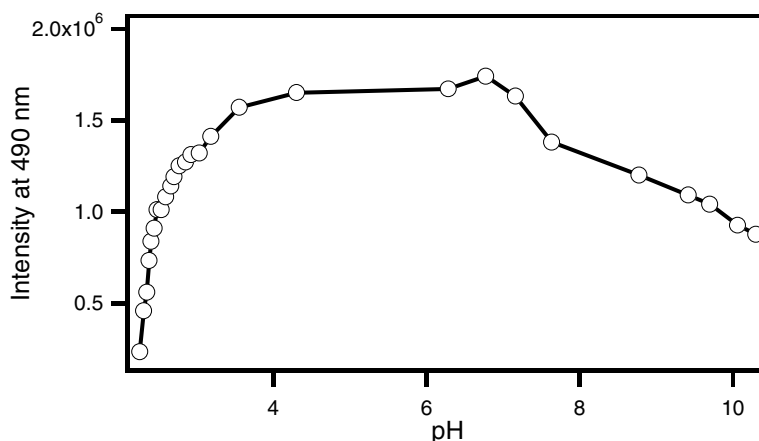
Figure 4.7   A plot of bound ThT fluorescence intensity at 490 nm versus pH.

CONCLUSION

This research has demonstrated that by changing the pH of the solution, the binding of CR and ThT to amyloid fibrils or insulin can be reduced. At pH 7.4, it was determined that CR binds to insulin or fibrils by a two binding site model and CR's binding mechanism is the same for both, insulin and fibrils. The thermodynamic parameters calculated from the binding data confirmed that electrostatic interactions are indeed the dominant forces that cause CR to bind to insulin. This also corroborates what other researchers have observed when they bound CR to other proteins.[22, 30] Then when the pH was adjusted to pH 11.1, a drastic change was observed when CR was bound to insulin; there was a two order of magnitude decrease in the equilibrium constant. This reduction in binding occurs when the amino acid lysine is deprotonated and is no longer

positively charged, which reduces the interactions between the amine group on the lysine and the sulfate groups on the CR.

The second part of this research shed some light into the binding mechanism of ThT to amyloid fibrils. When ThT was titrated into a fibril solution at pH 6.6, and a very unique binding isotherm was obtained with a fit to a four sequential binding site model. Analysis of the small enthalpy signal from binding was complicated by a larger background signal from the dilution of the ThT dye. From the first set of thermodynamic parameters it was determined that the ThT binding to amyloid fibrils was entropically driven with a small enthalpy contribution. Thus hydrophobic interactions are the driving force for ThT binding. The fluorescence intensity versus pH plot also gives an additional insight into the binding behavior of ThT and verifies that pH 6.7 is the ideal binding pH for ThT.

Then when the pH of the solution was decreased to pH 3, the binding of ThT decreased. The titrations at this pH yielded little heat, even with a slight increase in the ThT concentration (relative to the ThT concentration at pH 6.6), with the same concentration of fibrils. Since little heat was evolved but binding still occurred the conclusion is that by protonating glutamic acid, ThT can still bind relatively well and through hydrophobic interactions. Finally, the ultracentrifugation data enabled another way to determine the binding stoichiometry of ThT binding at the two different pHs. The binding stoichiometry at pH 6.6 was more than ten times larger than at pH 3 which supports the ITC conclusions. Overall, we were able to gain further insight into how CR and ThT bind to amyloid fibrils.

REFERENCES

1.   Kelly, J. W., Alternative conformations of amyloidogenic proteins govern their behavior. *Current Opinion in Structural Biology* **1996,** 6, 11-17.

135

2.   Allsop, D.; Swanson, L.; Moore, S.; Davies, Y.; York, A.; El-Agnaf, O. M. A.; Soutar, I., Fluorescence anisotropy: A method for early detection of Alzheimer B-peptide (AB) aggregation. *Biochemical and Biophysical Research Communications* **2001,** 285, 58-63.

3.   Dobson, C. M., Protein folding and misfolding. *Nature (London)* **2003,** 426, (6968), 884-890.

4.   Sipe, J. D., Amyloidosis. *Annual Review of Biochemistry* **1992,** 61, 947-975.

5.   Murphy, R. M., Peptide Aggregation in Neurodegenerative disease. *Annual Review of Biochemistry* **2002,** 4, 155-174.

6.   Harper, J. D.; Lansbury, P. T. J., Models of amyloid seeding in Alzheimer's disease and Scrapie: Mechanistic truths and physiological consequences of the time-dependent solubility of amyloid proteins. *Annual Review of Biochemistry* **1997,** 66, 385-407.

7.   Sunde, M.; Serpell, L. C.; Bartlam, M.; Fraser, P. E.; Pepys, M. B.; Blake, C. C. F., Common core structure of amyloid fibrils by synchrotron X-ray diffraction. *Journal of Molecular Biology* **1997,** 273, 729-739.

8.   Ha, C.; Park, C. B., Template-Directed Self-Assembly and Growth of Insulin Amyloid Fibrils. *Biotechnology and Bioengineering* **2005,** 90, (7), 848-855.

9.   Kad, N. M.; Myers, S. L.; Smith, D. P.; Smith, D. A.; Radford, S. E.; Thomson, N. H., Hierarchical assembly of B_2-microglobulin amyloid *in vitro* revealed by atomic force microscopy. *Journal of Molecular Biology* **2003,** 330, 785-797.

10.   Murali, J.; Jayakumar, R., Spectroscopic studies on native and protofibrillar insulin. *Journal of Structural Biology* **2005,** 150, 180-189.

11.   Krebs, M. R. H.; Bromley, E. H. C.; Donald, A. M., The binding of thioflavin-T to amyloid fibrils: localisation. *Journal of Structural Biology* **2005,** 149, 30-37.

12.   Khurana, R.; Ionescu-Zanetti, C.; Pope, M.; Li, J.; Nielson, L.; Ramirez-Alvarado, M.; Regan, L.; Fink, A. L.; Carter, S. A., A general model of amyloid fibril assembly based on morphological studies using atomic force microscopy. *Biophysical Journal* **2003,** 85, 1135-1144.

13.   Khurana, R. C., Chris; Ionescu-Zanetti, C.; Carter, S. A.; Krishna, V.; Grover, R. K.; Roy, R.; Singh, S., Mechanism of thioflavin T binding to amyloid fibrils. *Journal of Structural Biology* **2005,** 151, (3), 229-238.

14.   Bouchard, M.; Zurdo, J.; Nettleton, E. J.; Dobson, C. M.; Robinson, C. V., Formation of insulin amyloid fibrils followed by FTIR simultaneously with CD and electron microscopy. *Protein Science* **2000,** 9, 1960-1967.

15.   Lindgren, M.; Sorgjerd, K.; Hammarstrom, P., Detection and Characterization of Aggregates, Prefibrillar Amyloidgenic Oligomers, and Protofibrils Using Fluorescence Spectroscopy. *Biophysical Journal* **2005,** 88, 4200-4212.

16.   Jimenez, J. L.; Nettleton, E. J.; Bouchard, M.; Robinson, C. V.; Dobson, C. M.; Saibil, H. R., The protofilament structure of insulin amyloid fibrils. *Proceedings of the National Academy of Sciences of the United States of America* **2002,** 99, (14), 9196-9201.

17.   Ban, T.; Yamaguchi, K.; Goto, Y., Direct Observation of amyloid fibril growth, propagation, and adaptation. *Accounts of Chemical Research* **2006,** 39, (9), 663-670.

18.   Levine, H. R., Quantification of beta-sheet amyloid fibril structures with Thioflavin T. *Methods in Enzymology* **1999,** 309, 274-284.

19.   Voropai, E. S.; Samtsov, M. P.; Kaplevskii, K. N.; Maskevich, A. A.; Stepuro, V. I.; Povarova, O. I.; Kuznetsova, I. M.; Turoverov, K. K.; Fink, A. L.; Uverskii, V. N., Spectral properties of Thioflavin T and its complexes with amyloid fibrils. *Journal of Applied Spectroscopy* **2003,** 70, (6), 868-874.

20.   Klunk, W. E.; Jacob, R. F.; Mason, R. P., Quantifying Amyloid beta-Peptide (AB) Aggregation Using the Congo Red-AB (CR-AB) Spectrophotometric Assay. *Analytical Biochemistry* **1999,** 266, 66-76.

21.   Benditt, E. P.; Eriksen, N.; Berglund, C., Congo Red Dichroism with Dispersed Amyloid Fibrils an Extrinsic Cotton Effect. *Proceedings of the National Academy of Sciences of the United States of America* **1970,** 66, (4), 1044-1051.

22.   Klunk, W. E.; Debnath, M. L.; Pettegrew, J. W., Development of small molecule probes for the beta-amyloid protein of Alzheimer's Disease. *Neurobiology of Aging* **1994,** 15, (6), 691-698.

23.   Jin, L.-W.; Claborn, K. A.; Kurimoto, M.; Geday, M. A.; Maezawa, I.; Sohraby, F.; Estrada, M.; Kaminsky, W.; Kahr, B., Imaging linear birefringence and dichroism in cerebral amyloid pathologies. *Proceedings of the National Academy of Sciences of the United States of America* **2003,** 100, (26), 15294-15298.

24.   Turnell, W. G.; Finch, J. T., Binding of the dye Congo Red to the amyloid protein pig insulin reveals a novel homology amongst amyloid-forming peptide sequences. *Journal of Molecular Biology* **1992,** 227, 1205-1223.

25.   Nielson, L.; Frokjaer, S.; Brange, J.; Uversky, V. N.; Fink, A. L., Probing the mechanism of insulin fibril formation with insulin mutants. *Biochemistry* **2001,** 40, 8397-8409.

26.   Nielson, L.; Khurana, R.; Coats, A.; Frokjaer, S.; Brange, J.; Vyas, S.; Uversky, V. N.; Fink, A. L., Effect of environmental factors on the kinetics of insulin fibril formation: Elucidation of the molecular mechanism. *Biochemistry* **2001,** 40, 6036-6046.

27.   Shinchuk, L. M.; Sharma, D.; Blondelle, S. E.; Reixach, N.; Inouye, H.; Kirschner, D. A., Poly-(L-Alanine) Expansions form Cor Beta-Sheets that Nucleate Amyloid Assembly. *Proteins: Structure, Function, and Bioinformatics* **2005,** 61, 579-589.

28.   Klunk, W. E.; Jacob, R. F.; Mason, R. P., Quanitfying amyloid by Congo red spectral shift assay. *Methods in Enzymology* **1999,** 309, 285-305.

29.   Khurana, R.; Uversky, V. N.; Nielson, L.; Fink, A. L., Is Congo Red an Amyloid Specific Dye? *Journal of Biological Chemistry* **2001,** 276, (25), 22715-22721.

30.   Kim, Y.-S.; Randolph, T. W.; Manning, M. C.; Stevens, F. J.; Carpenter, J. F., Congo Red populates partially unfolded states of an amyloidogenic protein to enhance aggregation and amyloid fibril formation. *Journal of Biological Chemistry* **2003,** 278, (12), 10842-10850.

31.   Nesterov, E. E.; Skoch, J.; Hyman, B. T.; Klunk, W. E.; Bacskai, B. J.; Swager, T. M., In Vivo optical imaging of amyloid aggregates in brian: Design of fluorescent markers. *Angewandte Chemie (International ed. in English)* **2005,** 44, 5452-5456.

32.   Frasca, V., Microcalorimetry: A powerful tool for characterizing amyloid fibril formation. *American Biotechnology Laboratory* **2006,** 24, (2), 8-10,12.

33.   Jelesarov, I.; Bosshard, H. R., Isothermal titration calorimetry and differential scanning calorimetry as complementary tools to investigate the energetics of biomolecular recognition. *Journal of Molecular Recognition* **1999,** 12, 3-18.

34.   Cliff, M. J.; Gutierrez, A.; Ladbury, J. E., A survey of the year 2003 literature on applications of isothermal titration calorimetry. *Journal of Molecular Recognition* **2004,** 17, (513-523).

35.   Kardos, J.; Yamamoto, K.; Hasegawa, K.; Naiki, H.; Goto, Y., Direct measurement of the thermodynamic parameters of amyloid formation by isothermal titration calorimetry. *Journal of Biological Chemistry* **2004,** 279, (53), 55308-55314.

36.   Zeronvnik, E.; Skerget, K.; Tusek-Znidaric, M.; Loeschner, C.; Brazier, M. W.; Brown, D. R., High Affinity copper binding by stefin B (cystatin B) and its role in the inhibition of amyloid formation. *FEBS Journal* **2006,** 273, (18), 4250-4263.

37.   Nolan, C.; Margoliash, E.; Peterson, J. D.; Steiner, D. F., The Structure of Bovine Proinsulin. *Journal of Biological Chemistry* **1971,** 246, (9), 2780-2795.

38.   Edwards, R. A.; Woody, R. W., Molecular orbital calculations of the optical properties of Congo red and Cibacron blue and their complexes with proteins. *Journal of Physical Chemistry* **1983,** 87, 1329-1337.

39.   Klunk, W. E.; Wang, Y.; Huang, G.-f.; Debnath, M. L.; Holt, D. P.; Mathis, C. A., Uncharged thioflavin-T derivatives bind to amyloid-beta protein with high affinity and readily enter the brain. *Life Sciences* **2001,** 69, 1471-1484.

Vita

Catherine Carter Kitts was born in Midlothian, VA on July 17, 1979 to Robert Dale and Theresa Kitts. She grew up in Midlothian, VA and attended Midlothian High School. She graduated high school in 1998 with honors. She then attended college at James Madison University in Harrisonburg, VA where she pursued a major in Chemistry and a minor in Mathematics. During her college career she actively pursued research in chemistry. In May of 2002, she received a Bachelors of Science degree in Chemistry from James Madison University. Upon completion of her undergraduate degree, she moved to Austin, TX to pursue a doctoral degree in physical chemistry from the University of Texas at Austin.

Permanent address: 13371 Drakewood Road, Midlothian, VA 23113

This dissertation was typed by Catherine C. Kitts.